2019

Mechanical Properties of Brittle Ceramics: Case Study of Boron Rich Ceramics and Acropora cervicornis Coral Skeleton

Alejandro Carrasco-Pena
University of Central Florida

STARS Citation

Carrasco-Pena, Alejandro, "Mechanical Properties of Brittle Ceramics: Case Study of Boron Rich Ceramics and Acropora cervicornis Coral Skeleton" (2019). *Electronic Theses and Dissertations, 2004-2019*. 6337.
https://stars.library.ucf.edu/etd/6337

MECHANICAL PROPERTIES OF BRITTLE CERAMICS: CASE STUDY OF BORON RICH

CERAMICS AND *ACROPORA CERVICORNIS* CORAL SKELETON

by

ALEJANDRO CARRASCO-PENA
B.S. Western Michigan University, 2012
M.S. Western Michigan University, 2014

A dissertation submitted in partial fulfillment of the requirements
for the degree of Doctor of Philosophy
in the Department of Mechanical and Aerospace Engineering
in the College of Engineering and Computer Science
at the University of Central Florida
Orlando, Florida

Spring Term
2019

Major Professor: Kawai Kwok

ABSTRACT

Ceramics are ubiquitous in man-made and natural structures. Their mechanical properties highly depend on their composition, microstructure and level of defects in the bulk of the material, the latter affecting the integrity of the components; such is the case of boron-rich ceramics where large agglomerates create high stressed regions, or coral skeleton where porosity determines their strength against hydrodynamic forces present in the ocean tides. Therefore, studying the properties of ceramic materials using invasive and non-invasive methods helps in the understanding of the link between the properties and the performance of the structures. The aim of this research was to test the novel ceramic component ZrB_2-30wt%SiB_6 and *Acropora cervicornis* coral skeleton using non-conventional techniques that allow for the study of their mechanical properties and their behavior when exposed to external loads present in their environments of application. The first part of this study focuses on understanding the effects of adding SiB_6 to enhance the mechanical properties of ZrB_2 ceramics for their ultra-high temperature use. The second part will emphasize in the behavior of *Acropora cervicornis* coral skeleton when exposed to compressive forces and the effects porosity has on this structure when subjected to such loads. It was found that the SiB_6 phase was not stable after sintering of the composite and large agglomerates were present in the surface of the material acting as stress concentrators, thus compromising the biaxial strength of the component that resulted to be 224.9 MPa. It was also found that coral skeletons are highly susceptible to porosity which creates variability on the elastic modulus ranging from 60-1 GPa for simulated porosity of 0-90% respectively and a strength of 3.56 ± 0.31 GPa obtained through Vickers indentation. Finite element models were developed and validated against experimental results for the ZrB_2-30wt%SiB_6 and *Acropora cervicornis* coral skeleton.

iii

This dissertation is dedicated to my family for their constant support and the wisdom they have provided me throughout my entire life and for leading me into accomplishing this important achievement.

ACKNOWLEDGEMENTS

TABLE OF CONTENTS

LIST OF FIGURES

LIST OF TABLES

1. INTRODUCTION

1.1. <u>Motivation</u>

The following research involves the study of three subjects that are of great importance for the advancement of knowledge in the field of structural ceramics, that are brittle in nature, and the ways of studying their mechanical properties, including their strength and elastic modulus for cases when they are solid and porous, using invasive and non-invasive techniques. The first part of the research consists on the study of boron-rich ceramics used as refractory materials for ultra-high temperature applications and the properties of a novel composition that consists of ZrB_2-30wt%SiB_6; the second part of the research consists on the study of the compressive behavior of the staghorn coral *Acropora cervicornis* skeleton and the influence porosity has in its elastic modulus and fracture strength; and the third part of the research consists on the development of an *in-Situ* Raman spectrometer for the study of the real-time response of Raman active material when these are exposed to external loads.

1.1.1. Boron-rich Ceramics

Ceramics with boride structure have been used as refractory materials, especially ZrB_2 and HfB_2, and have been extensively studied for their application in the aerospace industry for supersonic flight and atmosphere re-entry vehicles applications [1,2]. The outstanding mechanical properties of ZrB_2 and HfB_2 and their high thermal conductivity and melting points make them ideal materials for environments with high temperatures and corrosion [2]. Monolithic ZrB_2 and HfB_2 have a density of 6.12 g/cm^3 and 11.21 g/cm^3 respectively which makes ZrB_2 more feasible for aerospace applications due to the lower mass per volume it exhibits [3]. The Young's modulus and Poisson's ratio for monolothic ZrB_2 and HfB_2 are 489 GPa and 480 GPa, and 0.11 and 0.12, respectively [2]. For thermal conductivity and melting temperature for monolithic ZrB_2

1

and HfB$_2$, which are important properties for ultra-high temperature applications, it was found that the values were 60 W/mK and 104 W/mK, and 3245 °C and 3380 °C, respectively [2]. Even though these materials exhibit very good mechanical properties they have the disadvantage of being very brittle which compromises their use as structural materials. For this reason, additives have been added to create composite materials based on ZrB$_2$ and HfB$_2$ in order to keep the excellent mechanical properties at high temperatures these materials exhibit and, at the same time, improve the strength of the ceramics for their better use in structural applications [2]. One of the additives that is being widely studied is the SiC which is typically mixed with ZrB$_2$ in a range of 10vol%-30vol%, improving the flexural strength of the ceramic from 275-629 MPa for monolithic ZrB$_2$ to a maximum of approximately 1089 MPa for the ceramic composite of ZrB$_2$-SiC [2]. The flexural strength of the ceramics does not only depend on the additives used to improve the mechanical properties of the composite, but also on the sintering method used [4].

1.1.2. *Acropora cervicornis* skeleton and the aragonite CaCO$_3$ structure

Other ceramic materials have been found to be of great importance due to their impact in nature and their contribution as structural base for living beings. One of these ceramics is found in the non-living part of coral reefs whose structure is mainly composed by an aragonite structure of CaCO$_3$ [5]. Coral reefs are living organisms that can be found throughout the world. They are the most diverse ecosystem in the marine environment and constitute the largest biological structure on Earth [6]. Understanding the mechanical properties of the non-living component in them and the interaction with the environment that surrounds it is of great importance for advancements in the protection of coastlines and their ecosystem since coral reefs serve as physical barriers to waves generated by storms or tsunamis [7,8]. Another benefit from coral reefs is that they provide habitat for a great number of living organisms, such as the polyps who

populate the coral structures and bring them to life [9]. In the last few decades, coral reefs have been found to possess an ambiguous future due to anthropogenic forces that range from climate and water temperature change, and human activity [10,11,12]. Overfishing is another activity that has been harming the health and growth of coral reefs. Algae has been found to compete against coral reefs for space and survival on the oceans, and overfishing of the parrotfish is allowing for the uncontrolled growth of algae affecting the spread of coral reefs on the coasts and their existence [13,14]. *Acropora cervicornis* (Lamarck, 1816) was a coral reef that once populated the waters of the Caribbean sea and the Atlantic ocean reproducing by fragmentation of its branches and forming extensive thickets in shallow water of less than 30 m deep, providing habitat to many species that populate these waters [15], but lately it has been affected and its existence threatened by all these environmental changes and activities, reducing only to small isolated patches in the Dominican Republic, Florida, Puerto Rico, Jamaica and Honduras [16]. Figure 1 shows an example of the staghorn coral *Acropora cervicornis* in its natural environment providing a habitat for a small school of fish.
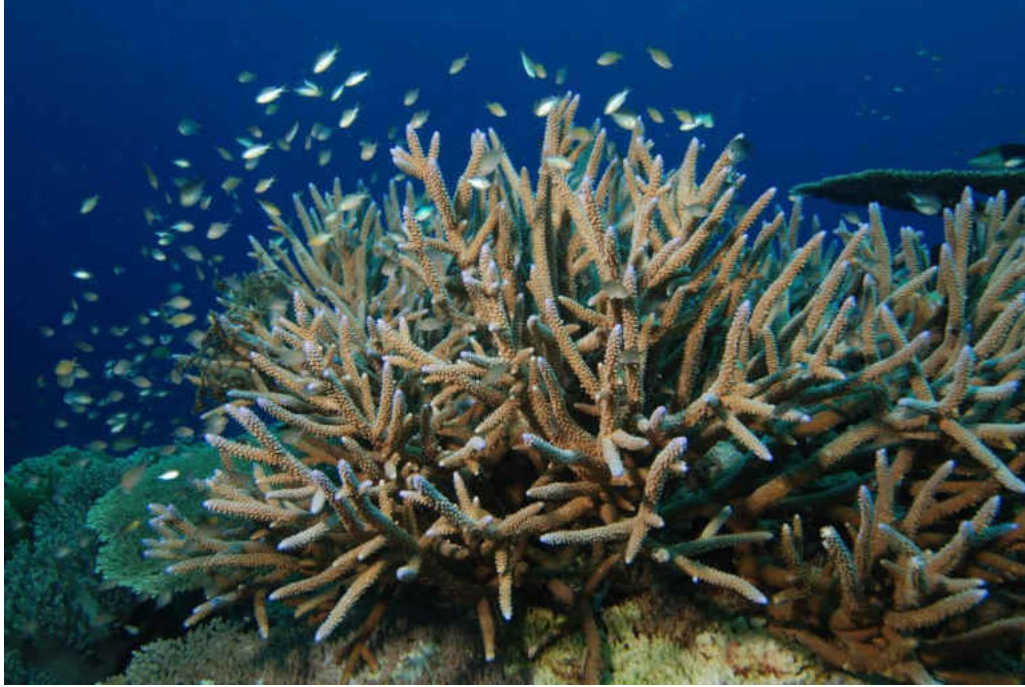
Figure 1: Staghorn coral *Acropora cervicornis* in its natural habitat [17].

1.1.3. *In-Situ* Raman Spectrometer

Raman spectroscopy is a well-known optical non-invasive technique that can be used for the quick characterization of materials and the phases present in them. Raman spectroscopy analyzes the energy frequencies in molecules, mainly the vibrational, rotational and low-frequency modes [18]. The collection of this type of spectrum is done through the utilization of a laser that excites a Raman-active molecule which emits a radiation, of an inelastic nature, that passes through a monochromator and an elastic, or Rayleigh, radiation filter and is interpreted by a charge coupled device (CCD) detector allowing for the identification of the wavelength location, or Raman bands, and the intensity of the radiation from the molecules that conform the material. The locations of these Raman bands serve as a fingerprint for the characterization of Raman active materials and their shift or deformation serve as a tool for the study and quantification of any stress being applied to the sample. However, when a load is applied to a structural ceramic it is done on external equipment that does not allow for the collection of

Raman spectra to understand the instantaneous vibrational response of the material. Therefore, the development of an instrument that permits the collection of the real-time behavior of materials withstanding a mechanical load using the Raman spectroscopic technique is of great importance in order to understand the instantaneous changes in phases a material experiences when exposed to such loads and the distribution of stressed over the surface of the sample.

2. GOALS OF THE RESEARCH

The goals of this research work are to investigate the biaxial strength and mechanical properties of brittle ceramic made from ZrB_2- and HfB_2-based ceramics, sintered using the spark plasma method, through the ring-on-ring technique and resonant ultrasound spectroscopy. The second part of the research work consists on the study of the uniaxial compression strength for right circular cylindrical specimens of *Acropora cervicornis* staghorn corals. The tests will be accompanied by Raman spectra mapping and the study of the strength of the skeleton in relation to its porosity that will serve as validation for the results and also as a tool to expand the field of investigation for the behavior of these materials under certain loads. The third part of the research will consist on the development of an *in-Situ* Raman spectrometer that will allow for the capturing of the real-time vibrational response of Raman active materials under mechanical loads. The samples studied were chosen due to their accessibility and their importance in the advancement of ultra-high temperature structural materials and the understanding of the mechanical properties of materials, such as $CaCO_3$ in biological applications for the preservation of the coral reefs.

3. LITERATURE REVIEW

Ceramics are exciting materials with ionic of covalent bonding between the atoms that determine their unique mechanical, electrical and structural properties, and can be implemented for a variety of different applications. While many ceramic materials are man-made their existence also occurs naturally. The characteristic features of ceramics, in comparison with other classes of materials, are the high hardness, high Young's modulus, high melting temperatures, and high specific strength, resulting from the type of atomic bonding present in the structure. The type of atomic bonding in a material also affects how it fractures, as is the case for ceramics that due to the type of bonding complete fracture occurs when all the bonds are pulled and broken apart by a stress high enough to overcome the theoretical strength of the material [19]. The stiffer and stronger bonds in a ceramic determine the material's theoretical strength and its Young's modulus, and thus, providing that the ideal ceramic is defect free, the theoretical strength can be approximated by the maximum stress (σ_{max}) to be between *E/5* to *E/20* [19]. However, due to the imperfections found in ceramics and the number of defects present in their structure the actual strength is much lower and it is located between *E/100* to *E/1000*, as in most cases the flaws present locally concentrate stresses that significantly waken the material [20]. The imperfections, in the form of flaws and defects, also concentrate stress and serve as the initial point where cracks start to propagate. These defects in ceramics are typically found in the form of small flaws characterized mainly for being large grains, pores, voids and cracks where fracture tend to originate [19], determining the strength of the ceramic sample which depends on the stress the largest defect can handle [20,21,22,23]. This characteristic does not allow for the strength to be described as a unique number, but as the result of a statistical distribution function that can determine the failure probability of a ceramic material undergoing a specific test. It is worth to

7

mention that in an ideal case where no defect is present on the sample tested, a failure probability of zero may exist [19]. The critical size for the failures that result after processing ceramics typically ranges between 100 μm and smaller lengths and are difficult to be detected by non-destructive experimental techniques, thus compromising mechanical properties of the ceramic material, such as strength, brittleness, among others, creating a challenge for designers considering using these types of materials for structural purposes since they can fail instantaneously [19]. Usually, a variation in the strength of ceramic materials in the interval of ±25-100% from the mean exists, exposing another difficulty in the selection of ceramic materials for structural purposes [20].
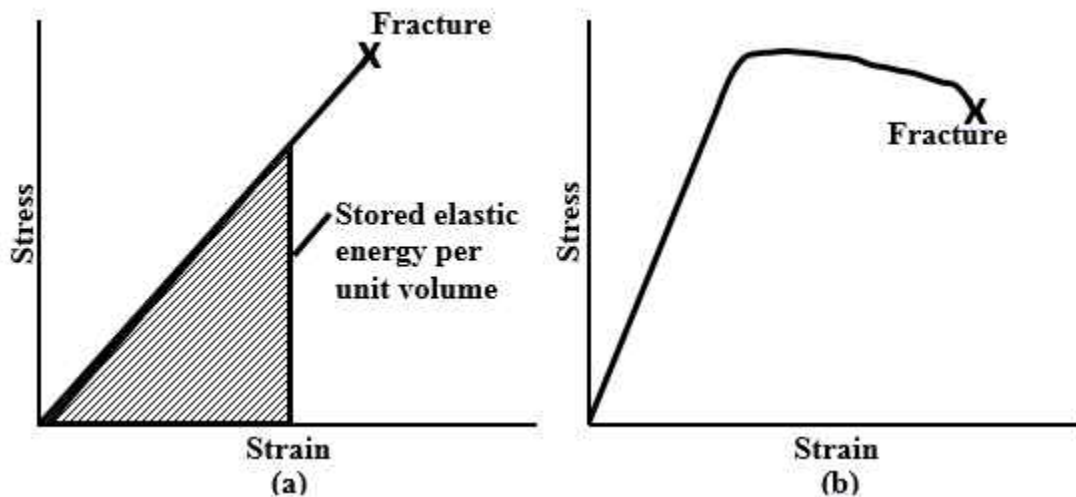
Figure 2: Typical stress-strain curve for (a) brittle materials and (b) ductile materials

It is well known that the application of stress to the material results in reversible elastic deformation followed by either fracture without reaching a yield point and plastic deformation, or fracture that is preceded by plastic deformation, behavior that is evidently different in ceramic materials since the strong atomic bonding that characterizes them makes them brittle and they fail without demonstrating any behavior of plastic deformation, therefore going from the elastic

8

region to complete failure [24]. Ceramics typically fail in a brittle manner, even when used for structural purposes. The strength of ceramic materials usually ranges between 10 to 50 GPa and it is proportional to the elastic modulus of it, however it is affected by the amount of defects present in the structure that causes failure below the theoretical level, therefore, decreasing the presence and size of defects improves the material resistance to failure by breakage. [19].
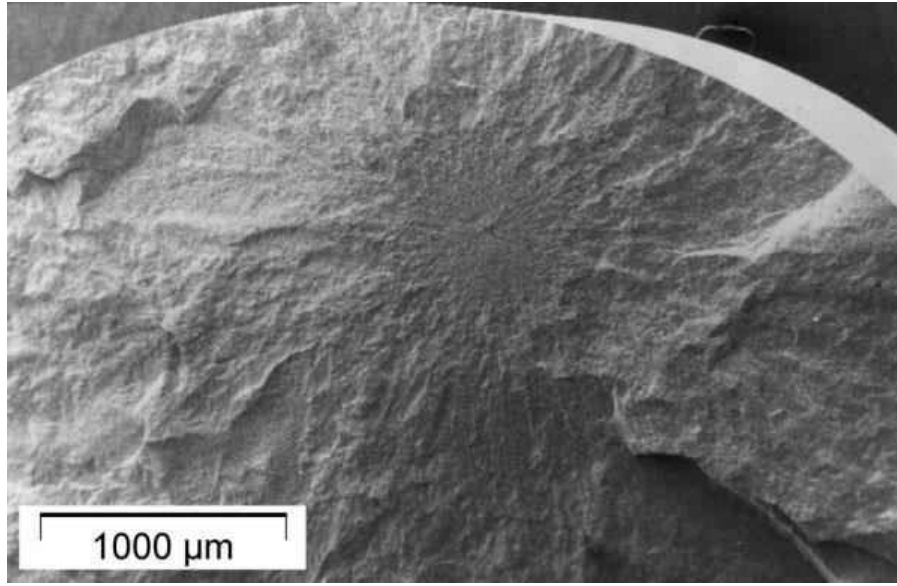
Figure 3: Brittle failure of a silicon nitride valve by a rupture test. The fracture surface shows that the crack path is perpendicular to the loading [19].

Fracture, in a brittle manner, is caused by the presence of flaws acting as stress concentrators in the body of the ceramic that result from processing or machining of the ceramic. The stress concentration generated by these flaws increases with the dimension of the defect, especially when their elongation is much longer than their width [19]. Mathematically, the stress concentration at the tip of the crack that behaves perpendicularly to the stress direction can be described as [19],

$$\frac{\sigma_n}{\sigma} = 1 + \frac{2c}{b}$$

(1)

where σ is the applied far field stress, σ_n is the stress at the tip of the crack length a, which is proportional to the major semiaxis c perpendicularly oriented to the stress direction, and b is the minor semiaxis proportional to the crack width. More precisely, this relationship can be described as [19],

$$\frac{\sigma_n}{\sigma} \approx 2\sqrt{\frac{c}{\rho}} \qquad (2)$$

where ρ is the radius of the curvature of the crack tip. For such cases, the stress present at the crack tip goes to infinity when ρ is atomically sharp and approaches to zero. From Equation (2) it can be estimated that for an applied stress with magnitude $\sigma = E/1000$, the ratio between the major and minor semiaxis, c and b respectively, has to be equal 50 and the ratio between the crack length and the crack tip radius, c and ρ respectively, has to be greater or equal to 2500 in order to create a stress concentration with magnitude $\sigma_n = E/10$ which is equal to the theoretical strength at the tip notch [19].

At the crack tip, the stress field can be determined with a linear relationship that scales with a stress intensity factor K represented by [25],

$$K = \sigma Y \sqrt{\pi a} \qquad (3)$$

where σ is the nominal stress in the cracked body, a is the crack length and Y is a dimensionless geometric correction factor approaching to one for cracks of small sizes relative to the component size typical for ceramics, such as $Y = 1.12$ for the straight through edge cracks [19]. When cracks are treated as elliptical holes with a tip radius of zero the stress component becomes infinite at the crack tip and goes over the theoretical strength of the ceramic component even at low loads and cracks with small dimensions (Eq. 2). Evidence has been found of cracks that do

not grow under an applied load indicating that certain conditions, described by Griffith, must be met for a crack to expand and propagate [26].

According to Griffith [26], only cracks with equal or larger sizes than the critical crack length, a_c, grow, but smaller cracks maintain their sizes and remain stable. Crack growth is prompted when the growth reduces the total energy of the body since strength, σ_f, is proportional to $1 \cdot (a_c)^{-1/2}$. According to Griffith and Irwin [19] for crack propagation to occur the fracture criterion $K \geq K_c$ is necessary, where K_c is the fracture toughness defined also as the critical stress intensity factor defined by $K_c = (E \cdot G_c)^{1/2}$, subsequently, G_c is the energy required to generate a new crack. Usually, the surface energy of a ceramic is approximately $1 \ J/m^2$ with fracture energy ranging between $10\text{-}3000 \ J/m^2$, which is a summation of the energy needed for the formation of two new surfaces (2γ) and any other process occurring during crack growth and propagation such as, the energy dissipation ahead of the crack tip on the crack bridges, among others [19].

The tensile strength, σ_f, of a ceramic component is mathematically expressed by the stress at the moment of fracture as follows [19],

$$\sigma_f = \frac{K_c}{Y\sqrt{\pi a_c}} \qquad (4)$$

This relationship indicates that tensile strength is directly proportional to fracture toughness, K_c, and inversely proportional to the square root of the critical crack size of a_c. The critical crack size a_c is then expressed as [19],

$$a_c = \frac{1}{\pi}\left(\frac{K_c}{Y\sigma_f}\right)^2 \qquad (5)$$

Typically, for many ceramic materials the K_c / σ_f ratio is in the order of 0.01 m$^{1/2}$, and for the case when fractures initiates within the ceramic's body, then the dimensionless correcting

factor $Y = 2/\pi$, yielding an a_c of about 80 μm, which indicates that the critical size of flaws has a strong dependence on the processing conditions of the ceramics [19]. The starting point of a fracture within a ceramic body is typically affected by common flaws, such as agglomerates from secondary phases, large pores and grains, inclusions, voids, and regions with accumulated small pores [27,28]. For the outer surface of the ceramic, the origin of a fracture is favored by defects created by contact damages to the body, such as scratches, indents and breakage due to contact [29].

The first successful mathematical approach for fractures and the idea that the free energy of a body undergoing stress should decrease as cracks grow and propagate was defined by Griffith and expressed as follows [21],

$$U = \left(\frac{-\pi a^2 \sigma}{E}\right) + 4c\gamma \qquad (6)$$

where U is the free energy of the ceramic, a is the crack size, σ is the stress on the surface, γ surface energy, and E the elastic modulus of the material. Fracture in a material was determined to not be the separation of two crystal planes but the growth of the cracks that exist and are proper of the ceramic body [21]. Griffith described the fracture stress of a material to depend on the materials elastic modulus, E, and surface free energy, γ, on the crack size, a, expressed as follows,

$$\sigma_f = \sqrt{\frac{2E\gamma}{\pi a}} \qquad (7)$$

This equation Eq. (7) is known as the Griffith equation [21,23].

3.1. Boron-Rich Ceramics and Strength Measurement

According to Munz and Fett [24], the strength of ceramics is determined by their resistance to tensile stresses since ceramic materials have a natural tendency to resist much higher compressive forces than tensile ones before failure. Therefore, simple uniaxial tensile tests are very useful as they exhibit homogeneous stress distribution and pure uniaxial stress state, thus is the easiest technique to determine tensile strength [30,31,32]. However, the tests are notoriously difficult to perform due to both misalignment that causes eccentricity of the load in the tested ceramic samples or breakage of the sample during clamping, increasing the difficulties and cost of performing such tests [33].

To avoid the problems that arise when performing tensile testing in ceramics, different bending tests were designed and developed for samples with rectangular and circular cross-sections [34,35,36]. Under a bending test, the sample can be loaded either in a three- or four-point bending manner, with four-point bending being a more preferred technique as the extended region of the sample with the constant bending moment exists between the inner rollers that supports the sample in two points. During four-point bending, a greater area of the sample is stressed when compared to three-point bending, therefore more defects and flaws are stressed compromising the strength of the ceramic sample and lowering its strength value [24].

When loaded in compression, ceramics are able to tolerate much higher stresses than when loaded in tension [22,37,38,39,40]. The compression strength of a ceramic material is defined as the compressive force applied to the sample over the cross sectional area that is being loaded by the force and, similar to the tensile test, the stress distribution over the sample under a compression test exhibits a homogeneous behavior [24]. Many difficulties also accompany compressive tests on ceramic materials, showing most commonly misalignment issues that bring

13

eccentricity problems, misfit of the elastic constants of the material tested and the compression platens used to transfer the load, and the occurrence of stress singularity along the outer contact contour of the ceramic tested due to the misplacement of the sample on the cross-sectional area of the compression platens. In addition, another common complexity of the compression tests is the use of lubricating layers, such as graphite or soft metals, between the sample tested and the compression platens surfaces to reduce the possibility of load introduction through a single point on the specimen surface, therefore complicating the determination of the true value for the compressive strength of ceramics [24].

Even though uniaxial compression and flexural tests provide reliable results and easiness of sample preparation, it is in seldom scenarios that ceramics are loaded in such a simple uniaxial way in real-life applications, making the results of these tests less accurate when determining the strength of ceramics in comparison to biaxial loading tests. Biaxial flexural strength tests depict a more accurate representation of the true behavior of the ceramics in common real-world applications by applying stress to the tested ceramic sample in a biaxial manner. Among the advantages of biaxial strength techniques the most significant are found to be the capacity to test a larger effective surface area that does not contain any edge finishing defects, easiness in the sample preparation for the tests, ability to test thin-sheet materials, and the equibiaxial distribution of stress on the sample that allows for a better detection of defects [41]. The biaxial flexural tests of brittle ceramic samples involve the use of a loading punch, which varies in geometry according to the test performed, over a ceramic a sample that is being supported by a fixed fixture that also varies depending on the type of test being performed. The main idea is to apply stress through several independent points on the surface of the ceramic, creating a state of biaxial stress distribution. Some of the most common biaxial testing techniques include the ring-

14

on-ring, piston-on-three-balls, and ball-on-ring [41,42,43]. These tests produce biaxial stress in the sample through the bending induced by the loading punch that only contacts the ceramic piece in one point or a ring on the upper surface which, at the same time, is supported by a fixture that touches the lower surface of the ceramic in several points, typically containing the shape of a ring of points or three points defining a triangle. These configurations produce compressive stress on the face touching the loading punch and tensile stress on the face in contact with the supporting fixture, being the major stress accumulation located in the tensile surface enclosed in the region defined by the loading punch [41,42,43]. The maximum force recorded until sample breakage occurs during the biaxial test is then used to calculate the biaxial flexural strength of the material analyzed by following different relationships defined for each biaxial flexural test.

Flexural strength testing techniques for ceramics involve a wide range of methods that provide an alternative way to measure the strength of ceramics without the difficulties found in tensile testing [33]. The flexural strength tests can be divided into two methods which depend on how the ceramic samples are loaded. They can be either uniaxially loaded or biaxially loaded. Both methods possess different advantages and disadvantages when compared to each other, being the most significant ones on how the samples are prepared, the defects on the geometry of the samples, optimum test geometry between the test piece aspect ratio and the material overhang, and limitation on the type of material geometry that can be analyzed [41]. Among the most common uniaxial loading testing methods found are the three-point and four-point bending, while for biaxial loading testing some of the most popular methods are the ball-on-three-balls, ring-on-ring, and ball-on-ring. The following is a description of the different flexural testing methods, providing insights on the description of the geometry of the testing fixture and its relation to sample geometry as well as how the strength is determined for each case.

15

3.1.1. Processing Methods for Boron-Rich Solids

Spark-plasma sintering is an advanced sintering technique used for the densification of ceramic materials. In spark-plasma sintering, indirect heating is applied to a die by an electrical field where the ceramic powder compacts through the applied heat and pressure created by a uniaxial load on the sample [4]. This technique favors the small grain growth during sintering due to the short time the whole process takes compared to other sintering methods such as hot pressing or hot isostatic pressing, allowing for finer and more homogeneous grains in the ceramic composite and, for ZrB_2-based ceramics, refined microstructures can be obtained by short sintering cycles that spark-plasma offers [4]. Figure 4 shows an example of ZrB_2-ceramic powders sintered using the spark-plasma sintering method at 1900°C 1900°C, with heating rate of 200°C/min with pressure of 50 MPa for two different dwelling times, one at 3 min and the other at 10 min.
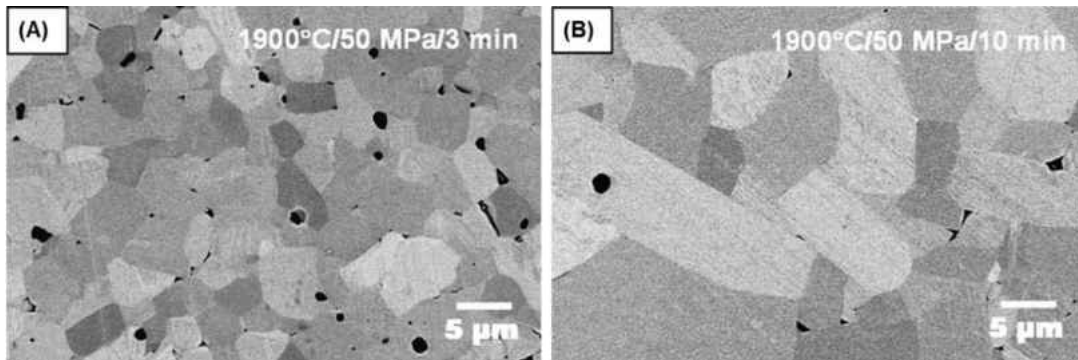
Figure 4: Spark-plasma sintering of ZrB_2 ceramics at 1900°C, with heating rate of 200°C/min with pressure of 50 MPa for a dwelling time of (A) 3 min and (B) 10 min [4].

When sintered by spark-plasma sintering, the behavior and grain growth of ZrB_2 is affected by the parameters of sintering temperature, holding time, and heating rate that are involved with this process [4]. The hardness and toughness of ZrB_2 and its composites were also found to improve when sintered by spark-plasma demonstrating that this technique is beneficial

for the processing of these ceramics [2]. A sintering plot for three different values of SiC in a

ZrB$_2$-SiC ceramic composites sample can be found in Figure 5.

1: ZrB$_2$-17vol%SiC   2: ZrB$_2$-32vol%SiC   3: ZrB$_2$-45vol%SiC
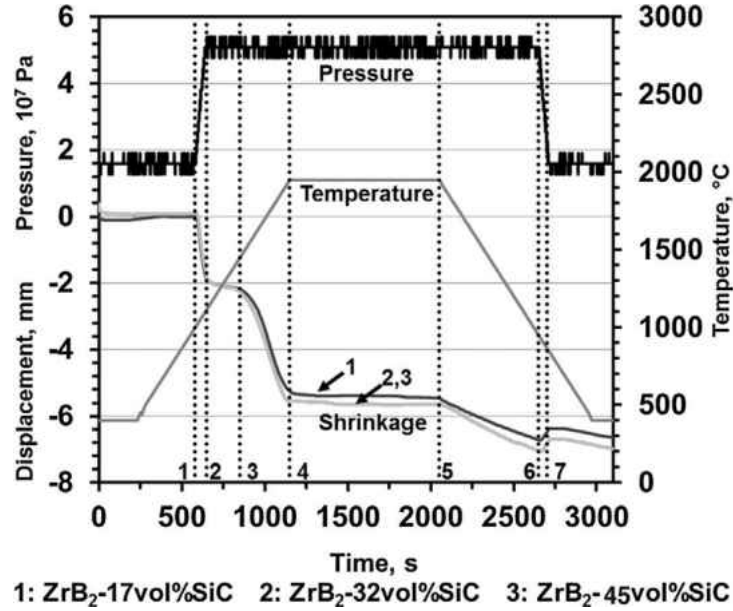
Figure 5: Sintering plot for three ceramic composites showing the pressure, temperature and shrinkage experienced during sintering [44].

3.1.2. Biaxial Strength Techniques

Biaxial strength methods for the determination of the strength of ceramics have been intensively used due to the advantages they provide among other strength testing techniques and the capability of depicting a realistic testing environment for brittle materials which, most of the times, are loaded biaxially in structural applications [42]. Mostly, samples with a disc-shaped geometry are tested with biaxial strength techniques even though some techniques, such as ring-on-ring, are capable of testing samples that are rectangular-shaped [45]. In simple uniaxial flexural tests, edge failures are undesirable features that are present and occur from the interaction of the sample and the testing fixture. These types of defects are eliminated by the use of biaxial flexural tests and, at the same time, these tests guarantee a more accurate measurement of the strength of the ceramic material [46]. Due to the increasing popularity of the biaxial

17

flexural methods, research has been conducted and many standards have been developed for different testing configurations of ceramic materials in order to validate their accuracy such as, ball-on-three-balls [47], the ball-on-ring [42,48], the piston-on-three-balls [42], and ring-on-ring [42,49]. Figure 6 shows a schematic of these tests and how the sample is placed on the testing fixture. It can be observed that a commonality exists among all tests in that the sample is always resting upon a surface that touches the supported surface of the ceramic on one point at a time, and the sample is loaded with a punch that makes contact with the upper surface in a similar manner. This configuration allows for tensile stresses to be generated on the bottom face of the ceramic that is in touch with the support, producing the greater stress accumulation within the region enclosed by the geometry of the loading punch used. The maximum stress has been modeled mathematically for the different test assemblies [42,47] and it is shown that maximum stress is dependent on the applied load, the Poisson ratio of the material, and the geometry of both, the testing fixture and the sample. Furthermore, biaxial flexural stress failure occurs on the region with the highest stress concentration and the stress distribution in the sample varies throughout the radius of the sample, being the highest at the center tensile surface and decreasing along the radial direction towards the edge of the ceramic.
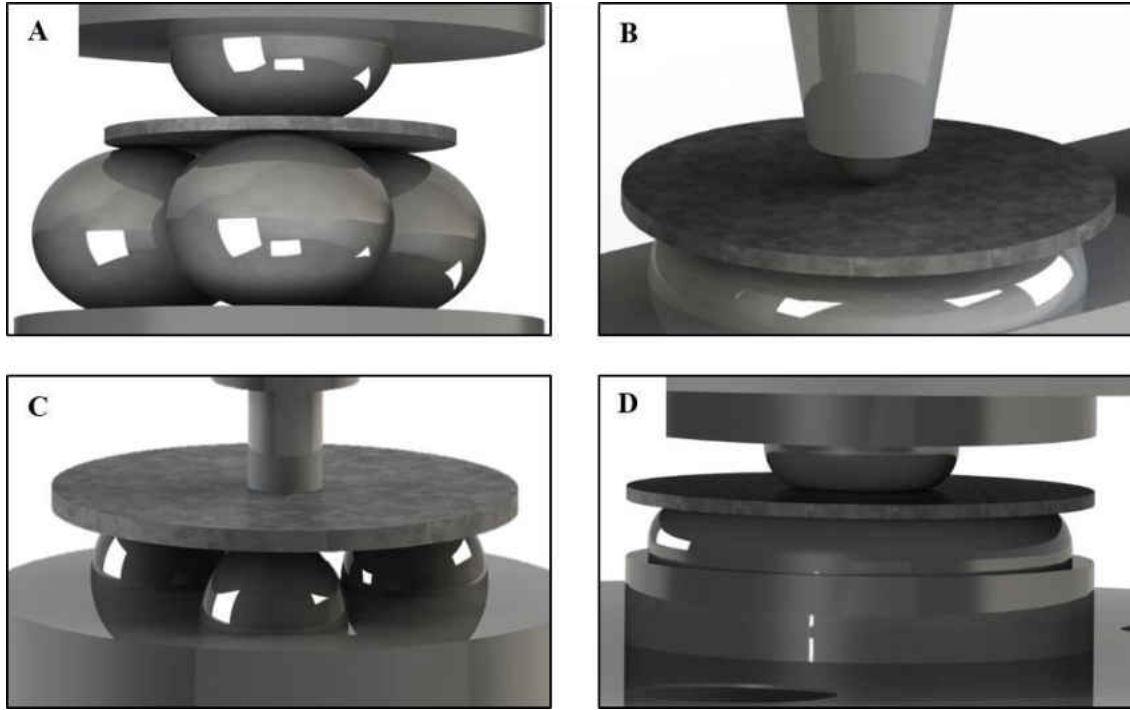
Figure 6: Schematic of biaxial strength tests using (A) ball-on-three-balls, (B) ball-on-ring, (C) piston-on-three-ball, and (D) ring-on-ring.

The ball-on-three-balls test is an innovative method to evaluate the biaxial strength of brittle ceramics. It consists on the test of sintered ceramic discs without any surface finish. The lower face of the specimen is in contact with the support region of the fixture, composed by three balls equidistantly located, and the upper face of the sample is loaded at its center with a fourth ball [47]. The ball-on-three-balls has a main advantage in that the samples do not require a specific surface finish, therefore making it useful for quality for control purposes in large scale production of ceramic components. In this test, the fracture load of the sample is measured and the maximum principal strength is considered to be a tensile stress concentrated in the center of the sample on the face opposite to the loaded surface [47]. The stress field in the disc-shaped ceramic sample is dependent to the load that is applied, sample geometry, the material's Poisson ratio, the radius of the loading region and the circumference defined by the supporting balls. The elastic properties of the fixture's balls and the elastic modulus of the ceramic material do not

19

contribute to the calculation of the maximum stress on the sample, which indicates that the stress field in the disc is independent from the non-linear changes in the loading process caused by the deformation of the loading and supporting balls in the fixture [47]. Figure 7 shows a schematic of the ball-on-three-balls set up and all the components that interact together in this test.
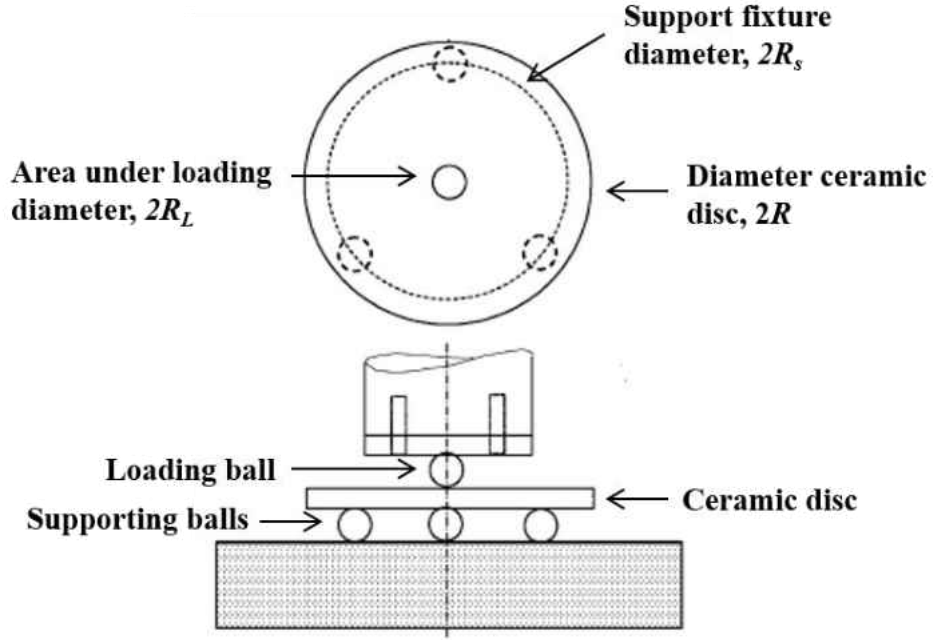
Figure 7: Ball-on-three-balls test setup and interacting components [50].

The maximum tensile stress is approximated by an equation developed by Shetty et al. [42] that explains the relationship of the material and the testing fixture as follows:

$$\sigma_{max} = \frac{3F(1+v)}{4\pi t^2} \cdot \left[1 + 2 \cdot ln\left(\frac{R_S}{R_L}\right) + \frac{1-v}{1+v} \cdot \left(1 - \frac{R_L^2}{2R_S^2}\right) \cdot \frac{R_S^2}{R^2}\right] \qquad (8)$$

where F is the applied load, v is the Poisson's ratio of the ceramic disc, t is the sample's thickness, R_s is the supporting fixture radius, R_L is the radius of the area under loading, and R is the sample's radius. The radial, σ_r, and tangential, σ_t, stress components defined in a polar coordinate system where also defined by Shetty et al [42] as:

$$\sigma_r(r) = \frac{3F(1+v)}{4\pi t} \cdot \left[2 \cdot ln\left(\frac{R_s}{r}\right) + \frac{1-v}{2(1+v)} \cdot \frac{R_s^2 - r^2}{R_S^2} \cdot \frac{R_L^2}{r^2} \cdot \frac{R_S^2}{R^2} \right] \qquad (9)$$

$$\sigma_t(r) = \frac{3F(1+v)}{4\pi t} \cdot \left[2 \cdot ln\left(\frac{R_s}{r}\right) + \frac{1-v}{2(1+v)} \cdot \left(4 - \frac{R_L^2}{r^2}\right) \cdot \frac{R_S^2}{R^2} \right] \qquad (10)$$

where r is the distance from the center of the face of the sample experiencing the tensile loading to the edge of the ceramic disc.

In the ball-on-three-ball biaxial strength test fracture initiates in the region of maximum stress located in the tensile surface under the loading ball in the center of the ceramic disc, where failure in a threefold symmetry predominates, although, depending on the stored elastic energy of the material, the number of fracture pieces resulting from the test may vary [47]. Figure 9 shows an example of fractured Al_2O_3 ceramic by the ball-on-three-balls biaxial flexural test and the area where failure was originated. The maximum stress that promotes fracture on the sample is directly proportional to the applied load delivered through the loading ball and inversely proportional to the square of the ceramic disc thickness [47], with a mathematical relationship expressed by [51],

$$\sigma_{max} = f(\alpha, \beta, v)\frac{F}{t^2} \qquad (11)$$

where F is the uniaxial load, f is the tensile stress dimensionless factor, α is the thickness to sample disc radius ratio, β is the support fixture radius to sample disc radius ratio, and v is the Poisson's ratio of the material.
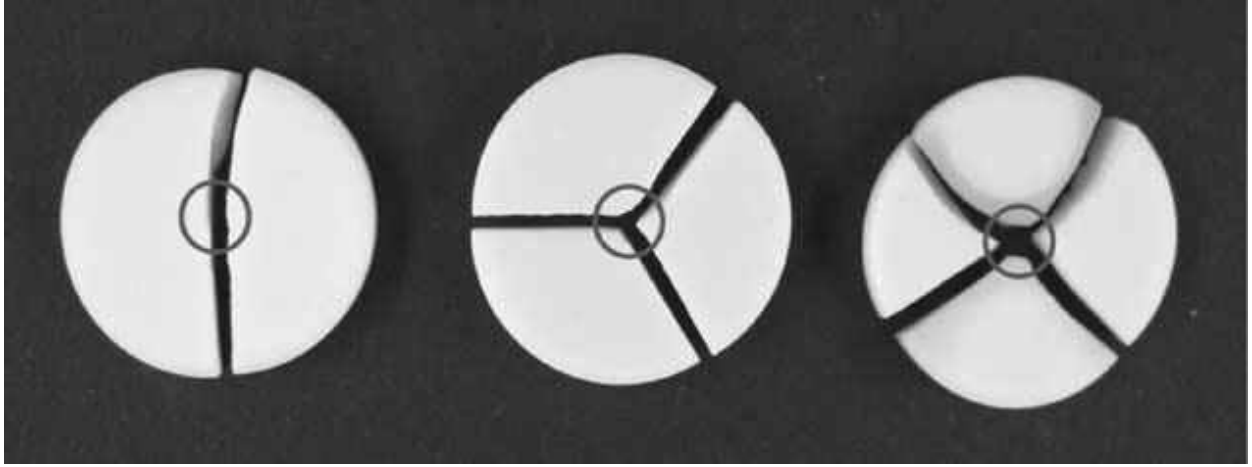
Figure 8: Different types of fracture patterns on as-sintered Al$_2$O$_3$ ceramic discs resulting from ball-on-three-ball biaxial test. The circled area indicates the origin of the fracture [47].

The ball-on-three-balls is a technique that can also be utilized for the biaxial strength testing of brittle ceramic rectangular plate samples. In comparison to other biaxial strength methods for rectangular plates where samples have to be machined with high accuracy to avoid warping while testing, the ball-on-three-balls do not require such preparations allowing for an easier and faster test execution [52]. The loading scheme for rectangular samples is similar to the disc samples previously described and, similar to the disc-shaped ceramics, the number of fragments that result after the test increase with the fracture strength of the material [52].

Finite element analysis of the ball-on-three-balls flexural strength test has provided insights on the behavior of materials undergoing this procedure and has served as a validation tool for the accuracy of this testing method. One of the first assumptions when modeling this test is the exclusion of the effects from friction due to the minimal changes it produces to the stress distribution on the sample and, due to the symmetry of the setup, the simulation of this test can be simplified to only one sixth of the total geometry of the fixture and the ceramic disc, providing more accurate results due to the simplification of the model [47]. Other parameters taken into consideration by Börger et al. [47] for the modeling and simulation of this biaxial

22

strength test was the use of brick elements with 8 and 20 nodes per element for the disc and supporting balls, respectively, with contacts between the sample and the balls defined as surface-to-surface; all materials used for the ceramic disc and the balls were assumed to be homogeneous and isotropic, and only the elastic modulus and Poisson's ratio for each material were defined. The simulation for the ball-on-three-balls and the stress distribution in the ceramic disc can be found in Figure 9.
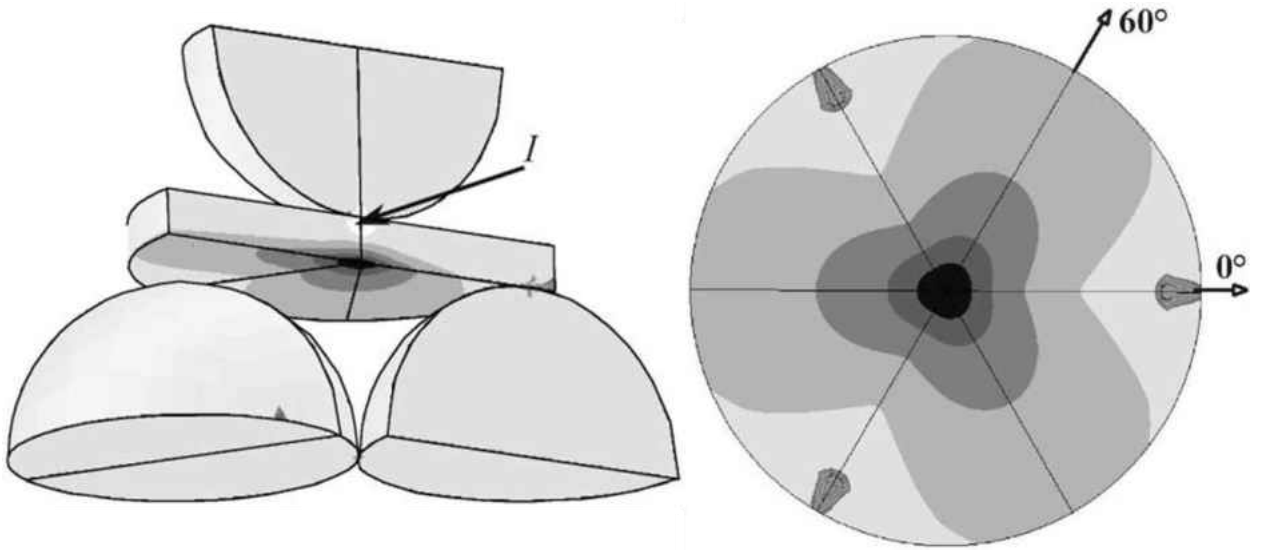
Figure 9: Stress distribution on a brittle ceramic sample ball-on-three-balls simulation of one-sixth if its total geometry. *I* indicates the region of compressive stresses by the loading ball [47].

From the finite element simulation, the stress distribution agrees with the mathematical model developed and the maximum tensile stress is found below the loading ball on the tensile surface of the disc, while the stress distribution happens in a threefold manner due to the three supporting balls. The radial, σ_r, and tangential, σ_φ, stresses distributions at 0° and 60° show a maximum value at the center of the ceramic disc, decreasing as the stress propagates to the edge of the disc. From Figure 10 it is found that under the loading region, the radial and tangential stresses at 0° and 60° are equal and they are also found in the contact area with the supporting

23

fixture. However, for the area outside the loading region, the radial stress decreases in a faster manner than the tangential stress for the direction where the supporting balls are located [47]. For the case when the supporting balls are smaller than the loading ball failure occurs at the support points instead of the loading region, making the results of the test invalid and , therefore, a setup that must be avoided [47].
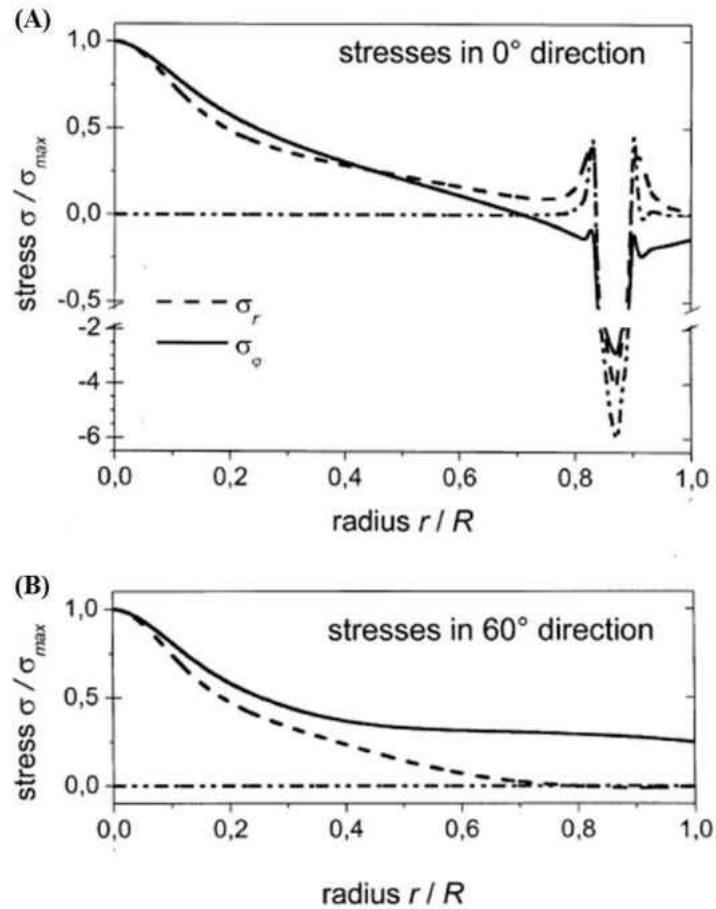
Figure 10: Normalized radial and tangential stress distribution at (A) 0° and (B) 60° along the radial direction of the ceramic disc [47].

The central alignment of the specimen for the ball-on-three-balls test is not significant for the acquisition of good results from this technique since this method is tolerant to the misalignment of samples from the center of the fixture and, for configurations where the support

balls are not fixed, friction can also be neglected since it contributes in approximately less than 1% to the stress distribution on the ceramic disc [53]. The ceramic sample's thickness and Poisson ratio are of major significance for the accuracy of the test and a relationship between the sample and testing fixture must be optimal for acceptable results [47,53,54].

Another popular method for the study of the biaxial flexural strength of ceramic materials is by using the ring-on-ring configuration. Among the different biaxial flexural techniques, the ring-on-ring provides accurate results for both disc and plate-shaped samples and, compared to the ball-on-three-balls in which the stress field is found to be in a threefold manner, the stress distribution on the samples subjected to ring-on-ring test is circular and uniform throughout the tensile surface of the ceramic [55,56]. However, for the ring-on-ring test a flat and parallel surface geometry of the ceramic sample is required as well as relatively strict requirements for the diameter-to-thickness ratio of the disc which allows to control the amount of sample's displacement, ensuring the disc will not flex excessively during testing and the direct proportionality between the applied load and the resulting biaxial stress can still be maintained [57]. Figure 11 shows the setup for the ring-on-ring test and all the elements of the testing fixture and how they interact together. The numerical stress analysis of glass plates tested in ring-on-ring geometry showed that the stress magnifications at the loading ring are significant when the plate deflection exceeds one half of the specimen thickness [57]. In addition, the friction between the ceramic sample and loading and supporting rings exists but it is typically ignored in the analysis. Other techniques, such as ball-on-ring or ball-on-three-balls, have also been merited for biaxial testing of ceramics. In the ball-on-ring test the precise knowledge of stresses produced in the sample during loading, combined with an easy alignment of the sample for the test, gives significant advantages for the use of this method.
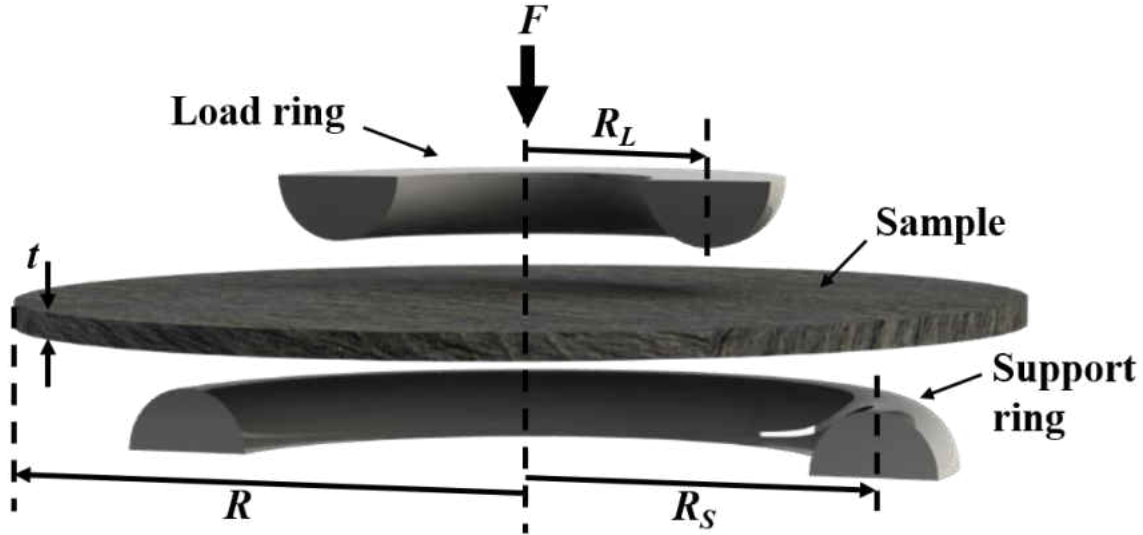
Figure 11: Ring-on-ring testing jig, its components and geometry of the rings and the sample.

In the ball-on-three-balls test the additional advantage is also considered, when choosing the technique for biaxial tests the requirements for the flatness of ceramic sample are not such stringent as in the case of ring-on-ring or piston-on-three-balls, therefore, sintered samples can be tested without any additional surface preparation. These considerations are important for choosing a specific technique when testing for biaxial strength of ceramics because any deviations that can occur from the sample geometry relationships and parallelism, and its interaction with the testing fixture may introduce different stress distribution and percent errors that can directly affect the measurements, as is in the case of the ring-on-ring method [58]. In order to avoid these uncertainties and errors in the measurement of the biaxial strength, a jig for biaxial stress test has to be designed around the sample geometry. The guidelines for the ring-on-ring fixture design and the sample's dimensions can be found in the ASTM standard C-1499, where the relationships between sample's geometry and jig dimensions are presented [49]. Due to the popularity and versatility of the ring-on-ring test its range of application varies from dental

material application, such as ceramic dental restorations [59], to the test of biaxial strength for LCD display panels [56] found in today's televisions and cellphones. The ring-on-ring geometry of the biaxial testing jig was adopted for the test of orthopedic alumina and zirconia ceramics and also used in testing of glass [41] as well as ZrO_2 based electrolyte ceramics and other different ceramic materials [55].

In the ring-on-ring test, the maximum stress occurs on the tensile surface of the ceramic material in contact with the supporting ring within the region enclosed by the loading ring. The maximum stress is calculated by following the governing rules of circular plate bending for a simply-supported plate developed by Timoshenko and Woinowsky-Kreiger [60]. Within the region enclosed by the loading ring in the tensile surface of the ceramic sample, the maximum stress as well as the radial and tangential stresses are equal and can be expressed as [42,49,61,62],

$$\sigma_{max} = \frac{3F}{4\pi t^2}\left[2(1+v)\ln\left(\frac{D_S}{D_L}\right) + \frac{(1-v)(D_S^2-D_L^2)}{D^2}\right] \tag{12}$$

where F is the applied uniaxial load, t is the thickness of the ceramic, v is the Poisson ratio of the ceramic material, D_S is the diameter of the support ring, D_L is the diameter of the load ring, and D is the diameter of the disc-shaped ceramic sample being tested. Equation (12) is only valid for small deflection of the plate in comparison with the thickness of the ceramic disc and it assumes that no deformation occurs in the middle of the plane of the plate [61]. For the region located outside of the surface bounded by the loading ring, the radial, σ_r, and tangential. σ_t, stresses for the ring-on-ring test can be calculated as [42],

$$\sigma_r = \frac{3F}{4\pi t^2}\left[2(1+v)\cdot\ln\left(\frac{R_S}{r}\right) + \frac{(1-v)\cdot R_L^2\cdot(R_S^2-r^2)}{R^2\cdot r^2}\right] \; for \; r > R_L \tag{13}$$

$$\sigma_t = \frac{3F}{4\pi t^2}\left[2(1+v)\cdot ln\left(\frac{R_S}{r}\right) - \frac{(1-v)\cdot R_L^2\cdot(R_S^2+r^2)}{R^2\cdot r^2} + 2(1-v)\cdot\frac{R_S^2}{R^2}\right] \; for\; r > R_L \qquad (14)$$

where R_S is the supporting ring radius, R_L is the loading ring radius, R is the ceramic sample disc radius, r is the radial length from the center of the ceramic disc to the edge of the sample, t is the thickness of the ceramic disc, and v is the Poisson ratio of the ceramic sample.

In order to determine the plate deflection using the ring-on-ring technique, a relationship between the load force, the elastic modulus and Poisson ratio of the material, and the geometry of the testing fixture and the sample must be followed. A mathematical expression was developed and it is contained on the ASTM standard C1499 [49] as,

$$\delta = \frac{3F(1-v^2)}{8\pi E t^3}\cdot\left[\frac{D_S^2}{D_L^2}\left(1 + \frac{(1-v)(D_S^2-D_L^2)}{2(1+v)D^2}\right) - \left(1 + ln\left(\frac{D_S}{D_L}\right)\right)\right] \qquad (15)$$

where E is the elastic modulus of the ceramic material being tested.

For disc-shaped ceramic materials tested by the ring-on-ring method at room temperature, four failure patterns are predominant and provide important information on the type of strength failure that took place during the test and the identification of edge initiated failure which would make the test invalid. Figure 12 shows a schematic on these typical failure patterns and what interpretation of the test can be obtained from them.

Low Energy – Low Strength Failure

Medium Energy – Medium Strength Failure

High Energy – High Strength Failure

Edge Initiated Failure (Invalid)
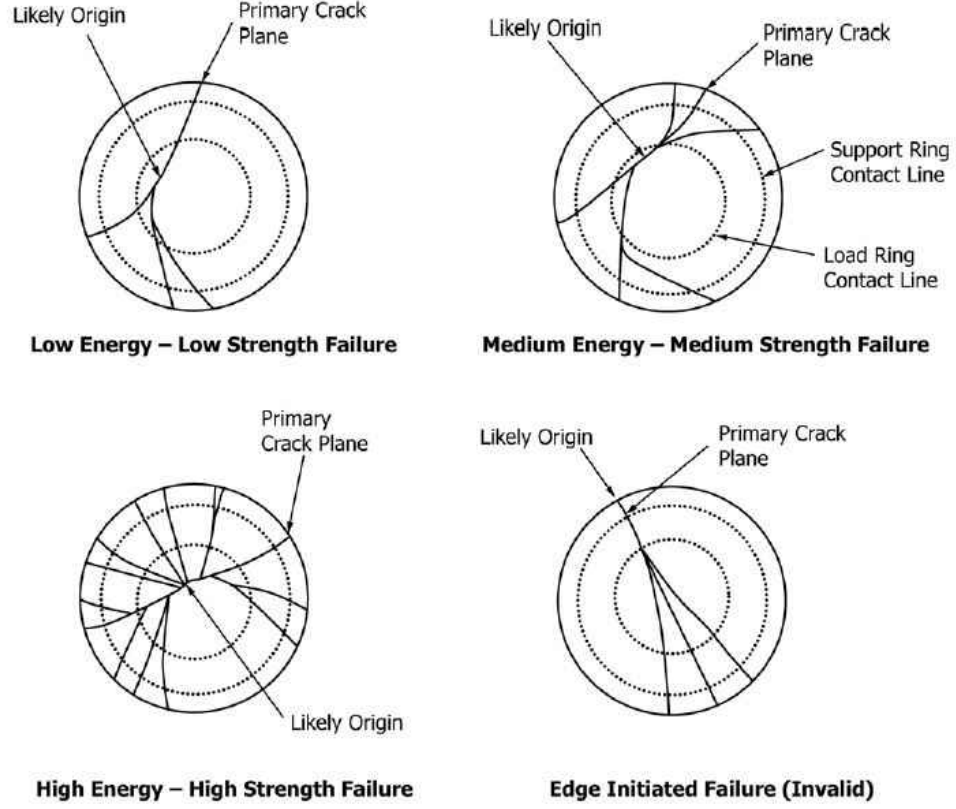
Figure 12: Typical types of failure on disc-shaped ceramic samples tested using the ring-on-ring method [49].

The plate thickness relative to the supporting ring diameter is of importance in the ring-on-ring test since this ratio, along with the elastic modulus and strength of the ceramic sample, determine the deflection of the sample testes at failure [63]. The ideal ceramic plate thickness needs to be within the following relationship,

$$\frac{D_S}{10} \geq t \geq \sqrt{\frac{2\sigma_f D_S^2}{3E}} \qquad (16)$$

where σ_f is the expected equibiaxial flexural strength of the ceramic sample, and E is the elastic modulus of the ceramic being tested. If the thickness of the ceramic disc is maintained within the range established by Equation (16), and when the deflection of the plate is not greater than half of the thickness of the ceramic plate tested ($\delta<t/2$) a linear dependence between the stress and

the load predominates [49,63], thus, for thin ceramic samples when large deflections arise ($\delta > t/2$), a non-linear dependence between the stress and the load applied is generated and the finite element method is required for the accurate calculation of the maximum tensile stress of the thin ceramic disc [55]. The effects of plate thickness on the stress and load on the ring-on-ring test for a ceramic sample with *E=300 GPa*, *v=0.20*, and geometry *D=50 mm*, *t=2 mm* were simulated and the results are found in Figure 13A and Figure 13B, where it can be observed that for displacements on the order of *t/2* an error of approximately 6% is found, while for displacements on the order of *t/4* an error of approximately 2% results [63]. Salem et al. [63] also recommends that the ceramic disc sample to be tested in the ring-on-ring setup should not be thicker than *t=10·D$_S$* since thick plates show a tendency to behave as if they were being loaded by a ball instead of a ring due to the ring ratio being small. Figure 13C shows the effect of plate thickness in the radial stress distribution on the ceramic plate. The breakage of thin ceramic plates by ring-on-ring follows the principles that at low strength failure fewer broken pieces result, while at high strength failure a large number of smaller broken pieces are found [55]. Figure 14 shows an example of thin ceramic electrolytes broken through ring-on-ring exhibiting large displacements including a typical load versus time plot (Figure 14A), failure at low strength (Figure 14B and C) and failure at high strength (Figure 14D and E).
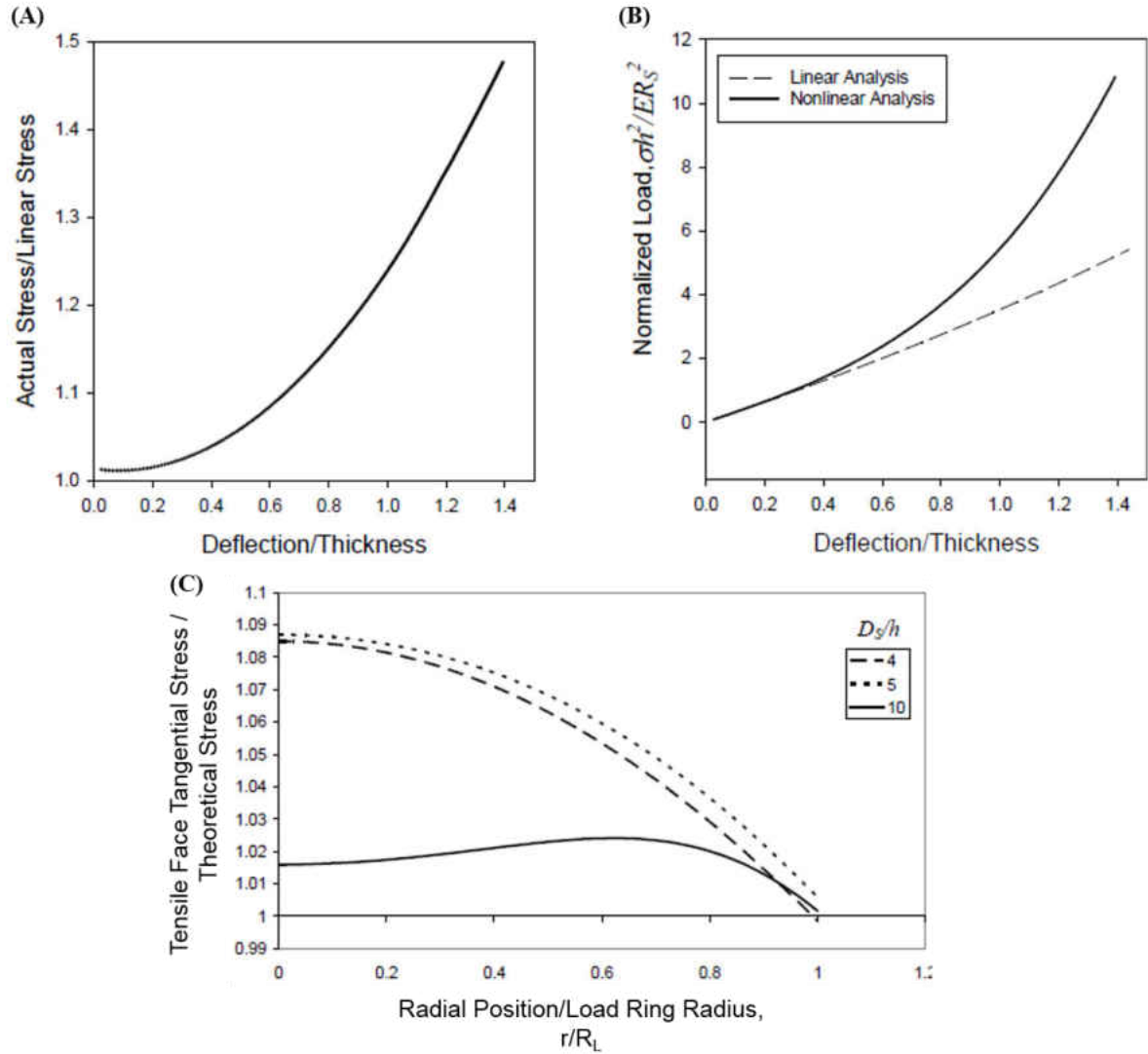
Figure 13: (A) Stress and **(B)** load as a function of deflection normalized to the plate thickness of the ceramic sample for the linear and non-linear solutions The ceramic simulated has properties of *E=300 GPa*, *v=0.20*, and geometry *D=50 mm*, *t=2 mm*. For the load and support rings, *E=230 GPa*, *v= 0.30*, *D_L=20 mm*, and *D_S=40 mm*. **(C)** Radial stress on the ceramic disc sample and the effect of plate thickness for a *D_L/D_S=0.2* and *D_L=8 mm*, *D_S=40 mm* [63].

31
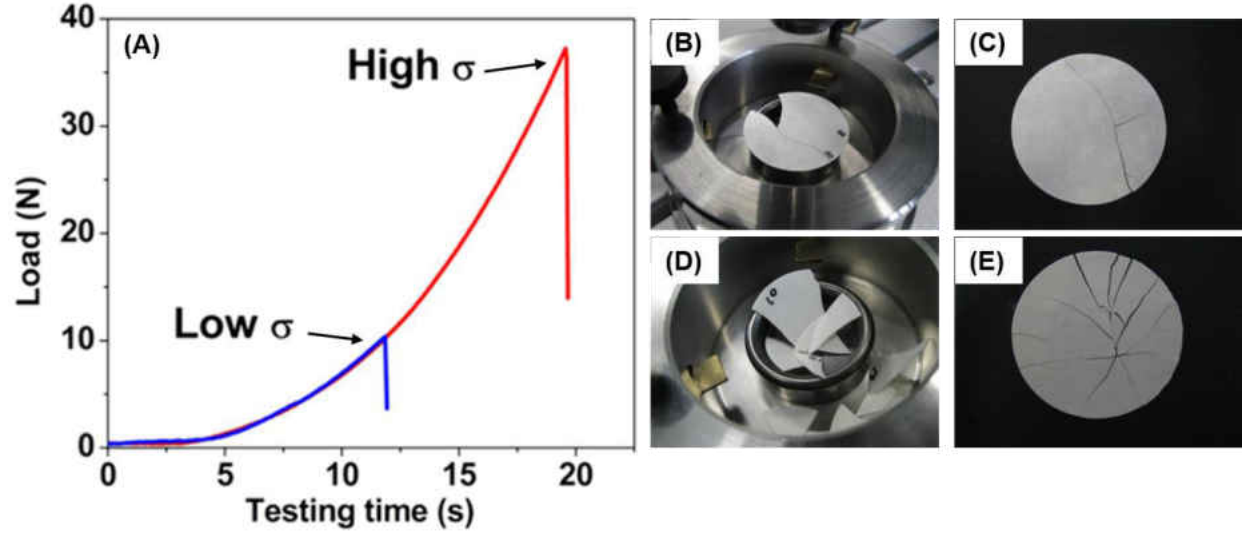
Figure 14: (A) Typical load versus time plot for a ring-on-ring test on thin electrolyte ceramics. (B-C) Electrolyte broken through ring-on-ring at low strength which yielded a small number of broken pieces. (D-E) Electrolyte broken through ring-on-ring at high strength which yielded a large number of broken pieces [55].

Not only the sample thickness affects the results of the ring-on-ring test, but also the relationship between the ceramic disc diameter and the supporting ring as well as the relationship between the loading and supporting rings are essential for the acquisition of reliable and accurate results. These relationships are as follows [49],

$$2 \cdot t \leq D - D_S \leq 12 \tag{17}$$

$$0.2 \leq \frac{D_L}{D_S} \leq 0.5 \tag{18}$$

In order to verify the accuracy of the method and validate its results, the use of the finite element method is necessary since it provides a more insightful analysis on the behavior of the ceramic sample while undergoing biaxial deformation. Typically, the surface experiencing tensile stress is the one more closely analyzed since it is the one that withstands the greatest stress and initiates failure in the sample [42,62,64]. This technique can be used to study how the stress distribution inside the ceramic sample behaves for the radial and tangential directions and how the stress field in the ceramic spreads throughout the geometry of the plate. From the finite

element results, it is observed that the maximum stress on the ceramic disc occurs in the predicted tensile surface in the region enclosed by the load ring, while the radial and tangential stresses decrease as the distance to the center of the disc increases [56,64]. One important observation is that within the region enclosed by the load ring maximum stress occurs and radial and tangential stresses are equal but, as the deflection of the plate is greater than half the thickness of the sample the stress field is not uniform and the peak stress occurs below the contact region between the load ring and the sample [56,63]. This peak stress can also result when the contact stresses between the load ring and the sample are significantly large which can bias the failure towards the contact point and affect the determination of the strength of the material [63]. A typical ring-on-ring simulation on electrolyte samples can be found in Figure 15 where the circular distribution of the stress field can be seen and it can also be observed that the peak stress occurs in the contact region between the load ring and the sample, agreeing with the behavior explained by Salem et al. [63] for large displacements on samples with thickness in the order of *t/2*. The effect of plate thickness in the radial stress can be observed in Figure 16.
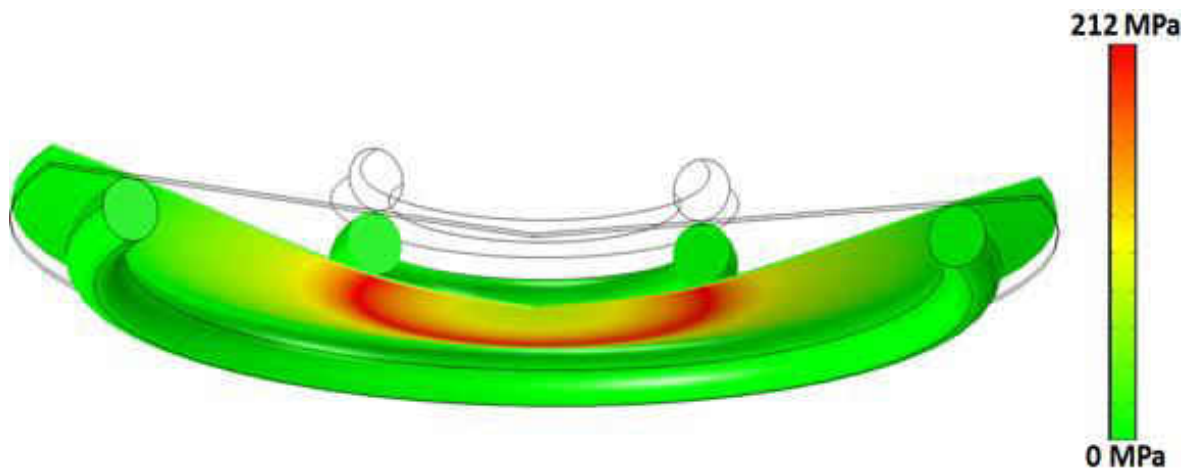
Figure 15: Ring-on-ring FE simulation of a solid oxide fuel cell electrolyte showing the stress field distribution in the ceramic thin plate [55].
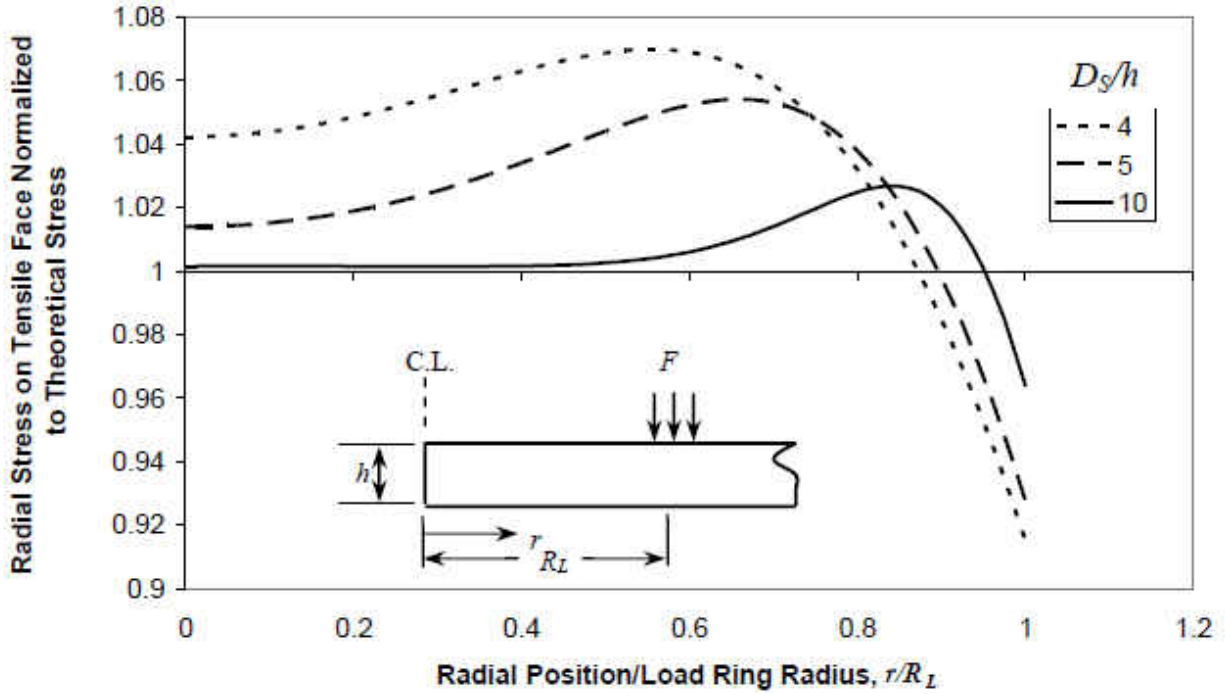
Figure 16: Effect of plate thickness on the radial stress distribution of a ceramic sample with E=300 GPa, v=0.20, D=50mm, and deflection t/4. For the rings, E=230GPa, v=0.30, D_L/D_S=0.5, D_S=40mm, D_L=20mm [63].

The methods for the determination of biaxial flexural strength of ceramic samples have proven to be effective and depict a clearer picture of the strength of ceramics under more realistic conditions. One of the methods that have been widely used and studied is the piston-on-three-balls [42,65], where a disc-shaped ceramic is supported by three balls positioned 120° apart from each other and is centrally loaded by a cylinder of hardened steel [66]. The advantages of this technique are that contact with the support is guaranteed even for warped samples due to the single contact point with each ball, and that the maximum theoretical stress follows the same mathematical model from Equation (8) [42]. The popularity of the piston-on-three-balls is such that it was even included as an ASTM standard with denomination F394-78 [67].

The ball-on-ring biaxial test is another method that is widely used for the determination of the biaxial flexural strength of brittle ceramics [42,68,69,70]. In this technique a ceramic sample is

centrally loaded by a ball while it is being supported by a ring creating biaxial stress in specimen [42,68]. As any other biaxial flexural strength technique, the maximum stress is found on the tensile surface in contact with the support ring within the region enclosed by the loading ball, and since the maximum equibiaxial stress as well as the radial and tangential stresses are independent from the number of support points [68], the ball-on-ring follows the same relationship established in Equations (8), (9) and (10) for the ball-on-three-balls [42].

Another method for biaxial flexural strength is the 3-balls-on-3-balls where a disc-shaped ceramic sample is supported on three balls located at 120° apart from each other, while the sample is loaded by three balls that define a circle of smaller radius than the supporting balls, at 120° apart from each other and, from the supporting balls, they can be aligned or located at 60° apart from each other [50]. The maximum fracture stress of this technique as well as the geometrical relationships between the sample and the testing fixture was studied in depth by Fett et al. [50] and it was found that the effective surface tested resulted to be smaller than other biaxial flexural strength methods.

3.1.3. Uniaxial Flexural Strength Techniques of Three- and Four-Point Bending

Uniaxial flexural strength techniques have been widely used to determine the uniaxial tensile strength of brittle materials subjected to unidirectional loading. Flexural strength, or the ultimate strength of a sample under bending, can be measured, at certain extent, on the materials subjected to this type of load by the use of two widely known methods: three-point and four-point bending [71]. These methods are applied to determine the flexural strength of different types of materials ranging from plastics, ceramics and metals and their popularity is such that they have been standardized by entities, such as ASTM with the designation of C1161 for testing of ceramics at ambient temperature [34], indicating that the results provided are reliable and can

35

be reproduced as long as the same conditions are maintained when testing materials. Even though these techniques provide acceptable results for the determination of the flexural strength of ceramics, their setup is easier than tensile tests for brittle materials but, due to the uniaxial nature of the test, the results are less accurate than the ones provided by biaxial flexural methods since in real-life applications ceramics are loaded biaxially [42,47,71].

Three- and four-point bending have been used as popular methods to determine the ultimate strength of beam-shaped material in bending. The principle from which these tests are based can be found in Timoshenko et al. [60] where it is described that due to the nature of the bending stress in which the samples are tested and assuming that the material is isotropic and homogeneous, the maximum stress is obtained from simple beam theory of a beam in flexure as [71],

$$\sigma_{max} = \frac{Mc}{I} \tag{19}$$

$$\sigma_{max} = \frac{16F \cdot l}{\pi D^3} \tag{20}$$

where Equation (19) is for rectangular bar samples and Equation (20) is for cylindrical rod samples made from materials that are assumed to behave according to Hooke's law. From these equations, M represents the applied moment on the sample, c is the distance from the neutral axis of bending to the outer surface of the rectangular bar, I is the moment of inertia of the cross section about the neutral axis of the bar, F is the load applied, l is the moment arm, and D is the diameter of the circular cross-section of the cylindrical rod. The value for the moment arm, l, varies according to the test being equal to $L_0/2$ for the three-point bending and $(L_0 - L_i)/2$ for the four-point bending. These techniques assume that the moduli of elasticity in tension and compression are identical and the material is linearly elastic [34]. Figure 17 provides a schematic view of the three- and four-point bending techniques with the location of the loading points and

the geometry of the sample and the fixture. From these tests, the maximum stress is found to be located in the middle section of the sample right under the loading point for three-point bending, or in between the two loading points for four-point bending [71].
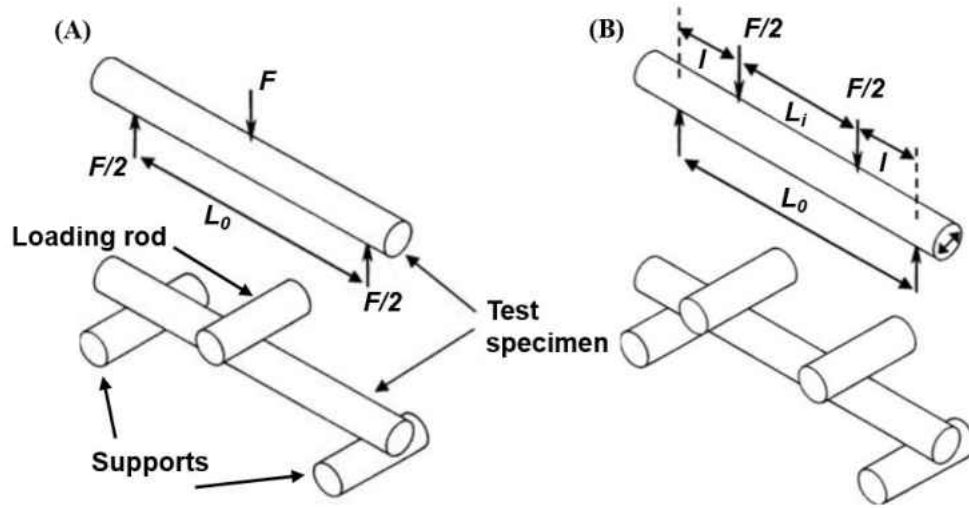
Figure 17: Flexure test done by (A) three-point bending, and (B) four-point bending. The location of the loading points relative to the span of the sample on the test is used to determine the method used [71].

From the simple beam theory and the use of Equations (21) and (22), the strength of a rectangular beam in three- and four-point bending can be found as follows [34],

$$\sigma_{max,3-point} = \frac{3}{2} \cdot \frac{FL}{bd^2} \qquad (21)$$

$$\sigma_{max,4-point} = \frac{3}{4} \cdot \frac{FL}{bd^2} \qquad (22)$$

where F is the force required to break the sample, L outer spam of the support bars, b is the width of the sample being tested, and d is the thickness of the sample being tested. The techniques of three- and four-point bending are prompt to several common mistakes that can result from extrinsic sources such as fixture or sample misalignments, user error in load measurements, or incorrect size and relationships between the sample and the testing fixture [71]. One common

source of error in uniaxial flexural strength testing comes from edge finishing defects from the sample and how they can alter the results for the strength of a material which, compared to the counterpart of biaxial testing where a larger effective surface area can be tested without the presence of these defects, it presents a major disadvantage [41]. Other common source of error can come from the load point friction between the sample and the fixture, the occurrence of eccentric loading, wedging, and the use of wrong spans between the loading and supporting points of the testing frame [71].

3.1.4. Uniaxial Compression

Ceramics are very often subjected to compressive forces in real life applications, to the point where the study of their compressive strength was of importance and the methods to obtain it were standardize by agencies such as the ASTM in their standard designated as C1424 [38]. Ceramics have demonstrated to be 10 to 15 time stronger in compression than in tension which can lead to tensile failure when testing for compression if the setup is wrong resulting in erroneous measurement for compressive strength [72] For the uniaxial compression test, parallelism between the surfaces of the sample being tested and the compression plates of the machine used to load the specimen is required, as well as a sample that macroscopically exhibit isotropic, homogeneous, continuous behavior and a uniform geometry to avoid misalignment of the uniaxial compressive load through the center of the sample geometry, and with it, eccentric loading which can result in non-uniform compressive stress distribution on the sample and tensile failure from bending stresses [38,72,73]. Compressive stress is calculated using the equation for uniaxial force applied over a defined area [72],

$$\sigma_{max,c} = \frac{F}{A}$$

(23)

with *A* for a circular cross-section being calculated as [38],

$$A = \frac{\pi d^2}{4} \qquad\qquad (24)$$

where F is the force applied, and A is the cross-sectional area of the gage section under compression, and d is the diameter of the gage section. For the compression test, the geometry of the specimen can vary from the regular shape of contoured specimens with defined gage sections that possess minimal stress concentration at the transitions from the area in contact with the compression platens and the area with reduced diameter, and samples with the form of right circular cylinders [38]. Strain measurements can be performed during the compressive test by the use of optical instruments or by the means of strain gages, and be used to determine elastic constants in the linear region of the stress-strain curve that results from the compression test [38]. Figure 18 shows a typical setup of the compression test for the two specimen geometries defined.
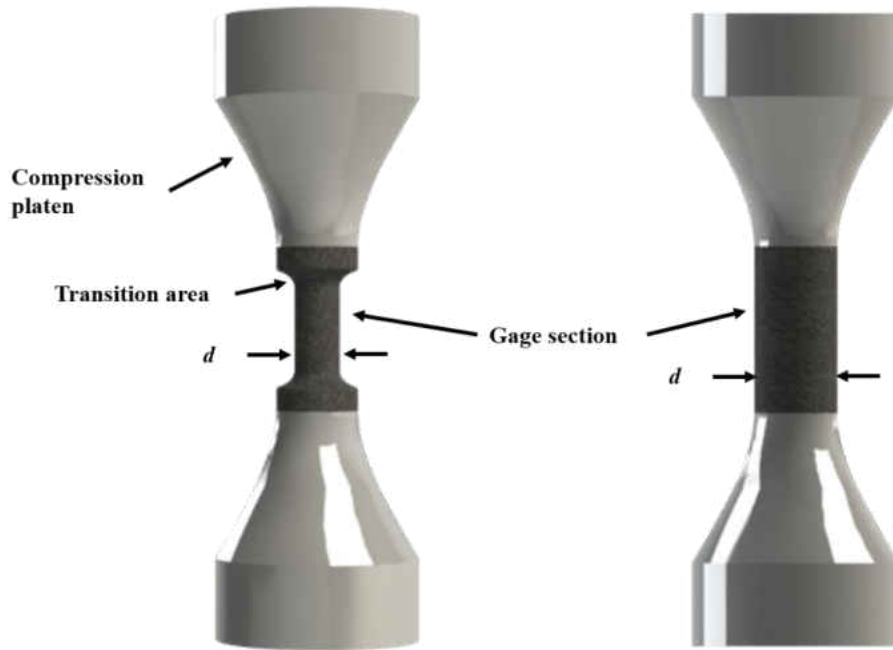
Figure 18: Typical setup for the compression test for (A) a contoured specimen, and (B) a right circular cylindrical specimen [38].

The application of ceramics for structural purposes is of importance for the development of new technology and materials that can satisfy current needs. For such reason, the study of the mechanical properties of ceramics is necessary and the understanding of the behavior of these materials under certain load conditions found in real-life applications is of great interest. Different compositions of ceramics can be used as structural materials ranging from nitrides, oxides, carbides, borides and even ceramics that possess an aragonite structure. Materials such as Si_3N_4 have been researched intensively and they serve as structural materials for light-weight applications where high thermal shock resistance and fracture toughness are required [74,75]. Ceramics made from oxides such as ZrO_2 and TiO_2 have been used in the past to manufacture parts that operate in aggressive environments of temperature and corrosion and as catalyst material for solid electrolytes in fuel cells and environmental applications [76,77]. Other important structural materials that have been greatly studied are carbides with applications as refractory materials for applications on environments with high temperatures that require high hardness [75].

3.2. Ceramics of the Living: Case Study for CaCO₃ and the Aragonite Structure of the Staghorn Coral *Acropora cervicornis* Skeleton

On the past three decades, approximately 30% of the total worldwide coral population has declined and new coral diseases have appeared that seem to be affecting most of the coral species, including the *Acropora cervicornis* [78]. At the global scale, the disease that is harming most corals of the world is coral bleaching which is caused by the disruption of the symbiotic interaction between the coral and the endosymbiotic algae that inhabits it [78]. This disruption causes the coral to lose the algae and the photosynthetic pigments that exist in it resulting in the whitening or bleaching of the coral, causing the death of the coral reef and leaving behind the

inorganic component of $CaCO_3$ aragonite structure of the coral skeleton [79]. An example of coral bleaching in an *Acropora cervicornis* sample can be seen in Figure 19.
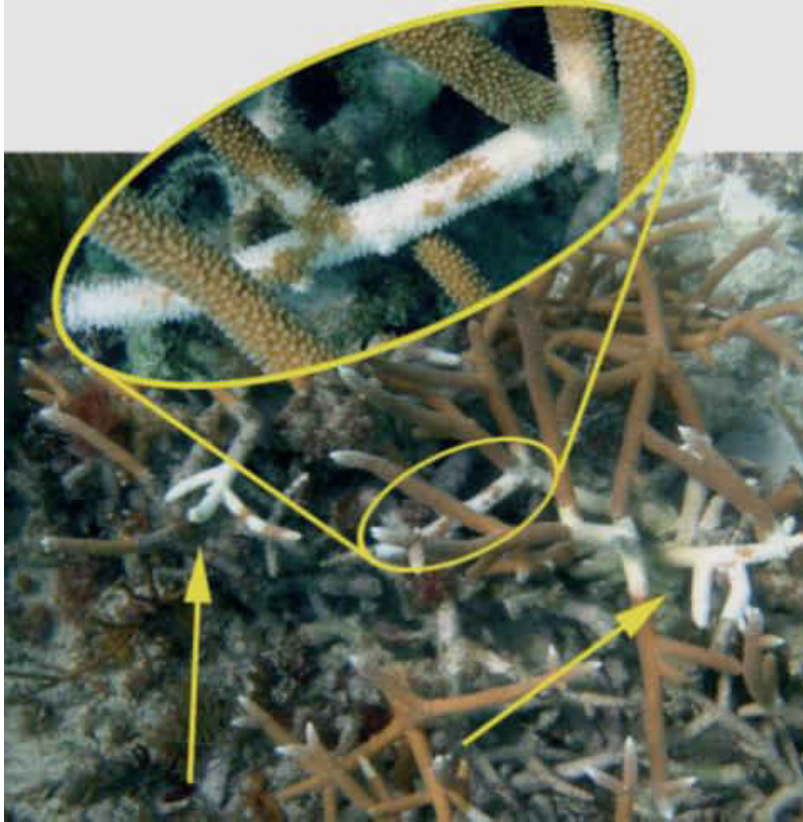
Figure 19: Bleaching of *Acropora cervicornis* coral [80].

Bleaching has been affecting different colonies of *Acropora cervicornis* where large fields of these corals can be found completely white with no other living beings surrounding the coral colony, indicating that these skeletons do not serve as habitats for other species once they are bleached and dead [78,80].

The projection in the rise of the sea water level is also threatening the spread rate of coral reefs in the oceans. It has been found that there is a direct correlation between the development and growth of coral reef and the level in water of the sea around them [81]. The increase of water

depth around the coral reef promotes a change in its interaction with the environment by interfering with the hydrodynamic conditions and the wave loads corals experience [82].

The increase in water temperature due to global warming and the acidity levels of the ocean waters constitutes another major problem that compromises the structural strength of coral skeletons. A direct correlation has been found between the rate of calcification of corals and how it is reduced when waters become warmer and more acid, thus leading to the formation of weaker skeletons and structures that are more prone to damage [83,84,].

3.2.1. Structure and Reproduction of the *Acropora cervicornis* Coral Skeleton

Most coral skeletons of the *Acropora* family are mainly formed by an aragonite structure made from calcium carbonate ($CaCO_3$) with a density of 2.94 g/cm^3 [85]. These corals are of the branching type, meaning that they grow by extending branches, called axial corallites, which for the *Acropora cervicornis* is of a staghorn-like shape, reason why it was given this name (Lamarck, 1816). This type of growth allows for a faster extension of the axial corallites and helps the coral to compete for space and light which is fundamental for its survival [86]. The reproduction of these living beings relies on the fragmentation of its skeleton and the health condition of its fragments, which are carried by the water currents away from the main structure, falling later to the bottom of the sea where they get fixed and start a new structure, increasing this way the size of the coral colony [87,88]. The fragments typically belong to newly formed branches, that when exposed to high hydrodynamic forces and high wave loads break due to be younger structures with weaker properties. The break load is highly dependent on the strength of the material which is greatly affected by the porosity of the structure, that, for a healthy colony of *Acropora cerviconis* it has been reported to be between 14-27% [89]. For the *Acropora* family, porosity varies in a wide range depending on the coral type, varying from 30% to 70% [90]. The

porosity in the coral skeleton is tied to the level of calcification during its formation which is affected in a negative manner by the acidity and warmness of the water where the coral develops. Madin et al. [85] reported a decrease by 21% in the calcification of corals which produced a decrease of 6% in the density of the specimens for a period of 16 years, therefore less $CaCO_3$ was found in the skeletons which produced a weaker structure on the branches analyzed. The skeleton of the *Acropora* family was determined to be a linearly elastic material with an elastic modulus ranging from 9-38 GPa, with tensile failure being the most typical failure form branching corals experience under the hydrodynamic forces and wave loads present in their natural environment [90]. A summary of many mechanical properties for different specimens of the *Acropora* family can be found in Table 1[90].

Table 1: Mechanical properties of different members of the *Acropora* family

Specimen	Density (g/cm^3)	Porosity (%)	Compressive strength (MPa)	Tensile Strength (MPa)	Elastic Modulus (GPa)
Acropora Palmatta	-	30	21-80.8	-	8.7-38
Acropora Reticulata	2.78-2.87	33-62	62-89.8	10.3-40.9	24.8-82.4
Acropora Spp.					
Acropora intermedia	2.42	12-40	28-99	8.84-12.7	55-77

Little is known about the mechanical properties and behavior of coral reefs, which makes the research in this field very important and interesting since it can open the doors to significant discoveries that can contribute for the noble goal of saving these living organisms from the uncertain future that they are facing.

3.3. <u>Raman Spectroscopy</u>

The analysis of material using this technique can be performed using several configurations that involve the scanning of points or an area on the surface of the material of interest that can be configured using a motorized XY-stage. The wavelength of the incident light is chosen according to the purpose of the analysis and it is adjusted for the type of sample being analyzed, being light on the blue/violet spectrum used when strong Raman scattering with a broader spectral window is required, and red light when the focus into a region composed by wavenumbers lower than 200 cm^{-1} is desired to be analyzed [91]. Figure 20 shows an example of a common Raman spectrometer instrument and configuration.
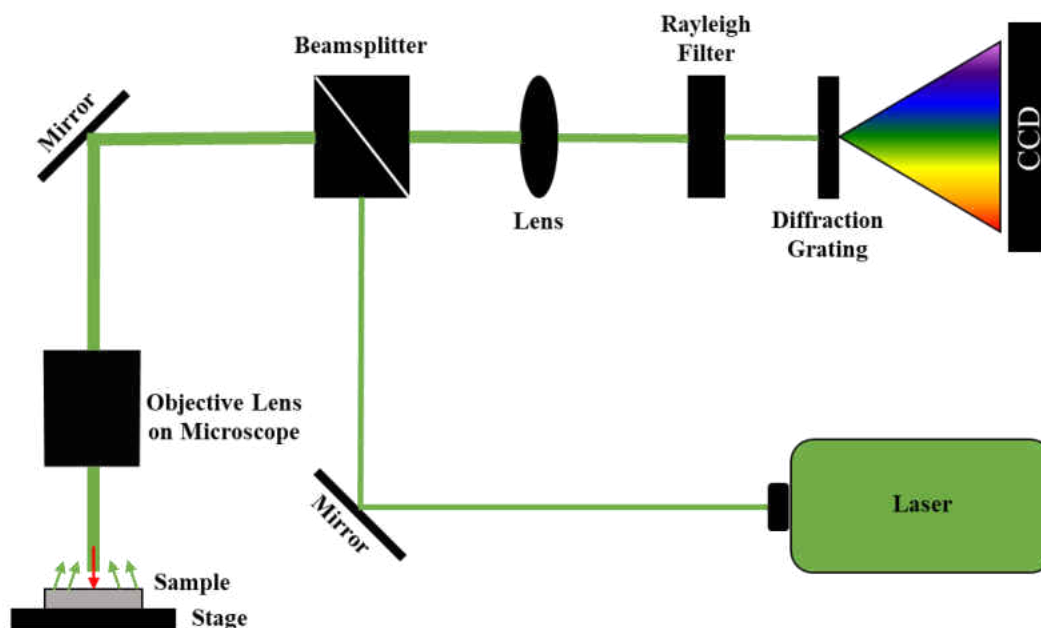
Figure 20: Common Raman spectrometer configuration [92].

3.3.1. Energy Modes and Raman Spectra

The interaction between matter and light make the photons present in the latter to be absorbed, reflected, or scattered, creating vibrations in the molecules that compose the physical object [92]. Raman spectra are produced when there is an electronic transition in excited diatomic

molecules after these are energized by scattered photons coming from a source of light, ideally with a constant wavelength, as is found in lasers [18]. Figure 21 shows a diagram with the different transition energy levels in the diatomic molecule. Photons take the molecules they interact with to a higher energy state for a short period of time, coming back immediately to a ground energy level after they relaxed [92]. This phenomenon is also knows as elastic or Rayleigh scattering and it occurs in 99.99% of the scattering process, where the photons emitted by the molecule have the same energy level as the photons coming from the source of light.
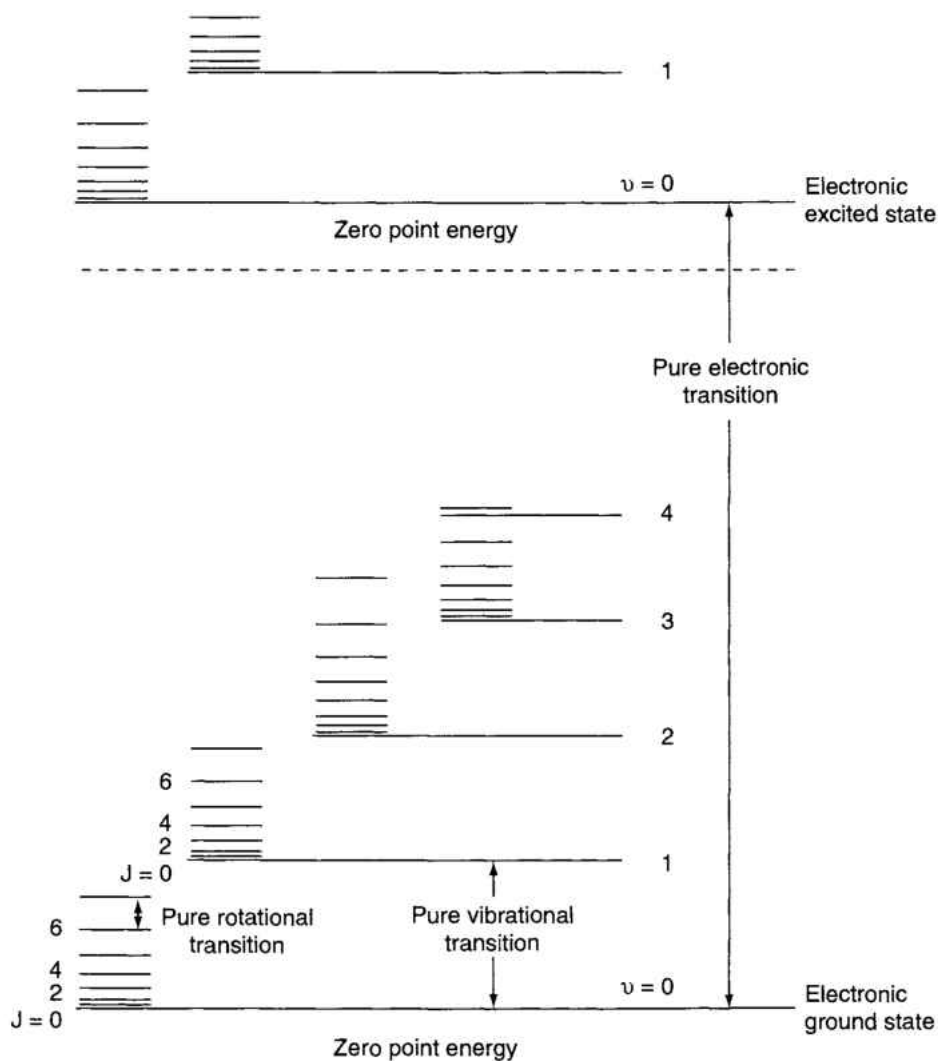
Figure 21: Energy levels of the diatomic molecule [18].

Furthermore, it is found that in less typical occasions, the molecule relaxes to a different energy state, scattering photons with a dissimilar energy level as the ones coming from the source of light. This energy level can be higher or lower than the one coming from the incident light and it causes a measurable shift or change in the wavelength of the light, also known as inelastic or Raman scattering [18,92]. Moreover, inelastic scattering is divided into two types names Stokes and anti-Stokes, the former occurs when the photons stimulate a molecule from the ground level to a higher energy state, making the molecule have less energy than initially and shifting the scattered photons to a longer wavelength, also called as red-shift; the latter is found when a molecule is already at a higher energy state and it is downgraded to the ground state due to the transferring of energy from the molecule to the photon creating a shift to a lower wavelength, also called blue-shift [92]. Figure 22 shows a schematic illustrating the energy transition within a molecule when interacting with a light source.
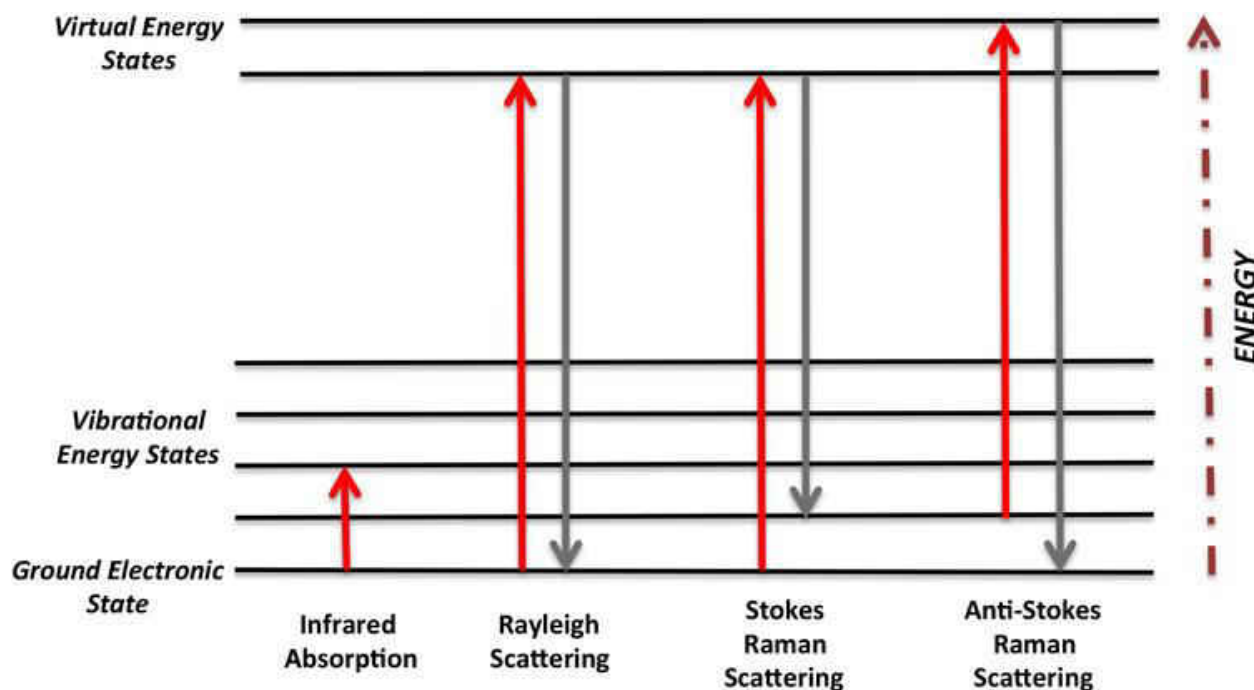
Figure 22: Energy transition in a molecule showing Rayleigh, Stokes, and anti-Stokes scattering [92].

From two types of Raman scattering, Stokes are more common than anti-Stokes since due to the law of thermodynamics, at room temperature, a molecule is more likely to be found in its natural ground energy level rather than at an excited level. Determining whether a molecule is Raman active or not depends on the change of polarization present at the molecule which is determined by the measurement of distorted electron cloud around the nuclei of the molecule given by,

$$\mu = \alpha E \tag{25}$$

where α is the polarization, μ is the electron dipole of the molecule and E is the interaction of the electron cloud with the emitted light [92]. The polarization of a molecule is related to the intensity of Raman radiation scattered, thus the greater the change in polarization the greater the intensity of the Raman spectra collected.

3.3.2. Analysis of Materials Using the Raman Technique

Materials can be analyzed by many means, but it is always preferred to use non-invasive methods that guarantee reliable results without compromising the integrity of the structure. By utilizing the Raman technique and understanding the behavior of the peaks generated by it many features of a material can be identified, such as external stresses, defects and grain boundaries, among others, as can be seen in Figure 23, which explains how the peaks shift, reduced their intensity or get narrower by different perturbations on the material.
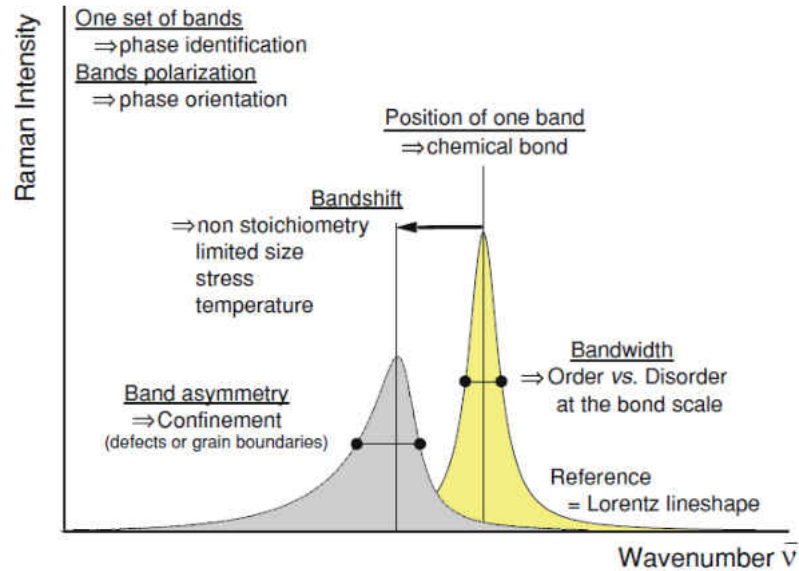
Figure 23: Possible alteration of Raman peaks from many defects and external factors that ceramic materials may be exposed [93].

Many modern Raman spectrometers come furnished with motorized stages that coupled with data acquisition software allow for the automatic collection of the Raman spectra corresponding to a surface area that can be mapped. The map is done by the systematic movement of the motorized stage guided by a local coordinate system defined by the data acquisition software, which outlines a grid on the surface of the material and collects the spectra on each point that are later analyzed as a bulk [93]. A graphical representation of the mapping process can be found on Figure 24.
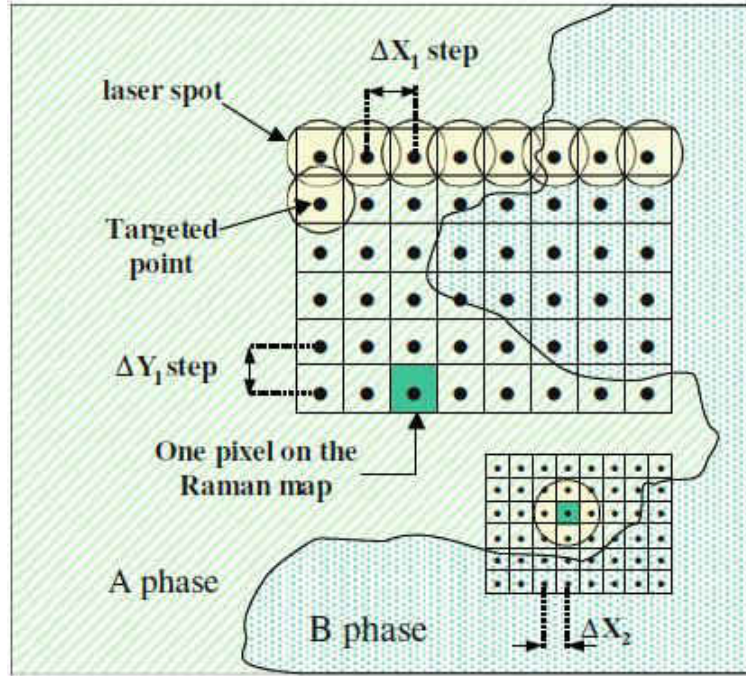
Figure 24: Graphical representation of the Raman mapping process on the surface of a material [93].

An analysis of a material can be achieved by the accurate collection of Raman maps and the interpretation of the data provided by the peaks collected summarized in four major factors that involve the peak intensity, width, shift and area using fitting through mathematical methods. The vibrational response and shape of the Raman spectra collected will depend on several parameters in the material such as material defects (voids, agglomerates, and cracks), grain geometry, phase orientation and secondary phases, and external mechanical stresses induced to the material of interest [93]. Therefore, the objective lens of the microscope used for the collection of Raman spectra should be one that can focus on the level of details desired to be capture from the surface of the material. Thus, the numerical aperture of the lens is of great importance and can be calculated as follows [93],

$$NA = n \cdot sin(\theta_{back}) \qquad (26)$$

where n is the refractive index that belongs to the medium carrying the light between the sample surface and the objective lens, which for air is typically 1, and θ_{back} is the greatest collection angle that can be possibly achieves for the backscattered light. A graphical description of this phenomena and the acquisition of backscattered light by a Raman microscope can be found in Figure 25. The numerical aperture is also important because it determines the resolution of the map which is the smallest distance that can be acquired between two measured points and it is approximated by [93],

$$R \sim \frac{0.16\lambda}{NA} \qquad (27)$$

where R is the resolution of the microscope, λ is the wavelength of the observed light and NA is the numerical aperture of the objective lens. An image for a SCS-6 fiber analyzed with a Raman map having a resolution of $1\mu m^2$ pixels can be found in , which corresponds to a map made from the intensity of the bands from 1300-1600 cm^{-1} [93].
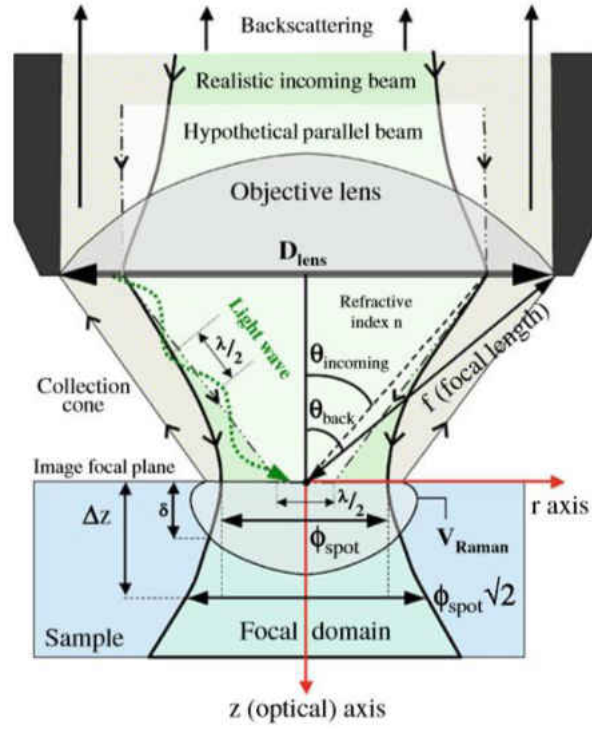
Figure 25: Schematic of the objective lens in a Raman microscope and the process of collecting backscattered light for Raman analysis [93].
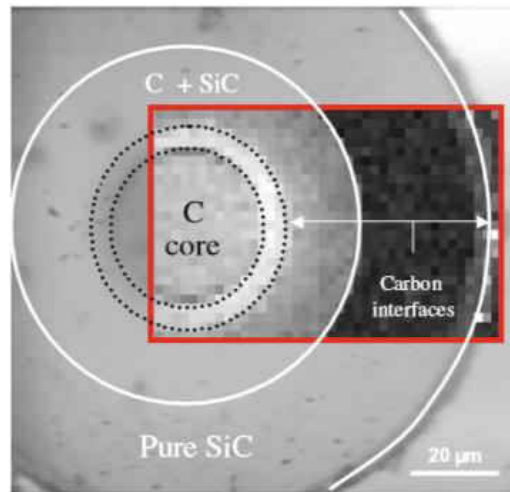
Figure 26: Image of a SCS-6 fiber showing an intensity Raman map over the bands corresponding to the range of 1300-1600 cm^{-1} with a resolution of 1μm^2 pixels [93].

3.3.3. Raman Mapping on Micro-Indented Surfaces

Micro-indentation is a common test used to determine several mechanical properties of materials such as elastic modulus, hardness, strength, among others. This type of mechanical testing is also used in tandem with Raman mapping to observe any phase transition in the material tested due to non-hydrostatic stresses generated by the load locally applied on the surface of the material by the indenter [94,95]. Since the indenter has an imperfect geometry at its loading tip and the pressure applied to the material varies along the indentation, different cracks on the corner of the indentation or material accumulation on the edges of the indentation may result that can captured and mapped using the Raman technique as can be seen in Figure 27 where the intensity map for a ZnSc sample indented by a 50 g load was done.
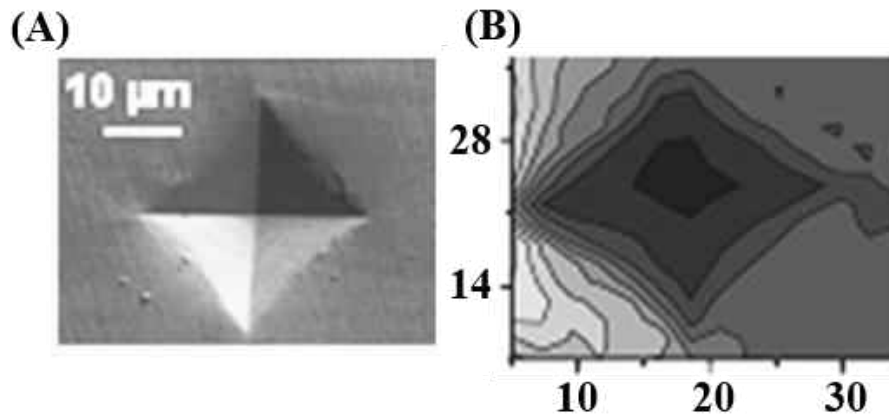
Figure 27: (A) Indentation of a ZnSc sample using a 50 g load; (B) Raman mao of the indentation made on the surface of the sample [93].

3.3.4. Raman spectra of $CaCO_3$

Calcium carbonate ($CaCO_3$) presents three common crystalline structures in nature which are calcite, vaterite and aragonite, with rhombohedral, hexagonal and orthorhombic structures, being calcite and aragonite the most thermodynamically stable [96]. In nature, the occurrence of this mineral, mainly in the aragonite form, is widely found and it is common to several structural

components of the marine life such as coral reef skeletons, clams, pearls, among others, with crystal growth produced by biomineralization [97,98]. It has been found that aragonite structures have an orthorhombic unit cell with lattice parameters of $a = 4.962$ Å, $b = 7.969$ Å, and $c = 5.743$ Å and space group *Pnma* as can be seen in Figure 28.
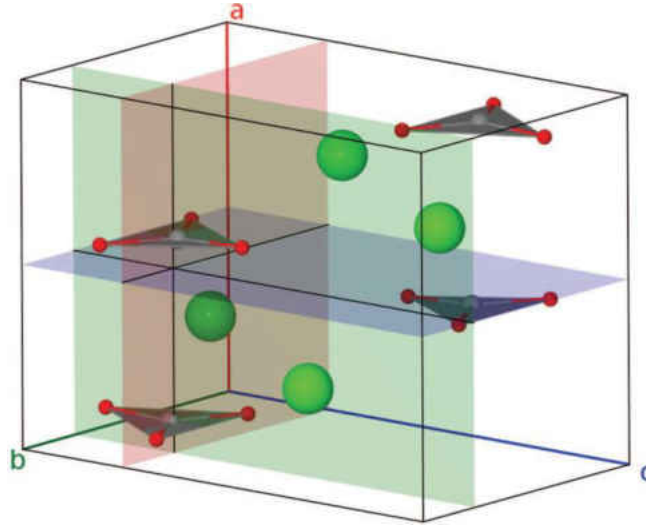
Figure 28: Unit cell for an orthorhombic aragonite structure containing four CO_3^- units and four Ca^{++} ions [96].

Aragonite presents many characteristic Raman modes, from which 23 distinct peaks have been identified by Frech *et al.* [99], being the most prominent found at 1086 cm^{-1}. The mode found at this band belongs to the symmetric C-O stretching in the CO_3^- units [96]. Figure 29 shows typical polarized Raman spectra for the aragonite structure showing the most significant peak at 1086 cm^{-1}.
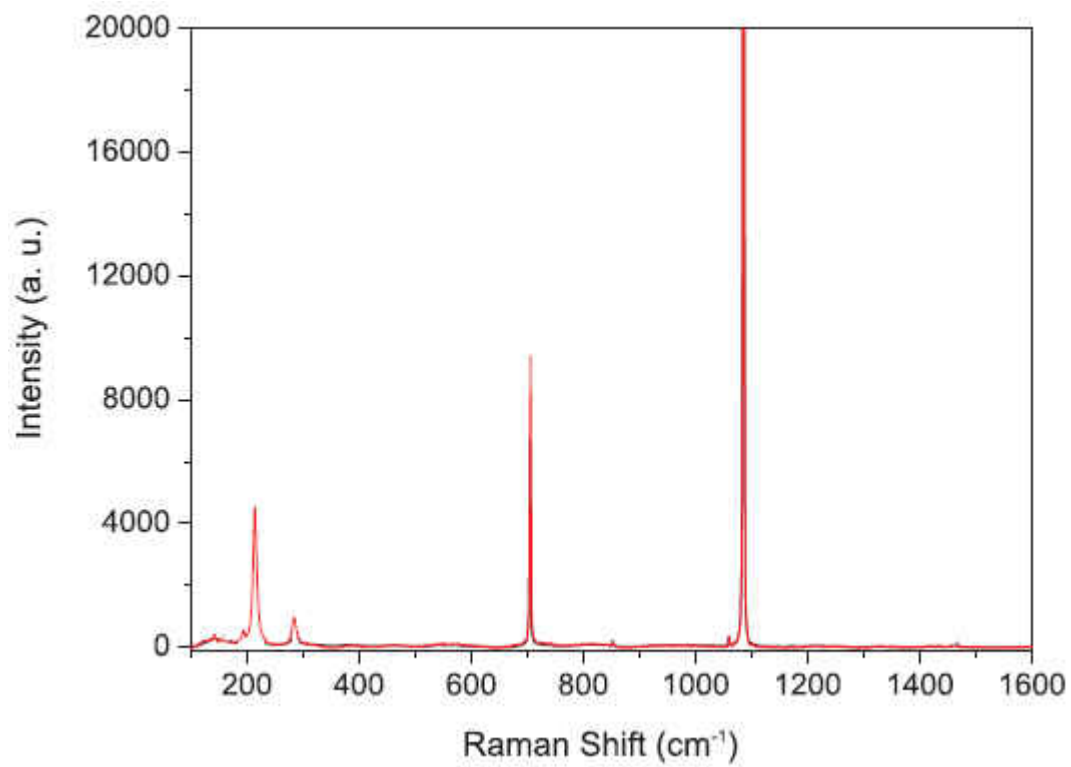
Figure 29: Polarized Raman spectra for an aragonite crystal structure showing the most prominent peak at 1086 cm^{-1}[96].

4. DESIGN AND DEVELOPMENT OF THE RING-ON-RING FIXTURE FOR THE BIAXIAL FLEXURAL STRENGTH OF BRITTLE CERAMICS

For the testing of biaxial strength of brittle ceramics at ambient temperature under monotonic loading, the ring-on-ring technique was chosen as the one which would be the most appropriate to test boride based ceramics with the shape of a disc. The jig developed consisted of a support ring, a load ring, a support of the load ring, and a sphere which is used for the specimen's alignment located between the load ring support plate and the load ring itself (Figure 30A). Equation (12) was used to determine the biaxial strength of the ceramic sample tested.

The design of the jig's components was achieved by following the ASTM standard C1499 [49], which strictly depends on the geometry of the ceramic samples to be tested. The relationship contained in Equation (17) was used for the calculation of the diameter of the support ring. The pre-multiplier 2 to 12 used in the Equation (17) correlates with the surface finish of the ceramic sample with 12 used for the curved and not flat surfaces, which is the case when samples used in ring-on-ring test are as-sintered without any machining. The ring-on-ring testing jig was designed for boride ceramic samples with diameters in the range of 18 to 20.55 mm and thickness varying from 1.0 mm to 1.5 mm, therefore the pre-multiplier was chosen as 3, which yielded a diameter of the support ring, D_S, equal to 15.45 mm. After the calculation of the D_S, the diameter of the load ring was determined using the relationship between the load and support ring in Equation (18). For the D_L the pre-multiplier value was chosen as 0.35 due to the geometry of the sample to be tested and the relationship with D_S. Thus, according to the Equation (18) the diameter of the load ring D_L was calculated to be equal to 5.41 mm. The calculation of the ring tip radius was then done using the equation,

$$\frac{t}{2} \leq r \leq \frac{3t}{2} \qquad\qquad (28)$$

where t is the sample thickness, mm; and the r is the load and support ring tip radius, mm. As the r dimension varied from *0.5t* to *1.5t,* Equation (35), a value of $r = 1.58$ mm was chosen. The dimensions for the bleed holes, the bleed slot and the heights of the load and support rings were determined using ASTM Standard load and support fixture designs for equibiaxial testing [49]. The size of the spherical ball located at the notched center of the top surface of the load ring was determined using the $D_S/12$ relationship. The depth of the notch resulted to be 1.05 mm with an opening that followed two lines separated at 120° from each other which made a circle on the top surface of the notch with a diameter of 3.64 mm. This notch was used as the location of the alignment ball for the load ring. The diameter of the metallic sphere used in the ring-on-ring was of 5mm. The drawings for the developed load and support rings designed in Solidworks® (Dassault Systèmes, Vélizy-Villacoublay, France), are shown in Figure 30A. After the drawings of the ring-on-ring jig components were developed, a 3D printed prototype model was made (Figure 30B) using the 3D printer Stratasys® Dimension SST 1200es (Stratasys Ltd., Eden Prairie, Minnesota, USA), thus allowing to ensure that all dimensions are correct and fit the location of the screw attachments of the MTS Criterion® 43 universal testing machine (MTS Systems Corporation, Eden Prairie, Minnesota, USA) to be used for biaxial strength tests. After all dimensions were verified and prototyped, the model was installed and tested (Figure 30C), then the final version of the ring-on-ring jig was manufactured using 4140 steel which has a HR_C larger than 40. The metallic jig was manufactured using a CNC Fadal® VMC-3016L machine (Fadal Engineering, Brea, California, USA) due to the high precision that was required for the inner and outer radii of the load and support rings, as well as for the parallelism necessary between the surfaces of the aforementioned components of the jig. The jig components as well

as its complete assembly in the MTS Criterion® universal testing machine are shown in Figure 30D-F.

The validation of the ring-on-ring test was made by using the finite element method where the experimental data obtained through the test was compared to the simulated results. The material tested to validate the accuracy of the ring-on-ring testing jig was a boride ceramic composite consisting of ZrB_2-30wt%SiB_6 sintered by spark-plasma since it was readily available for the experiment, and the geometry of the samples were appropriate for the biaxial flexural strength test since the dimensional relationship between the testing jig and the sample was maintained. The geometry of the three ceramic composite discs made from ZrB_2-30wt%SiB_6 that were tested consisted of diameters and thickness ranging from 18 to 20.25 mm and 1.03 to 1.42 mm respectively and a summary of their geometry can be found in Table 2.

Table 2: Summary of the geometry for the samples used to validate the design of the ring-on-ring jig for the determination of biaxial strength of ceramics.

Sample	Diameter (mm)	Thickness (mm)
1	18.64	1.42
2	19.783	1.06
3	20.25	1.37

The elastic properties of the material tested were obtained by the use of Resonant Ultrasound Spectroscopy from which the Poisson's ratio and the Young's modulus were obtained, serving for the calculation of the biaxial flexural strength of the material and also as input for the finite element simulation made for the validation of the test.
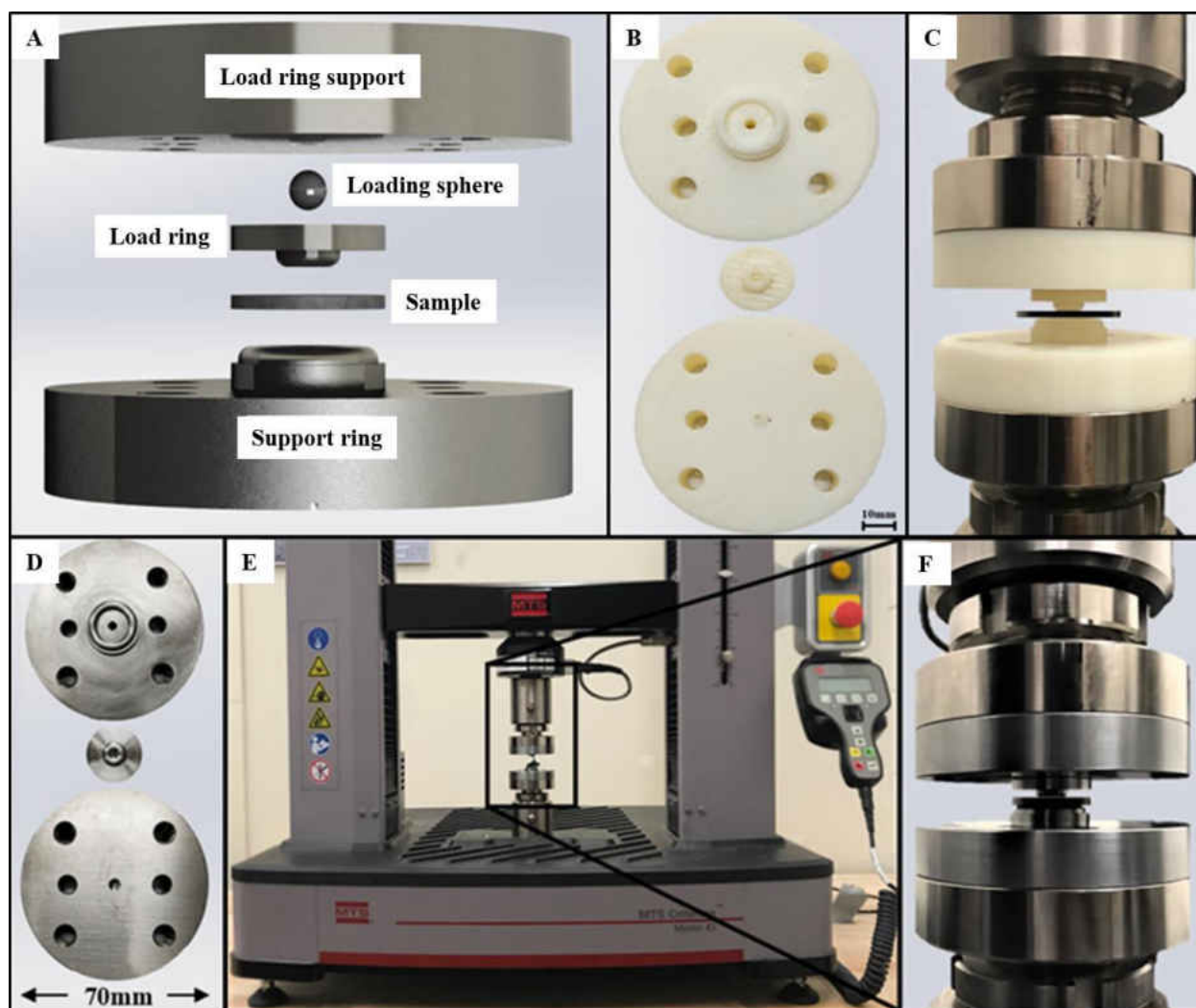
Figure 30: Ring-on-ring fixture designed for the biaxial flexural strength of ZrB$_2$-based ceramics. (A) Schematic of the design. (B) 3D printed prototype of the ring-on-ring fixture and (C) placement on the universal testing machine. (D) Manufactured testing jig. (E) Universal testing machine with the ring-on-ring fixture installed. (F) Close-up view of the ring-on-ring fixture on the universal testing machine.

4.1. Spark Plasma Sintering of ZrB$_2$-30wt%SiB$_6$ Ceramic Composite

Spark Plasma Sintering technique (FCT HDP 25; FCT Systeme GmbH, Rauenstein, Germany) was used to sinter a ball milled ZrB$_2$ (Grade B, H. C. Starck, Goslar, Germany) and SiB$_6$ (98% pure, -200 mesh, Cerac Inc., USA) ceramic powders. The graphite die of 20mm in diameter was packed with the ZrB$_2$-30wt%SiB$_6$ mixed powder and heat up to the sintering temperature of 1750°C and the dwell time of 10 minutes. The heating rate of 185°C/min was

58

used to heat up the die to the sintering temperature. After dwell time the machine was switched

off and natural cooling was initiated. The temperature, pressure and shrinkage plots collected

during SPS of ZrB_2-30wt%SiB_6 ceramic composite is shown in Figure 31. As one can see, the

sintering temperature was 1750°C with the dwell time of 10 minutes followed by rapid cooling

all the way until the die was cooled down to 400°C. From the sintering plot it can be observed

when heating was first initiated, but before the pressure was applied, the powder packed in the

graphite die expanded resulting in the appearance of positive shrinkage (Zone A in Figure 31).

When pressure was applied from zero to 50MPa the powder was compacted and the significant

negative shrinkage appeared (Zone B in Figure 31). However, this shrinkage was caused only by

the applied pressure, as the temperature was still too low (919°C-1129°C) to cause the sintering

of the ceramics, therefore, when the 50 MPa pressure was fully applied and remained constant,

the further increase on the temperature upon heating caused almost no visible shrinkage in

between 1129°C-1352°C temperature (Zone C-D in Figure 31) range, but upon further heating

the shrinkage, because of sintering of the powder, was initiated. The most active shrinkage of the

composite occurred in between 1352°C-1750°C (Zone C-D in Figure 31) and during the first

minute of the dwell time (Zone E in Figure 31). By the end of the dwell time, the shrinkage

ended and no further densification could occur (Zone E in Figure 31). Upon cooling, the

shrinkage occurred due to thermal contraction as temperature decreased (Zone F in Figure 31),

however when pressure decreased in Zone G of the plot, the material expanded causing the

shrinkage to increase one more time, until it all naturally cooled down with the material

shrinking without any applied pressure (Zone H in Figure 31). After sintering, 4.19 g/cm^3 density

of ZrB_2-30wt%SiB_6 ceramic composite disks was obtained. These ceramic disks were then

machined to the diameter of 18 mm and the thickness of 1.7 mm and one of the sides of the machined disks was polished to the mirror surface.
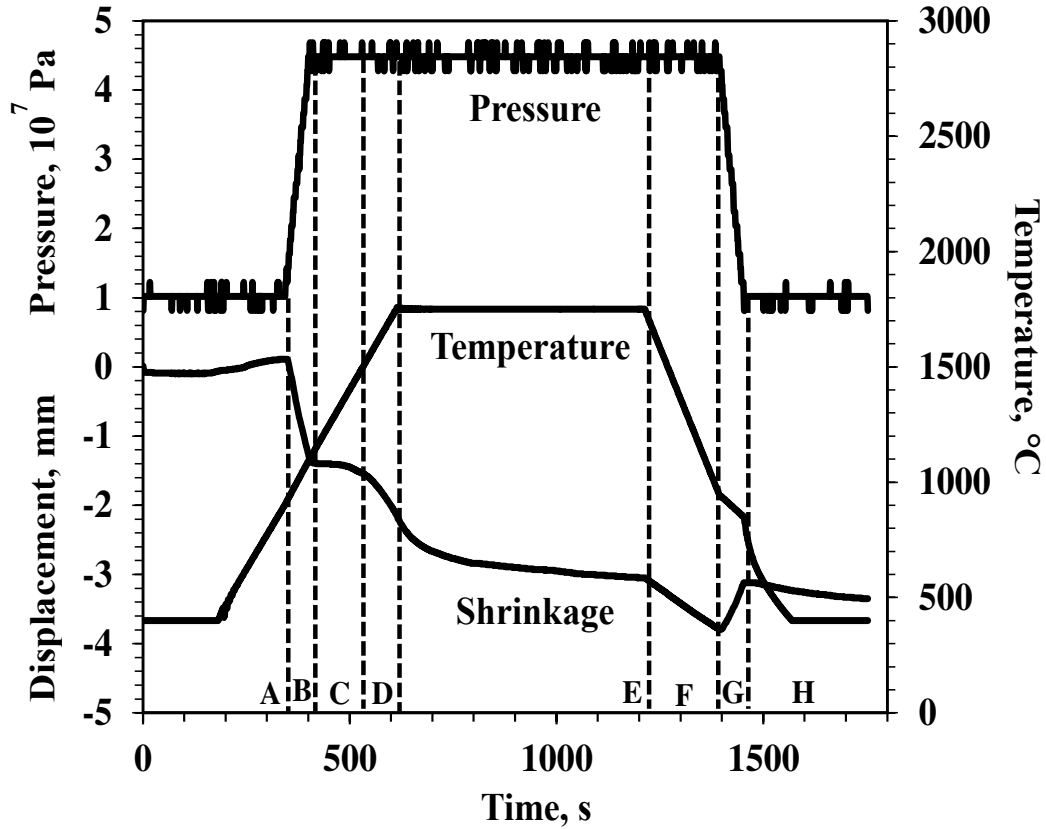
Figure 31: The pressure, temperature, and shrinkage plot showing the sintering parameters of ZrB$_2$-30wt%SiB$_6$ ceramic composite by SPS.

4.2. Phase Composition and Microstructure of ZrB$_2$-30wt%SiB$_6$ Ceramic Composite

The X-ray diffraction patterns (Rigaku Miniflex 600 diffractometer, Rigaku, Tokyo, Japan) of ZrB$_2$ and SiB$_6$ powders used for processing of the composite and ZrB$_2$-30wt%SiB$_6$ ceramic composite bulk material after SPS are shown in Figure 34. Pure single phase diffraction patterns were identified for ZrB$_2$ and SiB$_6$ powders. However, while ZrB$_2$ was retained after SPS as a major phase of the composite, the SiB$_6$ phase appeared not to be stable, as the peaks clearly belonging to SiB$_6$ structure [100] were not identified by X-ray diffraction. The Si and B phases were tentatively found instead, indicating the disruption of SiB$_6$ into two pure compounds. Also,

$Si_{11}B_{31}$ phase was also tentatively identified as an existing Si-B compound in the composite. A few weak X-ray peaks were tentatively assigned to two Zr-H hydrite phases, such as $ZrH_{1.6}$ and $ZrH_{1.9}$. Thus, the X-ray analysis identified that SiB_6 phase is not a stable phase upon sintering by current assisted SPS technique and a separate study would be required to determine the phase composition of the ZrB_6-SiB_6 ceramic composite after sintering using SPS. However, the composite was still used as a model material to verify the performance of the developed ring-on-ring fixture.

The microstructure and grain size of ZrB_2-30wt%SiB_6 ceramic composite was analyzed using a Zeiss Axio Lab.A1 (Carl Zeiss AG, Oberkochen, Germany) microscope. The optical micrographs of the ZrB_2-30wt%SiB_6 ceramic composite are shown in Figure 33. As one can see from the optical micrographs of the ZrB_2-30wt%SiB_6 microstructure, while in some areas the distribution of the two phases is relatively homogeneous, in many other locations large agglomerations of Si/B phase could be seen. The grain size analysis using intersection method allowed estimating that the average grain size of ZrB_2 phase was 2.25μm, while the average grain size of Si/B was 1.90μm. The grain size distributions of the phases along with their d_{10}, d_{50}, and d_{90} values are shown in Figure 33. Thus, as one can see from the micrographs and from the grain size analysis the structure is non-homogeneous, which would affect the mechanical performance of this composite.
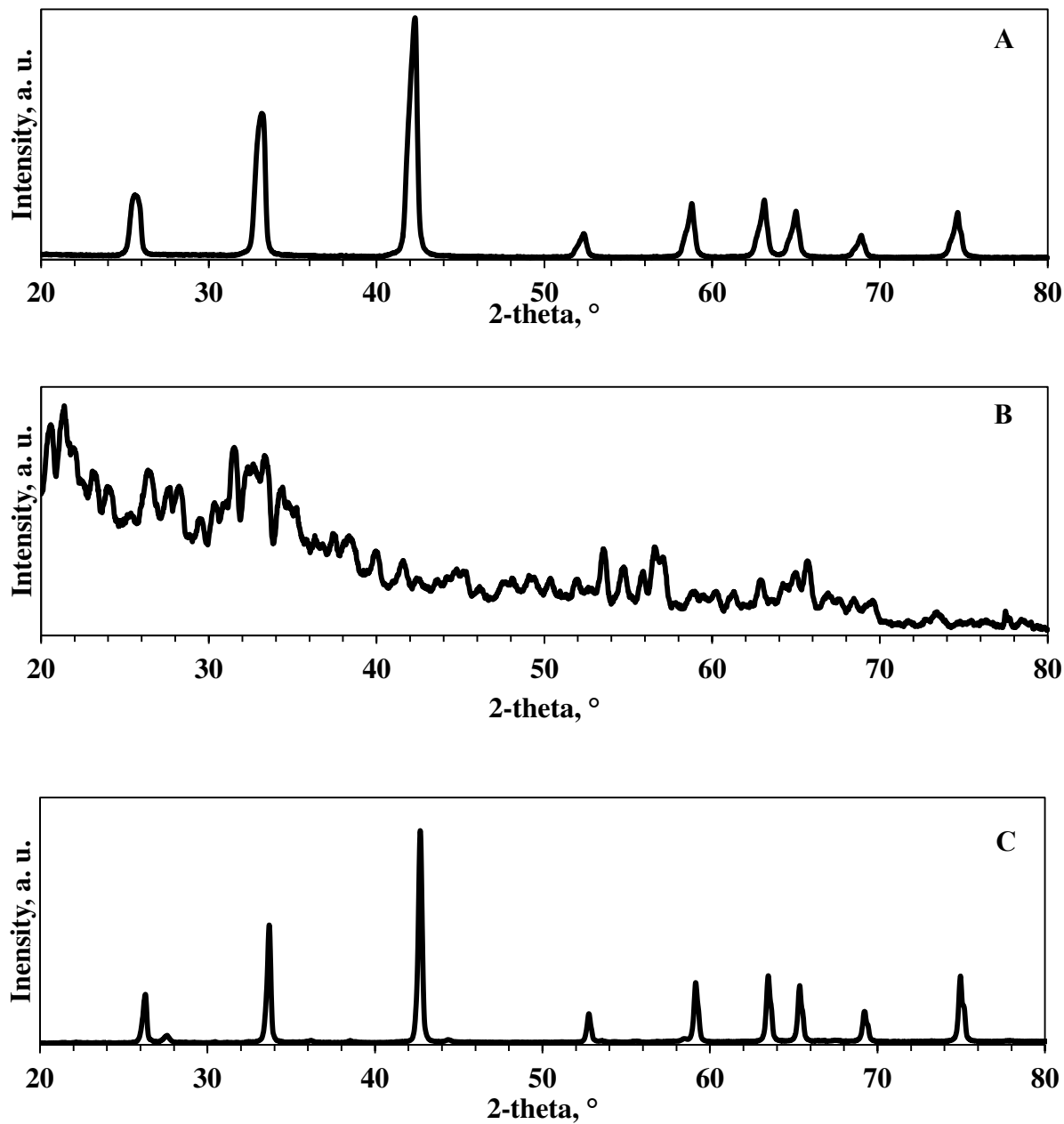
Figure 32: X-ray diffraction patterns of (A) ZrB₂ powder, (B) SiB₆ powder, and (C) ZrB₂-30wt%SiB₆ ceramic composite.
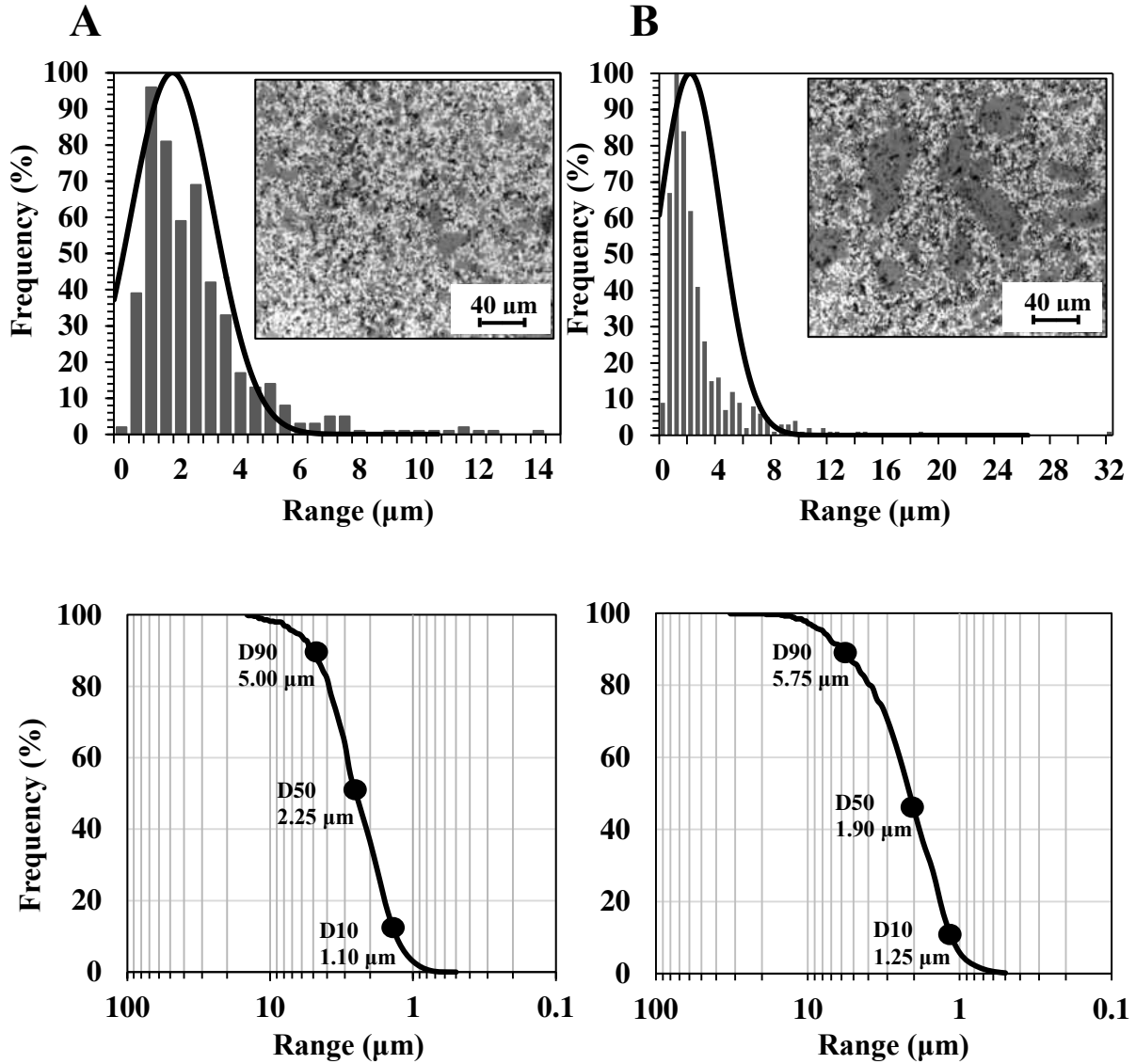
Figure 33: The grain size distribution of (A) ZrB$_2$ primary phase and (B) Si/B secondary phase with two optical micrographs of the microstructure of the composite showed as inserts.

4.3. Elastic Properties of ZrB$_2$-30wt%SiB$_6$ by RUS

The elastic properties of ZrB$_2$-30wt%SiB$_6$ ceramic composite were measured by Resonant Ultrasound Spectroscopy (RUS) (RUSpec, Magnaflux Quasar Systems, Alburquerque, New Mexico) both at room and high temperatures in an Ar protective environment, where the Young's, shear, and bulk moduli along with the Poisson's ratio are shown in Figure 34. The

63

Young's modulus at room temperature was equal to 452 GPa, and shear and bulk moduli were equal to 199 GPa and 210 GPa, respectively. The Poisson's ratio was equal to 0.136 at room temperature [Error! Bookmark not defined.]. There is almost linear degradation of the elastic moduli with temperature increase where Young's, shear and bulk moduli values are reported to be equal to 418.52 GPa, 183.83 GPa, and 192.87 GPa at 1000°C, respectively.
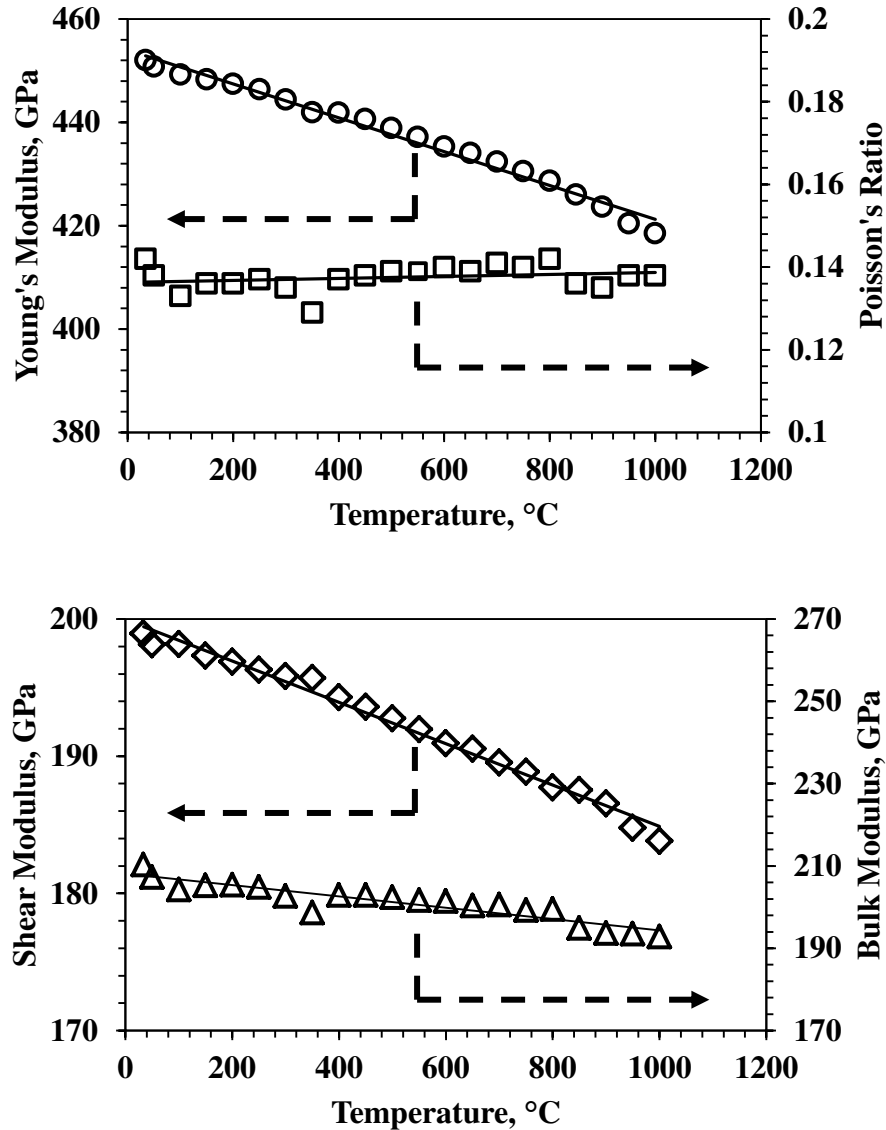
Figure 34: Elastic Properties for ZrB$_2$-30wt%SiB$_6$ measured by RUS. Young's modulus (○), Poisson's ratio (□), shear (◊) and bulk (△) moduli of ZrB$_2$-30wt%SiB$_6$ ceramic composite shown as a function of temperature.

4.4.Biaxial Strength through Ring-On-Ring for the Model Material ZrB$_2$-30wt%SiB$_6$

Three ZrB$_2$-30wt%SiB$_6$ disks were loaded up to failure using the developed ring-on-ring jig. The collected load versus time plot were used to generate the biaxial stress versus time plot shown in Figure 35 where the load was converted into stress using Equation (12). The biaxial strength measured at room temperature for three samples tested was equal to 225.31 MPa, 257.90 MPa, and 329.85 MPa, for samples 1, 2 and 3 respectively, which is rather below of the reported uniaxial bending strength of ZrB$_2$ based ceramic composites, such as 674 ± 130 MPa of 4-point bending strength of ZrB$_2$-SiC [89] measured at room temperature or 564.72 ± 11.21 MPa of 3-point bending strength of ZrB$_2$-15vol%SiC-15vol%MoSi$_2$ [101]. While it is not possible to directly correlate the biaxial strength with the strength values obtained by 4- or 3-point bending techniques, it is still understood that the biaxial strength of ZrB$_2$-30wt%SiB$_6$ ceramic composite is rather low likely because of the decomposition of SiB$_6$ into different phases during sintering. It is expected that ZrB$_2$-30wt%SiB$_6$ ceramic composites exhibit only elastic behaviour at room temperature, similar to other ZrB$_2$ based ceramics, as there are not known mechanisms available to introduce the non-linear deformation to the sample tested. Therefore, the generalized Hooke's law was applicable for the recalculation of the ε_x and ε_y strains related to the σ_x and σ_y applied stresses as Young's modulus and Poisson's ratio of the composite was measured by resonant ultrasound spectroscopy. The estimated stress-strain deformation plots of ZrB$_2$-30wt%SiB$_6$ ceramic composite is also presented in Figure 35.
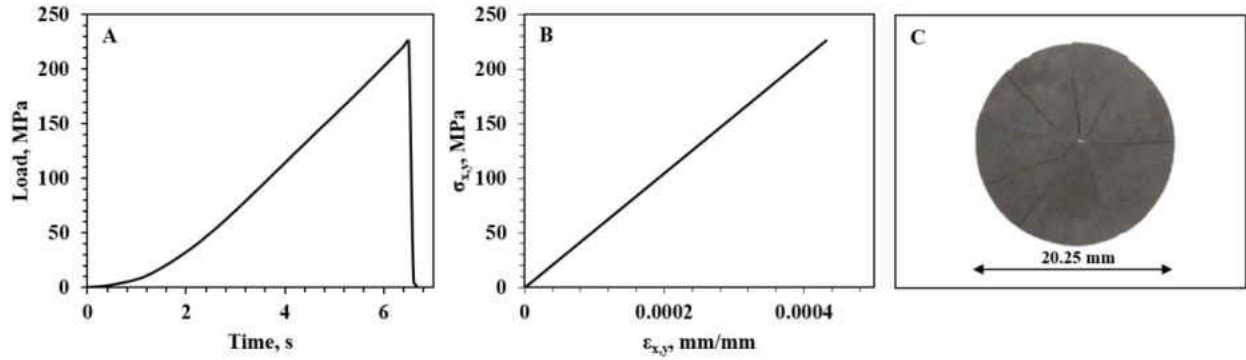
Figure 35: Biaxial stress-time plot (A), stress-strain deformation plot (B) and photograph of fractured sample (C) of ZrB2-30wt%SiB$_6$ ceramic composite disk.

4.5. <u>Finite Element Analysis for the Ring-On-Ring Test Using the Model Material Of ZrB$_2$-30wt%SiB$_6$</u>

A finite element analysis was performed for the ZrB$_2$-30wt%SiB$_6$ samples. It is known that Equation (12) was derived based on linear plate bending theory and the strength calculated is subjected to errors when non-linear geometry effect is significant. The purpose of this analysis was to assess the effect of geometric non-linear deformation in the calculation of strength as well as to validate the results from theory. The finite element software used was Simulia Abaqus® 6.19 (Dassault Systèmes, Vélizy-Villacoublay, France). The simulation was run using units of kilograms (kg), millimetres (mm), seconds (s). All interacting parts in the simulation were created in Abaqus® and selected as deformable bodies. Considering the symmetry of the geometry, material properties and loading, a 2D axisymmetric model was created and analysed, thus, a finer mesh control was achieved and more accurate data was observed with minimum computational cost and time. The load- and support-ring were defined as homogeneous elastic using the properties of 4140 steel, while the sample was defined as isotropic linear elastic using the properties obtained experimentally by resonant ultrasound spectroscopy, performed by the undergraduate student Jessica Dieguez from UCF with the help of Dr. Miladin Radovic from

66

Texas A&M, for the ZrB_2-30wt%SiB_6 samples. The density used for the 4140 steel and the ZrB_2-30wt%SiB_6 samples were 7.85 (10^{-6}) kg/mm^3 and 4.194 (10^{-6}) kg/mm^3, respectively, while the elastic modulus and the Poisson's ratio of 4140 steel and the ZrB_2-30wt%SiB_6 ceramic composite were 200 GPa, 452 GPa, 0.290, and 0.136, respectively. The contacts between the load-ring and the sample and the support-ring and the sample were defined as surface-to-surface contacts. Taking into consideration that simulations have been made using frictionless contacts [64] because the coefficient of friction in ring-on-ring is very small [49], three runs were made with the same model containing different values for the coefficient of friction, varying from frictionless to 0.1. A static, general step was defined for the simulation with duration of 6 seconds with initial step of 1 s, minimum of 1.00 (10^{-5}) s, and maximum of 6 s. To simulate the behavior of the interacting elements of the ring-on-ring, the support-ring was fixed in its position by avoiding any displacement or rotation whatsoever; for the load-ring, only y-axis displacement was allowed. From the experimental data, the force measured right before the sample broke, 654.82 N, was used to calculate uniform pressure over the load-ring top surface area. A pressure of 12.13 N/mm^2 resulted and was applied. For the load- and support-ring, a regular mesh with size of 0.1 mm was used, while the sample was meshed with a size of 0.04 mm uniformly over the section, yielding 8155 elements in total for the ceramic disk section. For the load- and support-ring 4-node bilinear axisymmetric quadrilateral, reduced integration, hourglass controlled (CAX4R) were used, and for the sample, 8-node biquadratic axisymmetric quadrilateral (CAX8R) elements were used. From the simulation, it was determined that the maximum tensile biaxial stress occurs inside the load-ring, on the bottom of the disk, indicated by red area in Figure 36, with a value of 224.3 MPa, 227.3 MPa, and 230.3 MPa, for the runs with coefficient of friction equal to 0.1, 0.05, and frictionless, respectively, which are close to the

experimentally measured value of 225.31 MPa. The closest value was obtained with the run involving the coefficient of friction of 0.1, which yielded an error of 0.4482%. Figure 37 shows how the radial, σ_r, and tangential, σ_t, stresses on the tensile surface vary as a function of the radial distance for the simulation with coefficient of friction of 0.1. σ_r and σ_t are equal at the centre of the tensile surface of the disk sample in the region enclosed by the load ring represented by the area marked by *A-B* in Figure 37. Vepakomma et al. [45] and Hsueh et al. [64] show that in a ring-on-ring simulation, the variation of maximum principal stress along the radial direction of the tensile surface shows a peak that occurs in the region enclosed by the load ring indicating that the stress is no longer uniform. The same behaviour was found in the simulation developed in this paper where, in Figure 37, σ_r is larger than σ_t for a small region, peaking in the line marked by *C*, and decreasing rapidly as the radial length distances from the centre of the disk. The line marked by *D* in Figure 37 shows the inflection point of σ_t and how it decreases in intensity, not as rapidly as σ_r, when it is measured in distances further from the centre of the sample. The inflection of the curve for the distribution of σ_t aforementioned occurs in a radial distance right below the contact point between the load ring and the sample. The line marked by *E* in Figure 37 shows an outlier point that describes an abrupt drop in the stress distribution on the tensile surface of the sample. This drop is caused by compressive stresses that arise from the contact point between the support-ring and the sample, and it does not represent a critical condition since its value indicates this is not a failure point in the ring-on-ring test.
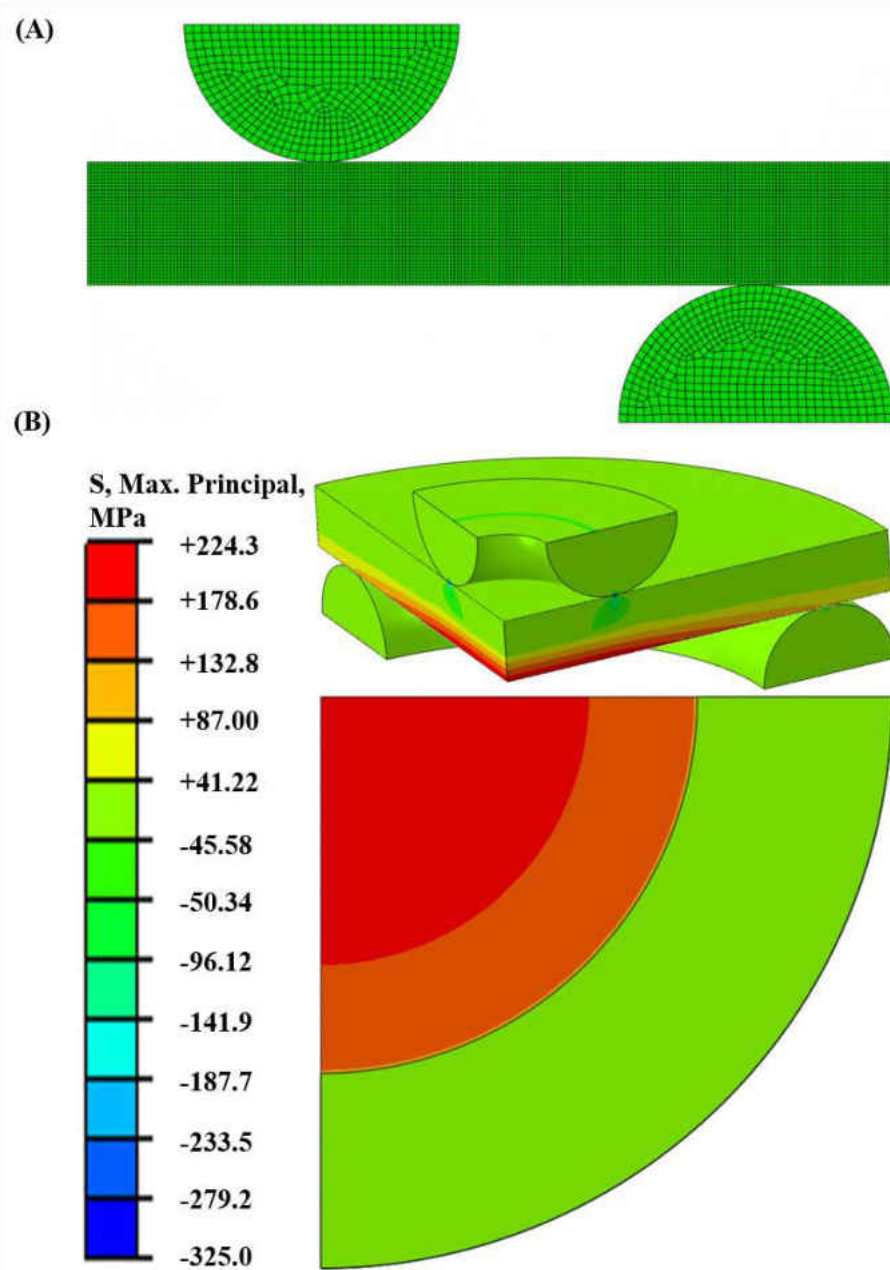
Figure 36: Finite element model of the ring-on-ring test using the sample material of ZrB$_2$-30wt%SiB$_6$ indicating (A) mesh distribution and (B) maximum-principal stress distribution on the sample.
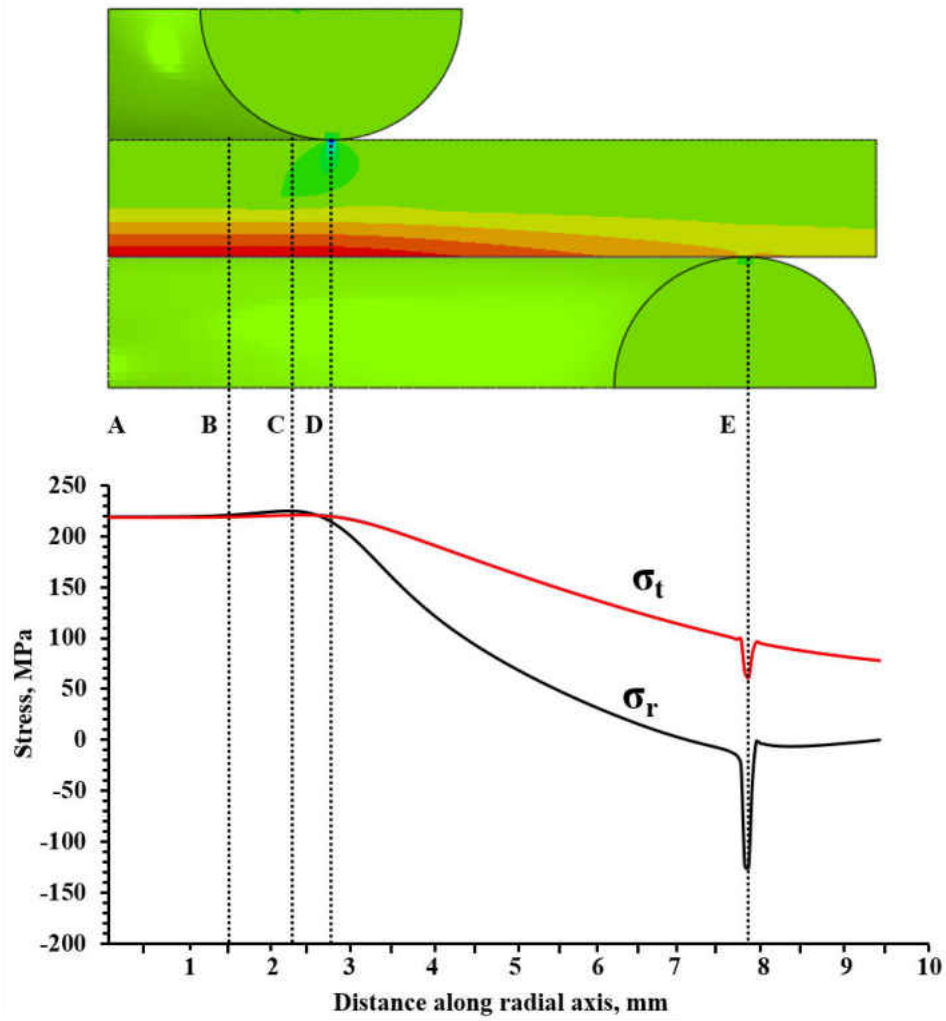
Figure 37: Tangential (σ_t) and radial (σ_r) stress distribution at the bottom tensile surface of the sample disk, shown in the upper portion of the figure, from the center to the edge of the disk, with coefficient of friction 0.1 and pressure of 12.13 N/mm².

5. *ACROPORA CERVICORNIS* STAGHORN CORAL SKELETON COMPRESSION STRENGTH AND VICKERS HARDNESS

Coral skeleton comprise the mayor inorganic structure found in a coral reef and, for the case of the critically endangered staghorn coral *Acropora cervicornis*, the skeleton is made by a $CaCO_3$ aragonite structure [79] and it allows the coral to withstand the high forces caused by the crashing of waves in shallow areas or the oceanic currents.

For the experiments performed in this research, one skeleton of dead *Acropora cervicornis* retrieved from Nova Southeastern University's coral nursery off Broward County, FL, USA, was studied (Figure 38A). Algae and other debris were chemically removed by immersion in bleach, which is a standard method for preparing coral skeletons. The skeleton was cut using a diamond blade into 4 cylinders with a 2.25:1 to 3:1 height and diameter ratios, with dimensions approximate due to the irregular skeleton geometry. Skeleton cross-sections were ground and polished using P1000-P3000 SiC sand paper to achieve a mirror surface suitable for hardness measurements. Optical micrographs of cross-sectional surfaces were made using a Zeiss Axio Lab.A1 microscope (Carl Zeiss AG, Jena, Germany) and photographs of full cross-sectional surfaces were made using a Canon SX530 digital camera (Canon Inc., Tokyo, Japan). An *A. cervicornis* was analyzed by X-ray computed tomography at 9 mm voxel size (GE Phoenix Nanotom-M™, GE Sensing & Inspection Technologies GmbH, Hamburg, Germany). X-ray emission parameters were 90 kV and 140 μA and 1801 images were collected through a 360° rotation. Each positional 2D X-ray projection was collected as an average of 3 images. The 3D volume was produced by reconstruction with Phoenix datos software. The 3D rendered volume was analyzed and images/animations produced utilizing VG Studio Max software (v2.1) (Volume Graphics GmbH, Heidelberg, Germany).

Both top and bottom surfaces of the cylindrical skeletal samples were ground flat and parallel to obtain surfaces ready for uniaxial compression tests. Uniaxial compression tests were performed using a universal testing machine (Criterion® 43, MTS, Minnesota, USA) in displacement control mode using a 0.003 mm/s displacement rate. A Vickers hardness tester (Tukon 2100B, Wilson Instruments, Illinois, USA) was used to measure hardness with ten indentations made using a 50 g load with 15 s dwell time under load. Raman spectroscopy of the skeleton was collected using a Renishaw® inVia Raman microscope (Renishaw, Gloucestershire, the UK). The microscope system used for the Raman spectra collection consists of a 532 nm Si solid laser with maximum power of 300 mW, a spectrograph with holographic notch filter attached to a Leica microscope (Leica Microsystems, Wetzlar, Germany) with a motorized XYZ-stage. The system was used to collect a 2D map of the surface of the sample with an area of 9.75 μm by 15.75 μm where 308 acquisition points at the step of 0.75 μm were obtained with a collection time of 10 s per point using an objective lens of 100x with working distance of 4.7 mm, which permitted to have a laser spot of approximately 1 μm. The map was carried at room temperature, and before its collection, the spectrometer was calibrated using a Si band at 520.3 cm^{-1}. Autofocus was used for the collection of the map since it provides better focused results during the area mapping. To produce the maps, Renishaw WiRE® software was used with mixed Gaussian and Lorentzian function for peak fitting. The system was set to collect the map over half of a Vickers indentation on the bleached *Acropora cervicronis* sample surface with a total collection time of 1.25 h.

The skeleton structure of *Acropora cervicornis* is very complex [89,102,103,104] and consists of needle-like aragonite crystals organized as the primary skeletal elements. The skeleton structure is highly porous but porosity and thus, permeability, decreases from the tip of the coral

towards its base. Cross-sections of the skeleton of *Acropora cervicornis* showed a highly symmetric structure and the higher-magnification optical micrograph revealed significant surface porosity (Figure 38B). From the computed tomography (CT) scan the pores within the body of the coral skeleton can be observed in more detail (Figure 39). Pores varied in size and shape, with major circle-like cavities presenting an average size of approximately 1 mm in diameter. Major and minor cavities were non-homogenously distributed along the coral.
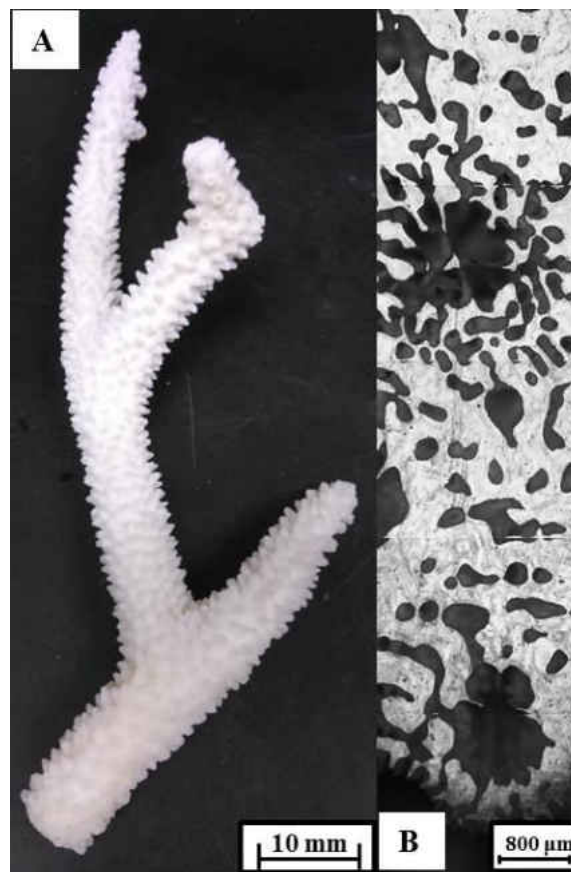
Figure 38: (A) Chemically-cleaned, dry skeleton of the critically-endangered coral,
***Acropora cervicornis* from Nova Southeastern University's coral nursery, Broward County,**
USA. (B) Representative optical micrograph of the dense part of its skeleton.
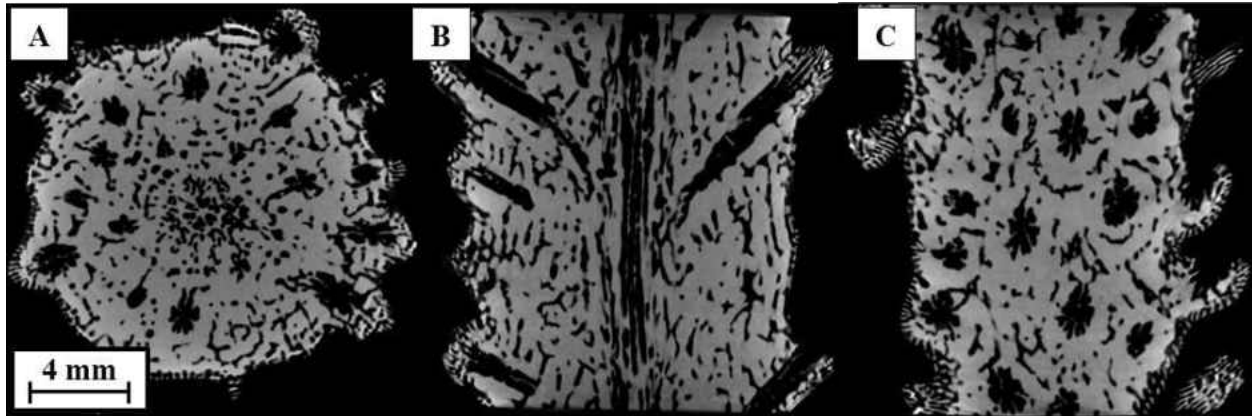
Figure 39: Computed tomography scan of the skeleton of the critically endangered coral, *Acropora cervicornis***, showing (A) cross-sectional top view; (B) longitudinal section parallel to the height of the sample at 0 mm from the center of the sample; (C) longitudinal section located 4 mm from the center of the sample.**

Figure 39A shows the top cross-section view of the corallite with the axial canal shown in the center of the cross-section. Also, as one can see from Figure 39A, both radial and circumaxial cavities are distributed along the cross-section. Figure 39B shows the axial canal of the corals along the center of the cross-section with both radial and circumaxial cavities caused by bioerosion [105]. Such erosion is responsible for removal of calcium carbonate by biological conditions. Figure 39C shows the radial corallites – the skeletal cup formed by an individual stony coral polyp in which the polyp sit and retract. The space between the radial corallites is 2-3 mm with their diameter being between 0.8-1 mm. These corallites are separated with the coenotsteum - the layer of living material lying between the corallites (Lamarck, 1816). The classification and detailed description of *Acropora cervicornis* coral skeleton microstructure was published by Marfenin [106] which are the same as found in the corals analyzed in this research.

5.1. Uniaxial Compressive Strength of *Acropora cervicornis*

The stress-strain plot of the coral skeleton under uniaxial compression exhibited non-linear loading with many step-ins (Figure 40), until at higher loads the sample completely

fractured. This response is indicative of a "gracious" failure, which apparently occurred due to the complex microstructure of the coral skeleton: cracks originated during loading had to deviate, branch and bifurcate to grow and move further as compressive loading increased. The major crack in the fractured skeleton (Figure 40A) grown parallel to the applied load. This is characteristic of compressive fracture in brittle materials such as ceramics and rocks [107,108]. Under uniaxial compression cracks grow parallel to the loading axis. The presence of sharp pores of different shape and size facilitates the initiation of fracture at several locations and with increase in load these cracks grow longer. However, when a crack reaches a nearby larger pore in its path, it stops to grow because the stress concentration accompanying the crack tip quickly reduces. The stress has to further increase substantially before the crack starts to grow again. This process of rapid crack growth and arrest results in sudden load drop in the stress-strain curve and then an increase with continued loading. After few cracks have grown sufficiently long, failure of the specimen into many fragments occurs.
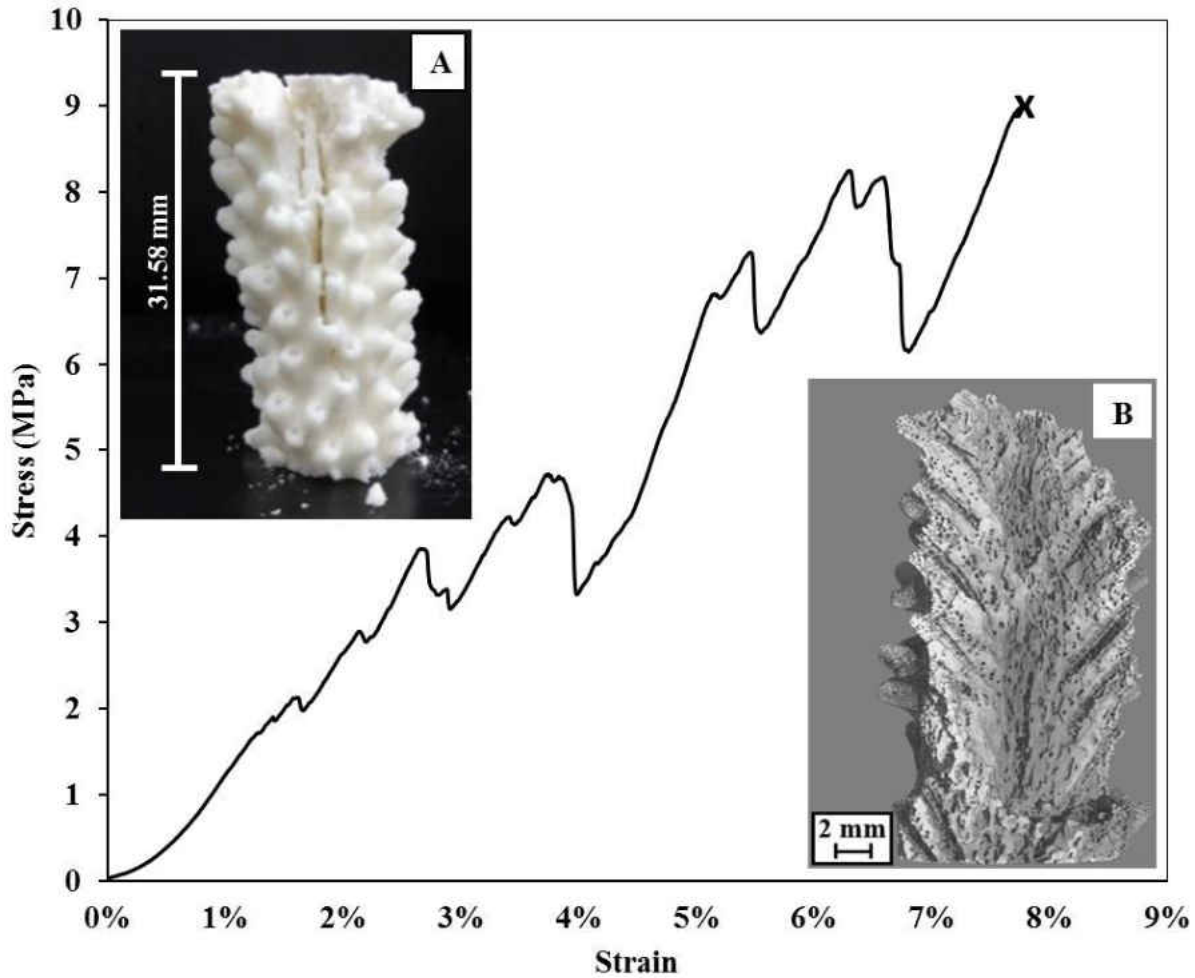
Figure 40: Stress vs. strain deformation plot of the critically endangered staghorn coral, *Acropora cervicornis*, **measured in uniaxial compression. Insert A is the photograph of the sample after fracture. Insert B is the CT scan of the fracture surface along the axial direction of the sample.**

The presence of numerous pores in the specimen not only retards the crack growth but also allows partial cracks to develop without causing complete fracture of the specimen as shown in Figure 40A. The intermittent crack growth in the presence of pores not only prevents catastrophic fracture typical of brittle materials, allowing for the "gracious" failure to occur. Finally, at peak load, many such intermittent crack growth events occur resulting in a saw-tooth stress-strain curve before complete load drop upon specimen failure.

76

The fracture surface of the coral skeleton shown in Figure 40B presents features of typical brittle failure of a porous ceramic structure [28,109]. Thus, it is obvious that the coral skeleton's ability to resist cracking is important for its existence because it does not separate easily from its parent structure even after small cracks develop.

5.2. Vickers Hardness of *Acropora cervicornis*

The Vickers hardness of a chemically-cleaned skeleton measured at 13 different points of the sample's polished surface was 3.56 ± 0.31 GPa, which is similar to the 3.31 GPa reported by Alvarez et al. [110]. Such hardness values are very typical for soft $CaCO_3$ aragonite materials, yet are sufficient to withstand the hydraulic pressure caused by ocean wave impacts. Optical photographs of two Vickers impressions had almost no radial cracks originating from the corners of the impressions (Figure 41A).

This behavior is once again attributed to the presence of numerous pores which reduce the stress intensity at the tip of the indentation imprint. Both the indentation and compression response are indicative of the skeleton's complex microstructure and its ability to suppress crack propagation and growth. It is worth to notice that many of the impressions, such as the one shown in Figure 41B, developed the lateral cracks causing chipping and uplifting of the surfaces surrounding the impressions.
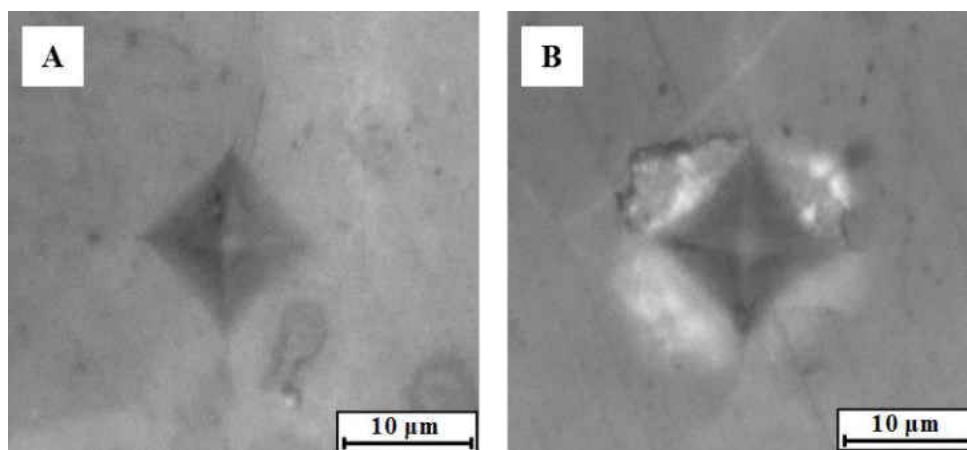
Figure 41: Optical micrographs of Vickers hardness impressions after 1 kg load in a chemically-cleaned skeleton of staghorn coral (*Acropora cervicornis*) reared in a nursery off Broward County, Florida, USA. (A) Indent with no chipping or lateral cracks; (B) indent with lateral cracks.

5.3. <u>Micro-Raman Spectroscopy of *Acropora cervicornis*</u>

Raman spectrum of *Acropora cervicornis* is shown in Figure 42A. As one can see from Figure 42A, the spectrum has 150 cm^{-1}, 203 cm^{-1}, 699 cm^{-1}, and 1083 cm^{-1} peaks, which are all characteristic of the aragonite structure [111,112]. It would be interesting to see how CaCO$_3$ aragonite structure is responsive to the stress and therefore, one of the Raman active bands, 1083 cm^{-1} with the strongest intensity was further selected to collect 2D Raman maps of the surface with the Vickers impression as such mapping allows to detect how the applied stress affects the vibrational response of the aragonite structure. The optical micrograph of the impression with the area selected for 2D Raman mapping and corresponding Raman micrographs of the 1083 cm^{-1} peak's intensity, peak's position and peak's FWHM are shown in Figure 42B. The contour of the Vickers impression can be clearly distinguished in all three maps. From the Raman maps, one can see that the peak intensity, peak position and FWHM are affected by the presence of the stresses introduced during the indentation event. The intensity of the peak is significantly decreased from 4500 – 5500 a. u. outside of the impression to 2000 – 2500 a. u. in the location of

78

the center of the impression where residual compressive stresses are the highest. The peak has significantly broaden from 4 cm^{-1} of FWHM outside of the impression to 7 cm^{-1} in the center of the impression, but the position of the peak changed non-significantly from 1083.1 cm^{-1} outside of the impression to 1083.7 cm^{-1} in the center indicating the weak stress dependence of this peak. These results indicate that aragonite structure is indeed responsive to the applied stress, especially to the concentrated load, which might occur to the coral skeletons in the ocean when the different objects, such as marine debris, can impact corals during storm or other detrimental events.
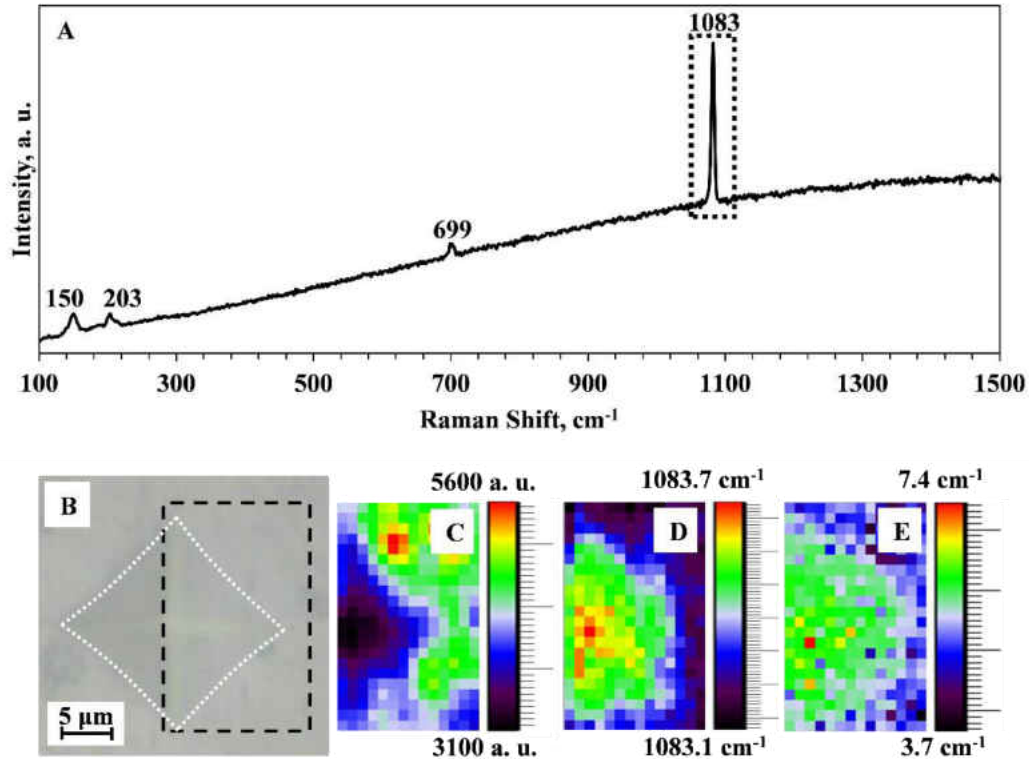
Figure 42: Raman spectrum of the skeleton of staghorn coral (*Acropora cervicornis*) showing the signature peak characteristic of an aragonite structure. (B) Optical micrograph and corresponding 2D maps of 1083 cm^{-1} Raman peak of (C) peak intensity, (D) peak position, and (E) peak width. The area of the mapping represented by the dashed line in (B) is 15.75 x 9.75 μm^2.

79

5.4. **Flow-Field of the Coral Skeleton**

The flow-field of the coral skeleton sample at different instants of the motion during fluidic experiments is presented in Figure 43. Figure 43A shows that after 1 s from the beginning of the motion, two counter-rotating vortices formed in the wake of the moving skeleton, still attached to it at that moment, which had yet to separate from the coral surface. These vortices resembled classical Kármán vortices that form in the wake of a bluff body[113]. As the shape of the coral skeleton was approximated by a circular cylinder with significant surface roughness, this roughness element created a number of smaller scale vortices, which were dragged into the wake. Figure 43B shows that the vortices formed earlier during the motion got disintegrated, and small-scale vortices appeared in the wake. The surface roughness of the coral skeleton likely promoted these small-scale instabilities in the wake, which quickly ruptured the bigger, Kármán type vortices. This trend continued at the later stages of motion (Figure 43C and D), where smaller-scale vortices prevailed.
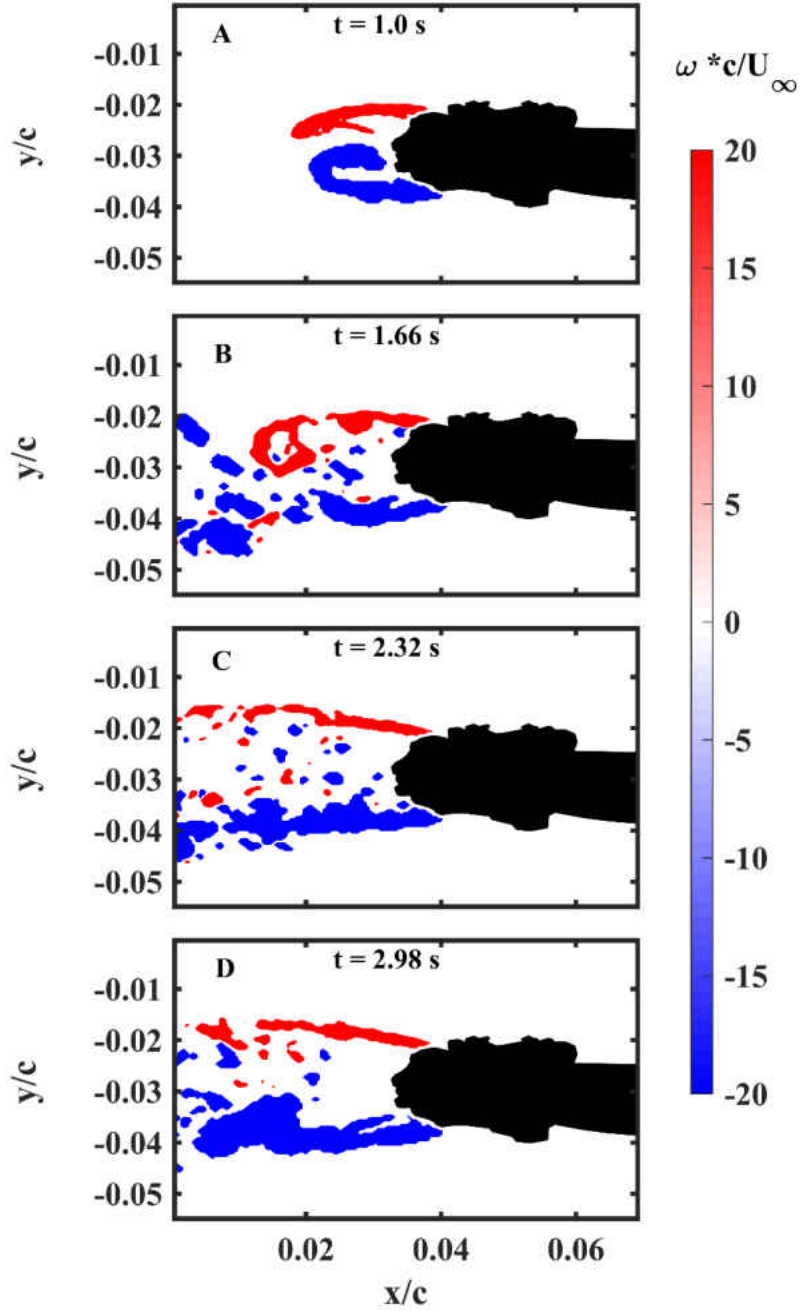
Figure 43: Contour plot of normalized vorticity (ω_c/U_∞) in the wake of the coral skeleton at different instants of the motion. c denotes the equivalent radius of the cross-section of the coral model, where PIV measurements were performed. The black portion denotes the masked-out part of the image to cover the shadow from the model. (A) After acceleration was completed, two counter-rotating vortices formed in the wake similar to a bluff-body wake, which were yet to be shed; (B) Smaller scale vortices started to form in the wake and the two main vortices started to disintegrate, which continued further as shown in (C) and (D).

81

6. RELATIONSHIP BETWEEN POROSITY AND THE ELASTIC MODULUS IN THE *ACROPORA CERVICORNIS* CORAL SKELETON

The ability of reproduction for the *Acropora cervicornis* coral is directly related to the health and strength of the skeleton that conform it. To populate an area, these types of corals depend on the hydrodynamic forces and currents that surround them since the coral requires for a branch to be detached from the main body, then it travels by a current to an empty space where it gets fixed to the bottom of the seafloor and starts the growing process that will repeat itself until a colony is formed [87,88]. Since this cycle is being interrupted by human activity which is contributing to the increase of seawater level, and water temperature and acidity, the contribution to the repopulation of this coral specie is being held through coral nurseries in many parts of the coasts of the Atlantic Ocean and Caribbean Sea through the use of controlled reproduction techniques by the breakage of healthy coral stems [16,85,90]. In order to achieve the reproduction process, either naturally or artificially, helped by human beings the understanding of the mechanical strength of the *Acropora cervicornis* coral skeleton and how the porosity affects it is of importance.

6.1. Microstructure Characterization and Porosity Measurement of the Coral Skeleton

Porosity varies in the coral skeleton depending on the conditions of the water where the coral grew and the age of the skeleton, thus varying form the stem of the coral branch to the tip [79]. It has been demonstrated that the rate of mineralization in a coral skeleton is affected by the water temperature and the rate of growth by the height of the water column covering the coral [90]. Many efforts have been made to study the properties of coral skeletons and its microstructure using techniques such as scanning electron microscopy [79], ultrasound pulse velocity tomography, compression and tensile tests, three-point bending and computational fluid

dynamics [90] which have given a better understanding of the coral skeleton and its interaction with the environment that surrounds it. A study conducted by Baldock et al. [90] found that for different branches of *Acropora cervocornis* skeletons studied the density was 2.42 g/cm^3, the porosity between 12-40%, the compressive strength was found to be 28-99 MPa, the tensile strength was measured as 8.84-12.7 MPa, and an elastic modulus of 55-77 GPa, all these being affected by a reduction in calcification due to the change of acidity in the waters the corals inhabit

To obtain a better understanding on the microstructure and porosity of the skeleton of the *Acropora cervicornis* coral reefs a 3D computer model of one section of the coral was produced from the CT scans generated using a GE Phoenix Nanotom-M™ (GE Sensing & Inspection Technologies GmbH, Hamburg, Germany). The emission parameters for the X-ray used were set to 90 kV and 140 µA and 1801 collecting images through a 360° rotation with an average collection of 3 images of 2D X-ray projection. An example of the images used can be found in Figure 39A. The video provided by the CT scan was split into 501 images extracted by the development of a code that processes images and videos using the open source language Python™ (Python Software Foundation, Delaware, USA) and the library OpenCV. The porosity was measured using optical techniques on the images that resulted from the CT scan and using the software imageJ (Public Domain, BSD-2 license) to apply a threshold that would make the images strictly black and white as seen on Figure 44. Two features were analyzed, the solid part of the coral captured by the CT scan (white area Figure 44A) and the holes and pores captured by the same instrument (white area Figure 44B) for all 501 images used. A Python™ code was developed to account for the number of white pixels on the images measuring porosity by finding the ratio between the solid skeleton, achieved by adding the area of the pores as in Figure

44B to the images that do not account for the pores, as in Figure 44A, and the skeleton with pores. The resultant porosity can be found in Figure 45.

(A)   **(B)**
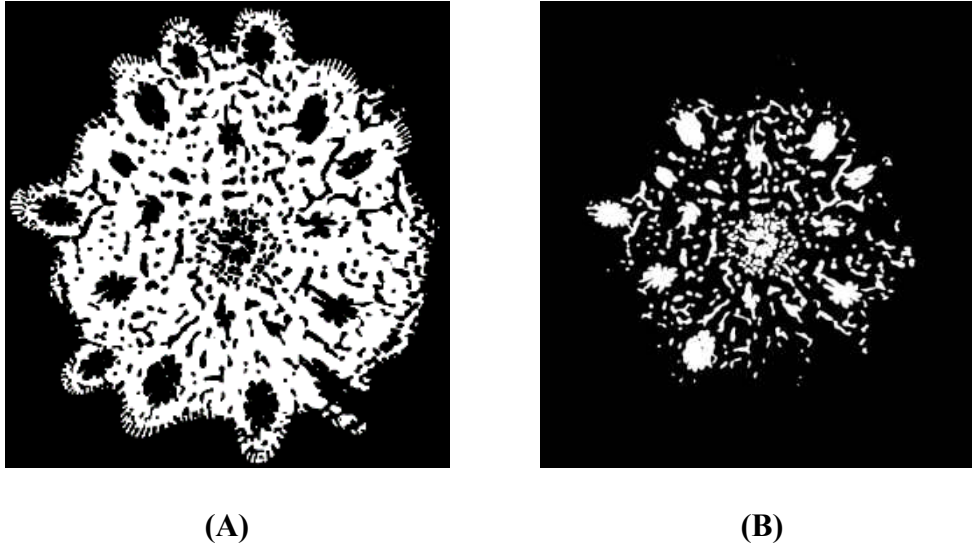
Figure 44: Threshold applied to the coral skeleton images to measure the porosity of the skeleton. (A) is the image accounting for the solid area and (B) is the image accounting for the area of the pores and holes.
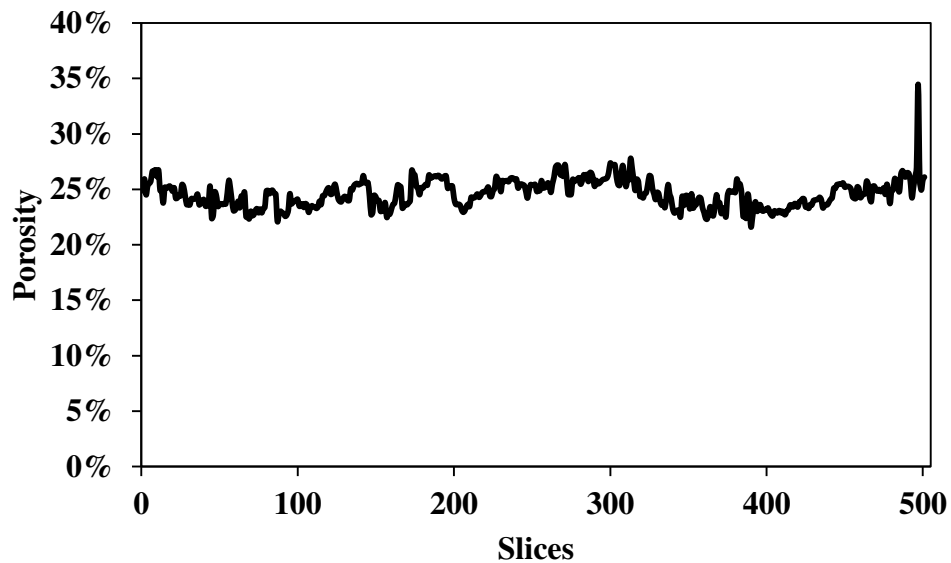
Figure 45: Measured porosity on the *Acropora cervicornis* coral skeleton on 500 slices extracted from the CT scan.

84

The average porosity with this technique was found to be around 25%, matching what has been previously reported in the literature [89,90].

An experimental method was also used to estimate the porosity of the coral skeleton and it consisted in measuring the open porosity through the ratio of the pore volume (V_0) to the total volume (V_t) of the skeleton by measuring the dry mass of the porous specimen (m_1), the mass of the specimen impregnated by the fluid when it is submerged (m_2), and the mass of the specimen suspended in the fluid (m_3) calculated as follows [114],

$$V_0 = \frac{m_2 - m_1}{\rho_f} \tag{29}$$

$$V_t = \frac{m_2 - m_3}{\rho_f} \tag{30}$$

where ρ_f is the density of the fluid, in this case water. By the use of this technique, the porosity was found to be 44.73%.

Since a difference in results existed between the porosity measured using optical-imaging technique and the results obtained through experimental methods a Scanning electron microscopy (SEM) was performed using a JEOL JSM-6480 SEM (JEOL Ltd., Tokyo, Japan) to measure the smallest features of the coral skeleton from which interesting observations were made. The SEM images can be found in Figure 46 where it can be observed how the skeleton is connected by branches that grow like a truss system perpendicular to the main cylinder that conform the structure of the coral making the skeleton more resistant to external stresses [79].

By looking at the distribution of the branches, a square open cell was assumed to be the one that most resembles the structure of the skeleton which yielded a porosity of 49.89% by

using the Gibson & Ashby (G&A) approach and assuming to be uniformly distributed among the

skeletal structure.
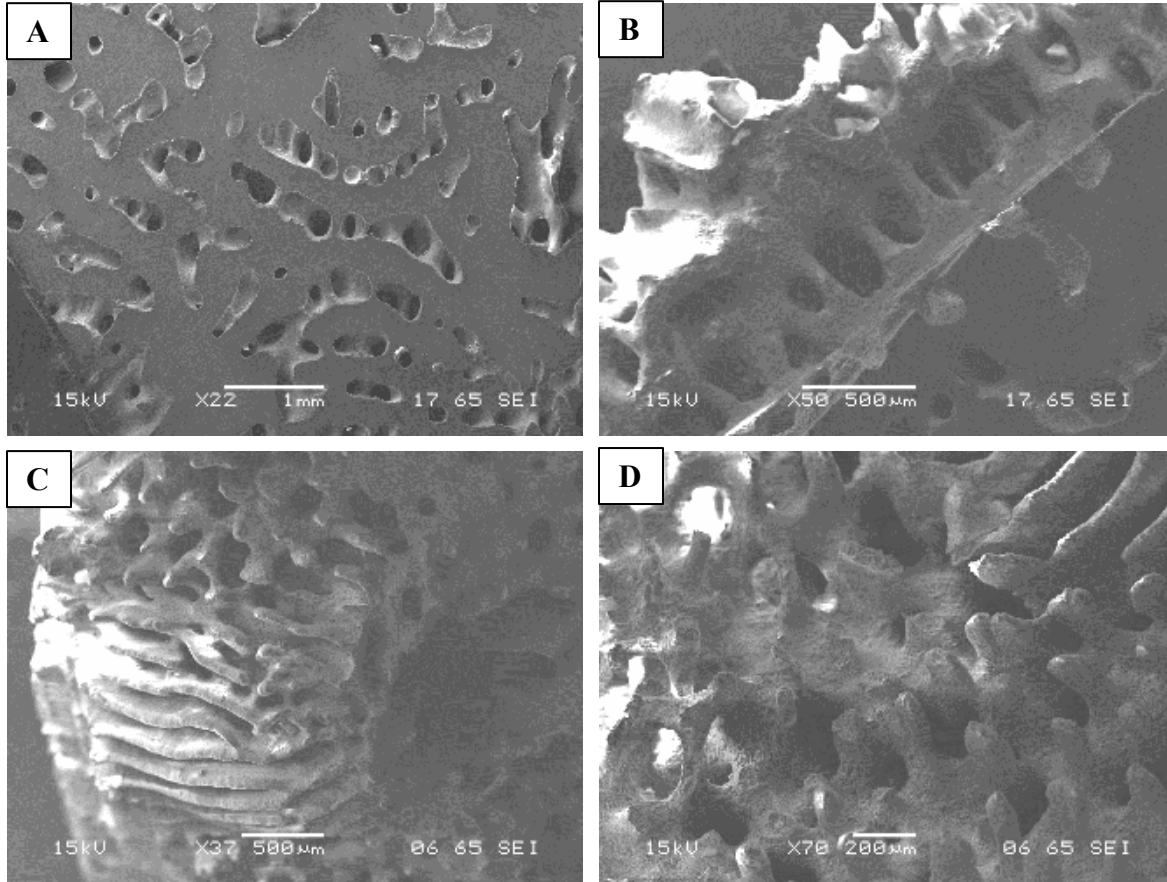
Figure 46: SEM images of the *Acropora cervicornis* coral skeleton showing the small pores covering the coral surface and the features that compose connect the skeleton together. (A) shows the pores inside the skeleton and from the holes the connecting links can be observed. (B) shows a picture from the edge of the cross-section of the coral skeleton and the links that act similar to a truss system can be observed. (C) shows a picture from the side of the coral skeleton and it can be observed that conducting channels constitute a big part of the structure. (D) shows the arrangement of the material in the coral surface when they do not define a channel and the appearance of stalagmites can be seen.

A summary of the porosity found using the different methods can be found in Table 3.

Table 3: Summary of the porosity obtained through three different measurement techniques.

Method	Porosity (%)
CT-Scan and image analysis	25%
Porosity through water impregnation	44.73%
SEM and G&A	49.89%

6.2. Analysis of the Elastic Modulus for the *Acropora cervicornis* Coral Skeleton

A 3D volume mesh of the coral skeleton was developed by using the CT-scan video and dividing it into frames from which the parameters set by the CT-scan were kept and a separation distance between images of 9 μm needed to build the 3D model was obtained. Once the images were sorted, the software Mimics® (Materialise NV, Leuven, Belgium) was used to stack the pictures and build a solid computer-aided model that was later used for the creation of a 3D solid model to be used for the simulation of the coral skeleton using the finite element method. Figure 47 shows an example on how the solid model was generated using the stack-up of images and the resultant solid generated by Mimics®.

CT Scan image **Stack-up of images** **3D model generated by Mimics®**
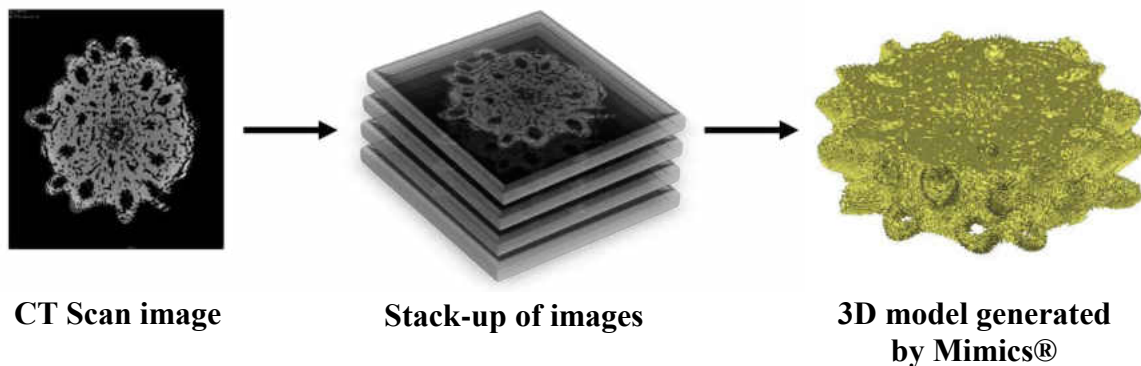
Figure 47: Steps involved in the generation of the 3D computer-aided model of the coral skeleton from the images provided by the CT scan video.

After the 3D model was generated in Mimics® it was required to develop a volume mesh for the further analysis of the skeleton using the finite element method. For this purpose, the solid model was exported to Materialise 3-matic® (Materialise NV, Leuven, Belgium) on which the complexity of the structure was reduced and the model was smoothed for the generation of a volume mesh that was used for the finite element simulation. The model was composed by 4-node linear tetrahedron elements and an example of it can be seen in Figure 48.

| (A) | (B) | (C) |
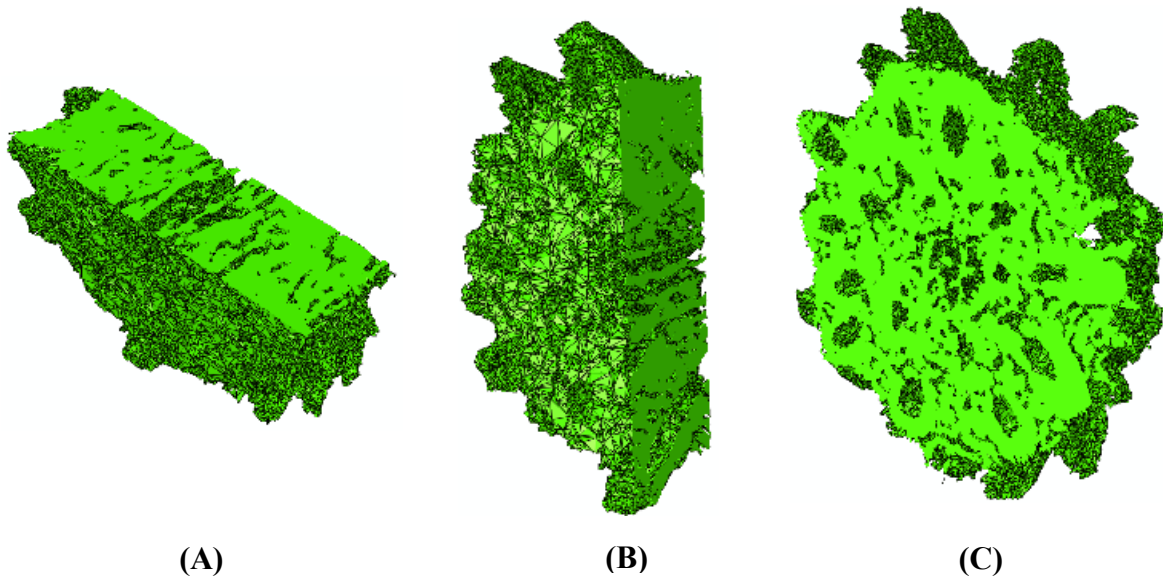
Figure 48: Volume mesh for the coral skeleton generated using 500 slices from the CT scan. (A) shows the cross-section of the ZX-plane of the skeleton and the porosity within the structure. (B) shows the cross-section of the XY-plane. (C) shows the cross-section of the YZ-plane.

As can be seen in Figure 48 the small pores of the skeleton disappeared due to the smoothing of the model and the geometry of the elements used. Only the major defects were kept in the volume mesh, such as the inner channels of the skeleton, after the simplification of the model which gave the model a total porosity of approximately 20%, not resembling the true porosity of the skeleton.

Once the volume mesh of the coral skeleton was developed it was exported into Abaqus/CAE 2017® (Dassault Systèmes, Vélizy-Villacoublay, France) as an Abaqus input file (.inp) which is a document generated by 3-matic® in which it assigns numerically the coordinates for the geometry of each element in the volume mesh. The simulation was set-up initially using the elastic mechanical properties of solid $CaCO_3$ since the structure of the skeleton is mainly formed by an aragonite structure [89]. The simulation was performed using linear geometry due to the fact that *Acropora cervicornis* coral skeleton can be assumed to be linearly elastic [90]. A combination of the experimental observations and the properties of $CaCO_3$ were used to define the parameters of the simulation. The material properties used were density $\rho = 2,930 \; g/cm^3$, elastic modulus of pure aragonite $E = 86,572 \; MPa$, and Poisson's ratio $v = 0.209$. The strain, with value $e = 1.2025\%$, was obtained from the experiment and was used to set the displacement of the model based on the number of slices used. The total running time for the simulation was $t = 73 \; s$ based on the experimental data and the a static step was defined with $1E6$ increments with initial time step at 1, a minimum of $1E-10$ and a maximum of 73. Since the 3D model of the skeleton was approximately 20% porous, the elastic modulus that resulted from it was high compared to the experimental and reported values, with a value of 74.221 GPa.

Another model was followed to obtain the elastic modulus of the coral skeleton by adjusting the modulus of the aragonite structure for different levels of porosity in the skeleton using the Gibson & Ashby approach [115]. These results were then validated by comparing the values obtained to the results found in the literature [90,5]. The Gibson & Ashby approach was adapted for a square open cell as can be seen in Figure 49, and the elastic modulus was estimated using the open porosity of 49.89% and the following equation,

$$E_p = C_1 E_m (1 - V_p)^2 \tag{31}$$

where E_p is the adjusted elastic modulus, C_1 is a constant proper from the geometry of the cell which is 1 for a square cell, V_p is the porous volume of the structure. The results for the adjusted modulus of the structure for the porosity found using the ratio between the pore and total volume on equations (29) and (30) and porosity ranging from 0-100% can be found in Figure 50 where they are compared to the values for the elastic modulus found in the literature.

(A)

(B)

cell edge

open cell face

CELL EDGE
BENDING
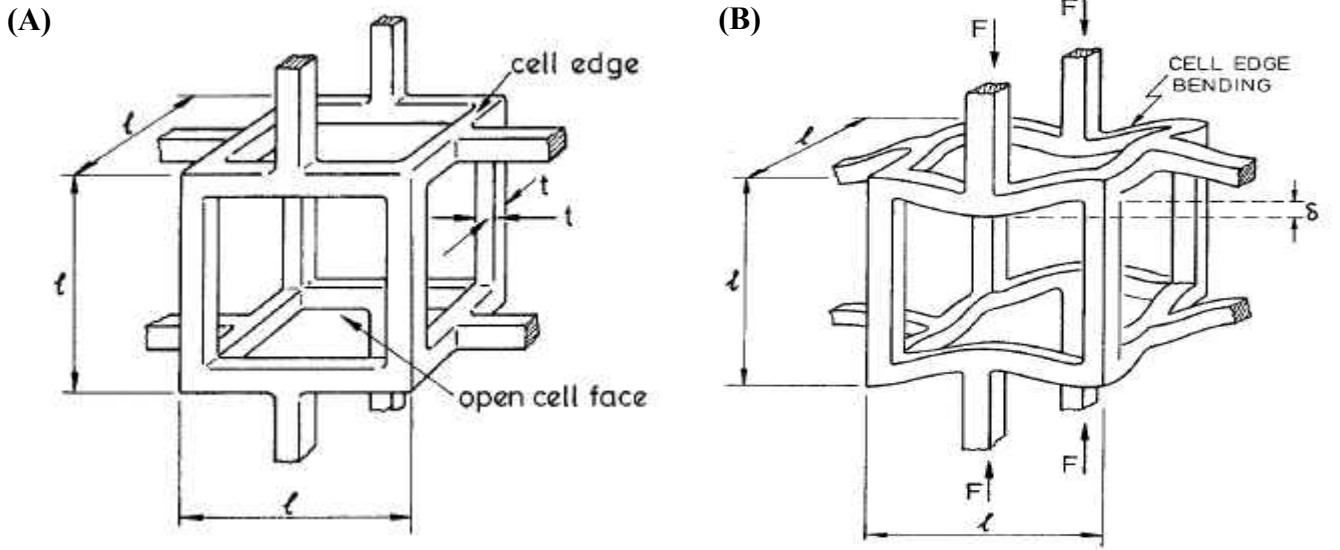
Figure 49: Square open cell as assumed by the Gibson & Ashby approach under no stress (A) and under bending due to compression (B).
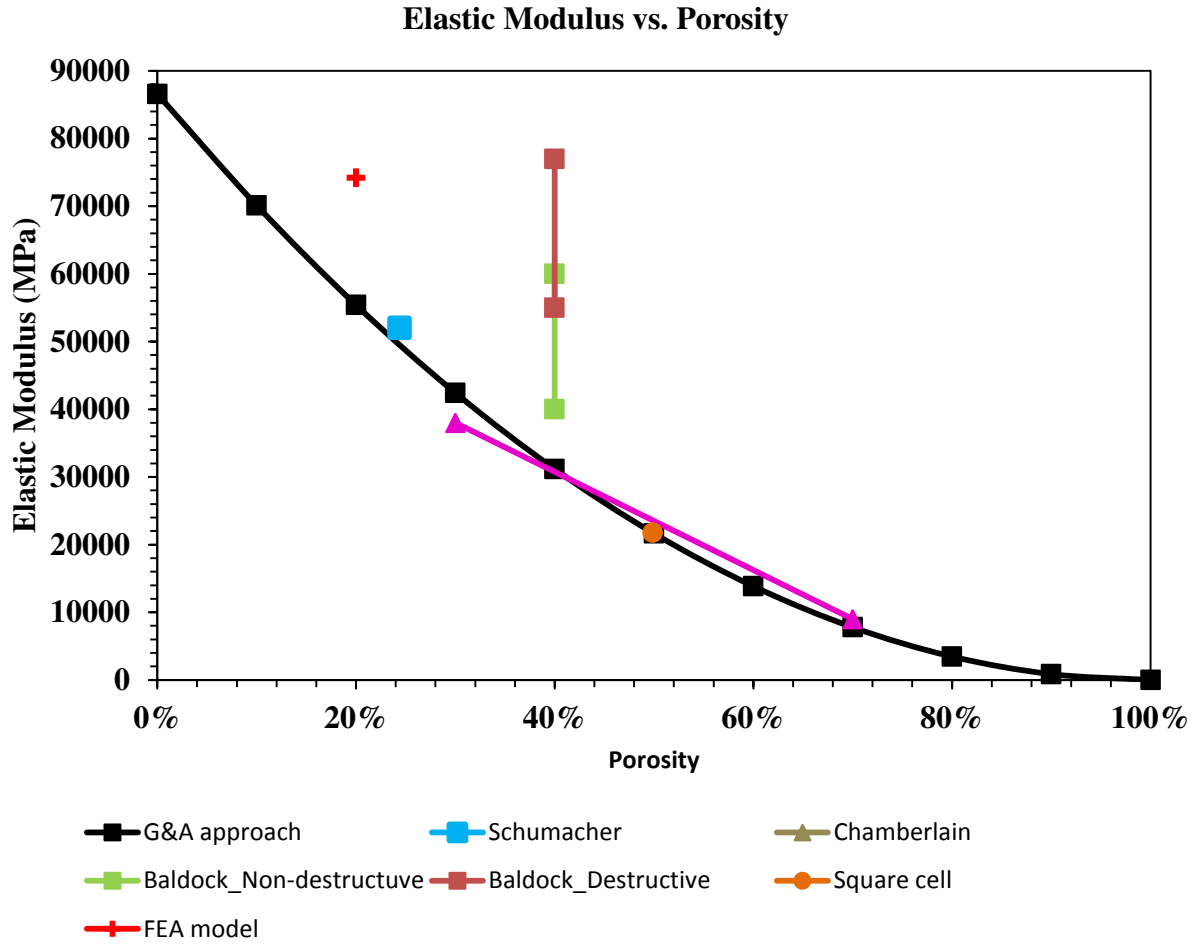
Figure 50: Elastic modulus for the *Acropora cervicornis* coral skeleton using the results obtained by the Gibson and Ashby approach for various levels of porosity. The values were compared to the elastic modulus found in the literature and the elastic modulus found using the finite element analysis simulation of the coral skeleton [5,90,116].

7. DESIGN AND DEVELOPMENT OF AN *IN-SITU* RAMAN SPECTROMETER INSTRUMENT TO DETECT REAL-TIME RESPONSE OF MATERIALS UNDER PHYSICAL STRESS: INSTRUMENT DESCRIPTION

Mechanical behavior of ceramic materials is important as it determines how materials respond and behave under the influence of external mechanical forces, which, in turn, defines the area of applications of ceramics. Properties like the strength and fracture toughness, when found to be high in ceramics, such as transformation toughened Y_2O_5 stabilized ZrO_2 [117], determines the application of ceramics as knives blades or medical scalpels [118]. If ceramics are super-hard, such as cubic BN [119] they are used as dies and anvil cells for high pressure applications [120]. If ceramics have a high Young's modulus and high hardness as for instance B_4C [121], they can be used as protective materials against ballistic impact [122]. As most of the ceramic materials with a few exceptions, such as, for example, $LaCoO_3$ or $LaMnO_3$ based perovskites, behave elastically, not only their strength and fracture toughness could be determined, but their elastic moduli could also be obtained from the stress-strain deformation plots collected during mechanical tests, therefore the techniques for the measurement of mechanical properties of ceramics are of high importance. Other materials of interest that resembles ceramic behavior are simulants used to study the surface of extraterrestrial bodies such as asteroids, planets and moons. A particular simulant is one that includes the mineralogy of CI carbonaceous asteroids. Different techniques have been developed for the measurement of mechanical properties of ceramics, such as uniaxial compression or tension, three- or four-point bending, biaxial testing, among others [123,124,125,42].

Mechanical properties as well as other physical properties of ceramics are directly dependent on the crystal structure and chemical composition of the material. Direct correlations have been found between the strength of the atomic bonds in the lattice and elastic constants as

well as melting temperature of ceramics [21]. Very often, the crystal structure of ceramics can undergo phase transformations, either due to change in the temperature or due to application of external stress [126,127]. Such changes in the crystal structure resulting in different transformations and different arrangement of the atoms in the lattice can bring dramatic changes in the mechanical behavior of the material. The phase change during loading could be very beneficial, as is the case of transformation toughening zirconia, or it could be very detrimental if it involves crack nucleation and propagation, or even the complete disintegration of the material as a result of the change of the crystal structure. For example, the change of the stiffness of $LaCoO_3$ perovskite was also detected [128]. It was measured that while pure $LaCoO_3$ exhibited Young's modulus equal to ~76 GPa at room temperature as calculated from the stress-strain deformation plots measured in 4-point bending, the value of the Young's modulus increased to ~120 GPa at 700-900 °C. Such increase in Young's modulus in $LaCoO_3$ with significant increase in temperature was very unusual, but no high temperature phase transition was detected by using high temperature X-ray or neutron diffraction that would help to explain such change in the stiffness. Thus, some other changes must occur in the structure of $LaCoO_3$ upon heating, which went undetected, and, therefore, using different techniques, such as *in-situ* Raman spectroscopy might provide an answer as to why such significant stiffening occurred in $LaCoO_3$ in 700-900 °C temperature range.

Besides of structural changes, the mechanical properties of ceramics are strongly affected by the presence of both bulk and surface defects that were introduced during the processing of the material. The defects, such as pores, agglomerates, and impurities act as stress concentrators which prompt instantaneous failure of brittle ceramics [19]. In addition, the presence of thermal residual stresses, which appear due to grain's anisotropy or mismatch of the coefficients of

thermal expansion in ceramic composites are also detrimental and can define mechanical performance of ceramics [129]. The techniques, such as X-ray diffraction or Raman spectroscopy, which allow to detect and to characterize both the defects and thermal residual stresses, would help to better understand and control the mechanical behavior of ceramics.

In most occasions, the structural characterization of ceramics is performed either before or after mechanical testing, leaving the gap in the knowledge of structural changes that can occur during the loading of the sample. However, in many modern testing techniques the unique opportunity to perform *in-situ* structural characterization of the material under the applied stress becomes available. Such structural characterization of ceramics under stress can be performed using *in-situ* X-ray or neutron diffraction [130,131], *in-situ* scanning electron and transmission electron microscopy, SEM and TEM, respectively [132,133], or *in-situ* Raman spectroscopy [134]. All these techniques allow for a better understanding of the structural changes in ceramics during the mechanical loading, thus allowing for a better understanding of the material responses leading to different mechanical behavior and failures. While numerous approaches have already been used for such *in-situ* characterization, still significant improvement can be achieved, if either a better resolution or more distant methods would be implemented for such structural characterizations that were not available before. This chapter describes the development and assembly of an optical probe to perform *in-situ* Raman spectroscopy characterization on ceramic samples during uniaxial compressive loading.

7.1. <u>Instrument Description</u>

7.1.1. Hardware

The idea of coupling a universal testing machine with an *in-situ* Raman spectrometer via an optical probe using fiber optics came from the need of collecting real-time structural response

from Raman active ceramics when they undergo mechanical stress by externally applied load. For such system, the In-via® Raman spectrometer (Renishaw PLC, Gloucestershire, the UK) connected both to the optical microscope (Leica Microsystems GmbH, Wetzlar, Germany) and to the optical probe (Renishaw PLC, Gloucestershire, the UK) for the collection of backscattered light was used. A 532 nm Si solid laser with a maximum power of 300 mW was used for the excitation of ceramics. The XYZ movement of the optical probe was controlled by a Velmex stage which consisted of two Vexta stepping motors (Oriental Motor, Tokyo, Japan). One of these Vexta stepping motors provided control for the Y- and Z-axis motion, while the other was in charge of the motion along the X-axis. The two stepping motors were controlled by two VXM controllers (Velmex Inc., New York, USA) which provided 0.005 mm/step resolution in the X- and Y-directions and 0.0016 mm/step resolution in the Z-direction. Three objective lenses were available to be used for focusing of the optical probe on the surface of the ceramic sample. Both, 50x objective lenses with working distance of 18 mm and two 20x objective lenses with 12 mm and 25 mm working distances were available for better focusing and collection of Raman signal from the surface of the ceramic sample. The ceramic characterized by Raman spectroscopy was fixed using a Criterion® universal testing machine (MTS Systems Corporation, Minnesota, USA) subjected to the applied uniaxial compressive stress. A schematic presentation of the experimental set-up is presented in Figure 51 and the real set up is shown in Figure 52.

(A)
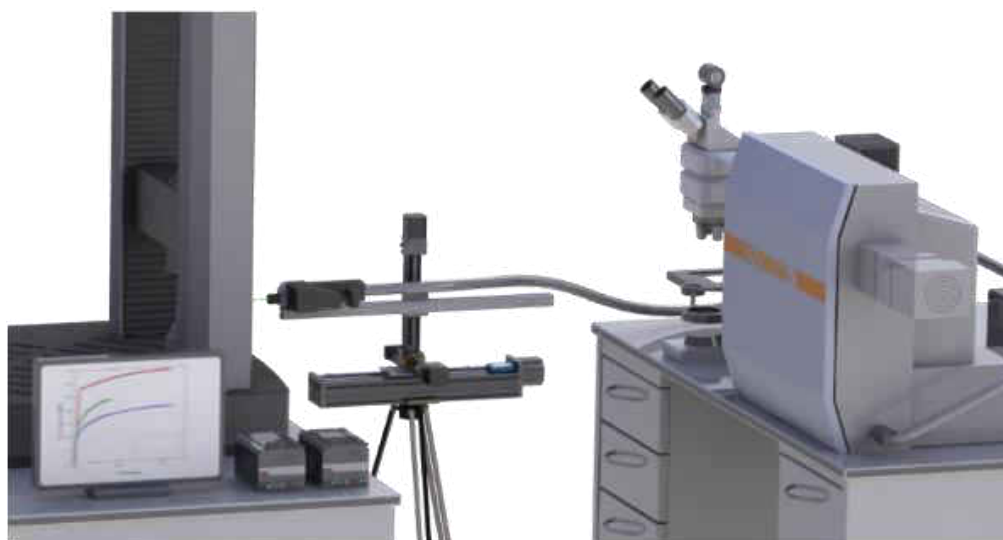
(B)
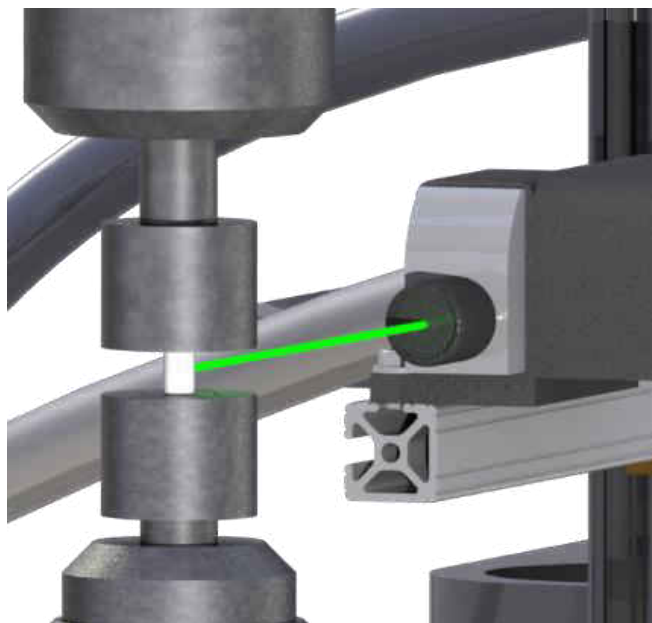
Figure 51: Computer model of the set-up for the probe designed for *in-situ* Raman spectra of ceramic materials showing the spectrometer, the universal testing machine, the optical probe and the optical microscope.
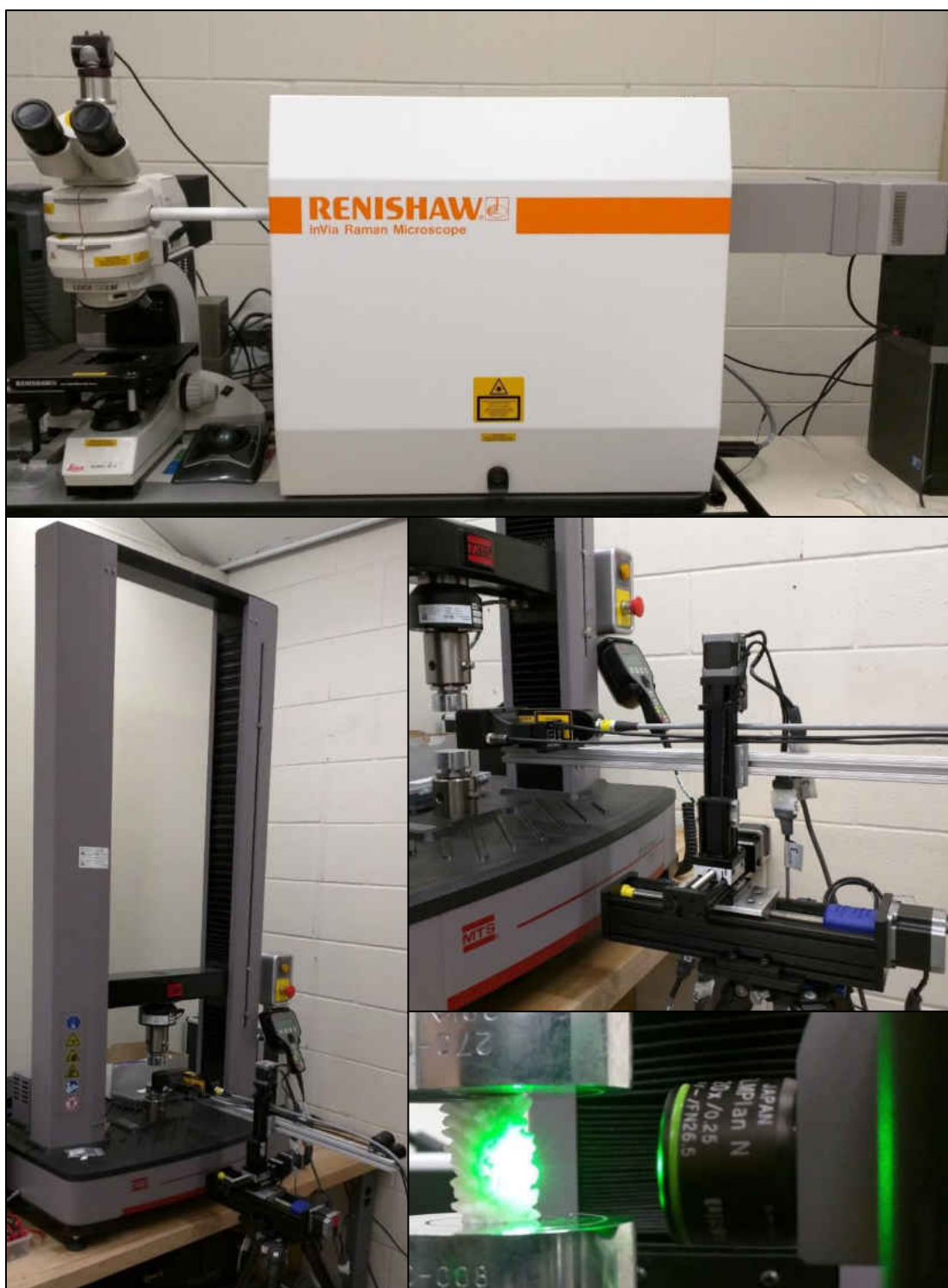
Figure 52: Components used for the development of the Raman spectroscopic probe for *in-situ* analysis of ceramic materials.

7.1.2. Software

For the full development of the instrument it was necessary to develop software that could make the XYZ-stage, the stepper motors and the Raman spectra processing software interact among themselves and make the process automatic. In order to achieve this goal, the process was divided into different steps that dealt with each fundamental part of the functionality of each component of the system and allowed them to work in synergy. The steps can be summarized as: (1) defining the collection area on the sample surface; (2) develop the code to move the XYZ-stage automatically using the stepper motor controllers following the collection area defined on the previous step; (3) allow for the Raman collection software to send a signal to the stepper motor controllers after each collected point to trigger the motion of the stage to the next collection point in the defined area.

For the first step, collecting the data for a 2D Raman maps was done by dividing the sample's image surface into a user-defined grid and scanning throughout the grid cells by moving the probe using the Velmex stage and the VXM stepping motors, collecting the Raman spectrum at each position.

An automated system was created to move the probe along the grid, trigger the spectrometer on each cell of the grid, and acquire the data from the scan. Velmex stepper motors could be controlled using either the buttons on the hardware or through the computer software, COSMOS® provided by Velmex Inc. which provides a command line tool to send commands to the stepper motors and move the probe in XYZ directions for the desired amount, usually 0.05-0.5 mm for the XY-movement of the stage that defines the plane desired to analyze. But COSMOS® did not satisfy the features that were needed to achieve the grid-based scan because it was not able to interact directly with WiRE® 3.4 ((Renishaw PLC, Gloucestershire, the UK).

Velmex Inc. also provided the drivers for stepper motors and program scripts for different programming languages to integrate Velmex stepper motors controller inside a third party created software. This feature allowed for the communication with the stepper motor inside the custom-made program and move the stepper motors arbitrary to the desired positions.

The next step consisted in controlling the Raman Spectrometer from the automated data acquisition software. To control the In-via® Raman spectrometer, Renishaw PLC provided a software called WiRE® 3.4 which interacted with the spectrometer and collected the spectrum data. WiRE® 3.4 is proprietary software and does not provide the source code for the software. Therefore, access was not granted to the software code in order to modify it and create the required features for automatic grid scan. To solve the problem, a solution other than modifying the source code had to be found. WiRE® 3.4 had different modes for data acquisition. One of these data acquisition modes provided a tool that could be used to ask WiRE® 3.4 to collect X-number of data collections and wait for a software inter-process call between each data collection. A software inter-process call is a programming concept to allow communication between two different software without accessing each other's environment. Inter-process calls are usually handled by the operating system, but in some cases, programmers define their own protocols to send and receive calls on their software. The case with WiRE® 3.4 is the latter. The WiRE® 3.4 software documentation provided a few details on how the inter-process communication was implemented and how a Visual Basic script could be used to send and receive calls. Using this method, the number of data acquisitions was defined on WiRE® 3.4 and triggered the acquisitions from an external program.

To create the automated data acquisition software, Visual Basic programming language was used since WiRE® 3.4 inter-process communication only supports this language. The

process of acquiring the data by our system started with calculating the grid size. If data acquisition wanted to be performed on a grid of m by n, the system would be acquiring data on $n \times m$ grid cells. Then it was needed to find the *step size* for the scan. The *step size* is the magnitude of the Velmex stepper motors movement between each scan, in other words, step size is the distance that the probe should move between each cell of the grid. Using m and n a new data acquisition could be created in WiRE® 3.4 to acquire data $n \times m$ times and wait for software trigger before each acquisition. Then the task was able to start on WiRE® 3.4. Since software trigger was used, the scan did not start until it received a trigger from external software.

In the next step, the automation software was opened. The software started by scanning the COM ports and recognizing the connected Velmex device, then it turned it online by sending the online command. Once the device was online, the graphical user interface of the software was displayed. Different modes of data acquisitions were chosen and also the optical probe was able to be moved through the graphical user interface. To focus the laser on the object, the physical buttons on the stepper motors control became handy as it could be used to easily move the probe further or closer to the object to perform the focus process. Manual controls were used to move the probe precisely to the desired starting point.

When the object was in focus and WiRE® 3.4 was waiting for software triggers, the m, n, and the step size information were entered in the software for a rectangular- or linear-shaped scan. After entering the parameters, the start button could be clicked to start the data acquisition. The automation software sent a trigger command to WiRE® 3.4, then it moved the probe in a snake pattern throughout the grid and each time it moved the probe, it sent a software trigger to WiRE® 3.4 to acquire the data. Thus, both hardware such as an optical probe supported on the

operational XYZ Velmex-stage and the software became operational and ready to use to perform mechanical testing of ceramic samples coupled with *in-Situ* Raman spectroscopy.

7.2. <u>Results from Different Ceramic Materials Analyzed with the Developed Raman Probe</u>

7.2.1. Asteroid Simulant

An application of this newly developed instrumentation was used to analyize the strength properties of asteroid regolith simulant. The series of planetary regolith simulants was developed by the Center for Lunar and Asteroid Surface Science, in partnership with Deep Space Industries, to provide a high-fidelity material analog to the surface material found on extraterrestrial worlds such as asteroids, the Moon, and Mars. By replicating the mineralogy of these parent materials we can capture many of the physical and chemical properties of the surface material. Simulants are a valuable resource for the planetary science and engineering communities for mission design, spacecraft development, instrument testing, and modeling.

Since smectite is the "cement" for these types of meteorites, we will test the effect of varying smectite content on the strength of the resulting mixture. For the smectite-enrichment testing 7 test cylinders were fabricated from the UCF/DSI simulant, CI-V3 based on the mineralogy of Orgueil-type CI Carbonaceous Chondrite [135]. This type of meteorite represents volatile-rich, very friable primitive asteroid material, thought to be likely analogs to the P and D asteroid spectral types [136]. They are of particular exploration interest as a potential source for water and carbon compounds, shielding material, and as a scientific window on the more primitive materials of the solar nebula. The base mineralogy of the simulant is shown in Table 4 and Table 5 [137], while CI-V3 simulant maintains a smectite weight of 5% which acts as a cement to hold together what is essentially a conglomerate of dissimilar materials. To study the effects of varying smectite content on the compressive strength of the material the weight % of

smectite was increased in each successive sample to 7.5, 10, 12.5, 15, 17.5, and 20 wt. % smectite while maintaining the relative proportion of all other minerals.

Table 4: Composition of the asteroid simulant

Orgueil-type CI Carbonaceous Chondrite V3	
	Wt. %
Olivine (Fo90)	7
Pyrite	6.5
Vermiculite	9
Magnetite	13.5
Mg Serpentine	48
Smectite	5
Epsomite	6
Kerogen (Sub-bituminous coal)	5

Table 5: Bulk chemistry of the asteroid

Oxide	Wt%
SiO_2	25.0
TiO_2	0.5
Al_2O_3	3.1
Cr_2O_3	0.2
FeO_T	25.8
MgO	30.2
CaO	3.0
Na_2O	6.4
K_2O	0.4
P_2O_5	0.4
SO_3	4.9
Cl	0.0
Total	99.9

This CI-V3 simulant is a close mineralogical match to CI carbonaceous chondrites with the following caveats. The organic component of volatile rich carbonaceous chondrites contain polycyclic aromatic hydrocarbons (PAHs), some of which are known carcinogens and mutagens.

Our research suggests that rough chemical fidelity can be maintained by substituting much safer sub-bituminous coal as our organic analog. A second safety consideration is the choice of serpentine group materials. While most serpentine polymorphs are quite safe, we avoid fibrous chrysotile because of its asbestos content. In the same vein, pyrite was substituted for troilite because of troilite's tendency toward combustion and/or explosion in small particle sizes. The particle size was designed to peak at 70 microns, based on data from CI meteorites. For strength testing the material was cast into short cylinders called "pucks". It was found that the bulk density of the CI carbonaceous asteroid simulant was mid-way between the CI Ivuna (1.95 g/cm^3) and the CI Orgueil (1.61 g/cm^3) [138,139]; the grain density was higher than CI Ivuna and Orgueil by ~0.2 g/cm^3 [138,139]; the porosity was consistent with the Orgueil and a slightly higher than Ivuna [138,139].

The cylinders were cast by wetting the simulant powder at a ratio of one gram (or milliliter) of de-ionized water for every 4 grams of simulant. The water was mixed until a frosting-like consistency is achieved and then the simulant mixture was transferred to a 25.4 cm diameter by 50.8 cm length mold for casting. Once cast the cylinders were oven dried at 50°C for 24 hours.

After casting and heat treatment the sample dimensions were on average 24.5 mm in diameter and 49.0 mm in length. The samples were then tested under mechanical uniaxial compression while the Raman response on a single point was being recorded. Figure 53 shows an image of one asteroid simulant sample with 10 wt. % smectite and the Raman response before and during compression. The Raman response of the sample showed a slight shift to the right of the Raman band corresponding to 1615.29 cm^{-1} accompanied by a decrease in the intensity of the response. This behavior is on the Raman response occurred due to the change of frequency of the

excited molecules in response to the influence of the compressive stresses in the sample [134].

The sample was exposed for 100 s using a 20x magnification lens and 10% of the total laser

power to avoid any burning damage on the surface of the material and an overshoot reading.
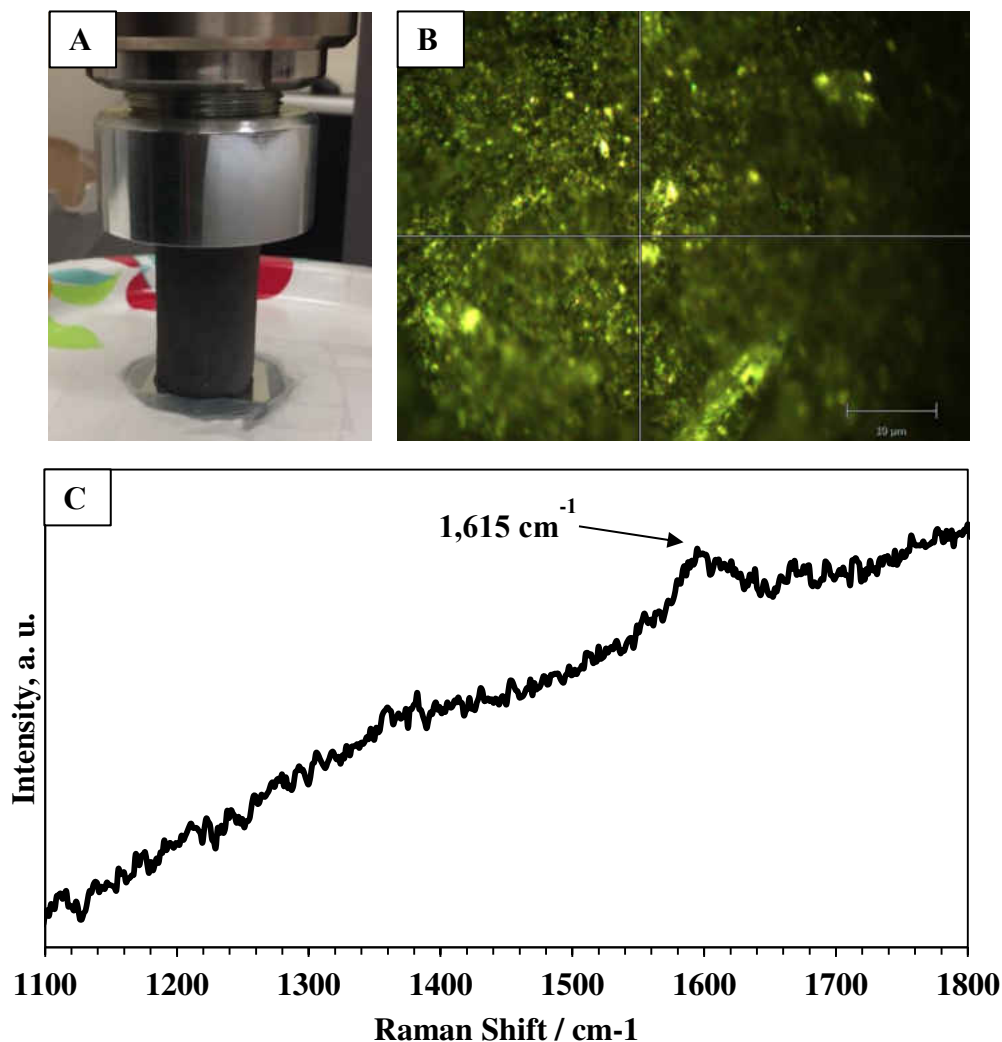
Figure 53: Set-up of the asteroid simulant sample with 10% smectite tested under compression with the Raman spectra analyzed by the optical probe designed. (A) Asteroid simulant sample loading set-up for the compression test. (B) Micrograph captured using a 20x objective lens installed on the optical probe. (C) Raman spectra collected utilizing the *in-Situ* **optical probe.**

7.2.2. LaMnO$_3$ Vibrational Response

In order to validate the accuracy and effectiveness of the developed probe the vibrational response of a LaMnO$_3$ sample was recorded. The sample was stressed at a compressive load of 4 kN and the Raman spectra showing the behavior of the ceramic under this load was analyzed and compared to the vibrational response of the same sample with no load. Figure 54 shows the results obtained from the vibrational response of the LaMnO$_3$ sample analyzed using the *in-situ* optical probe using a 20x objective lens exciting the sample with a 300 mW green light laser at 10% power for 200 s of exposure time for a range of 50-1000 cm^{-1}.

From Figure 54 a reduction and broadening of the two major peaks identified, occurring in the bands of 489 cm^{-1} and 600 cm^{-1} can be observed product of the compression stress resulting from the 4 kN load as well as a slight shift of the two peaks towards the left side. From this image the concept of capturing *in-situ* Raman response can be proved and the functionality of the equipment can be validated. The type of load applied to the sample as well as the ability to increase the magnitude of it depends on the availability of the equipment and the type of load cell used.
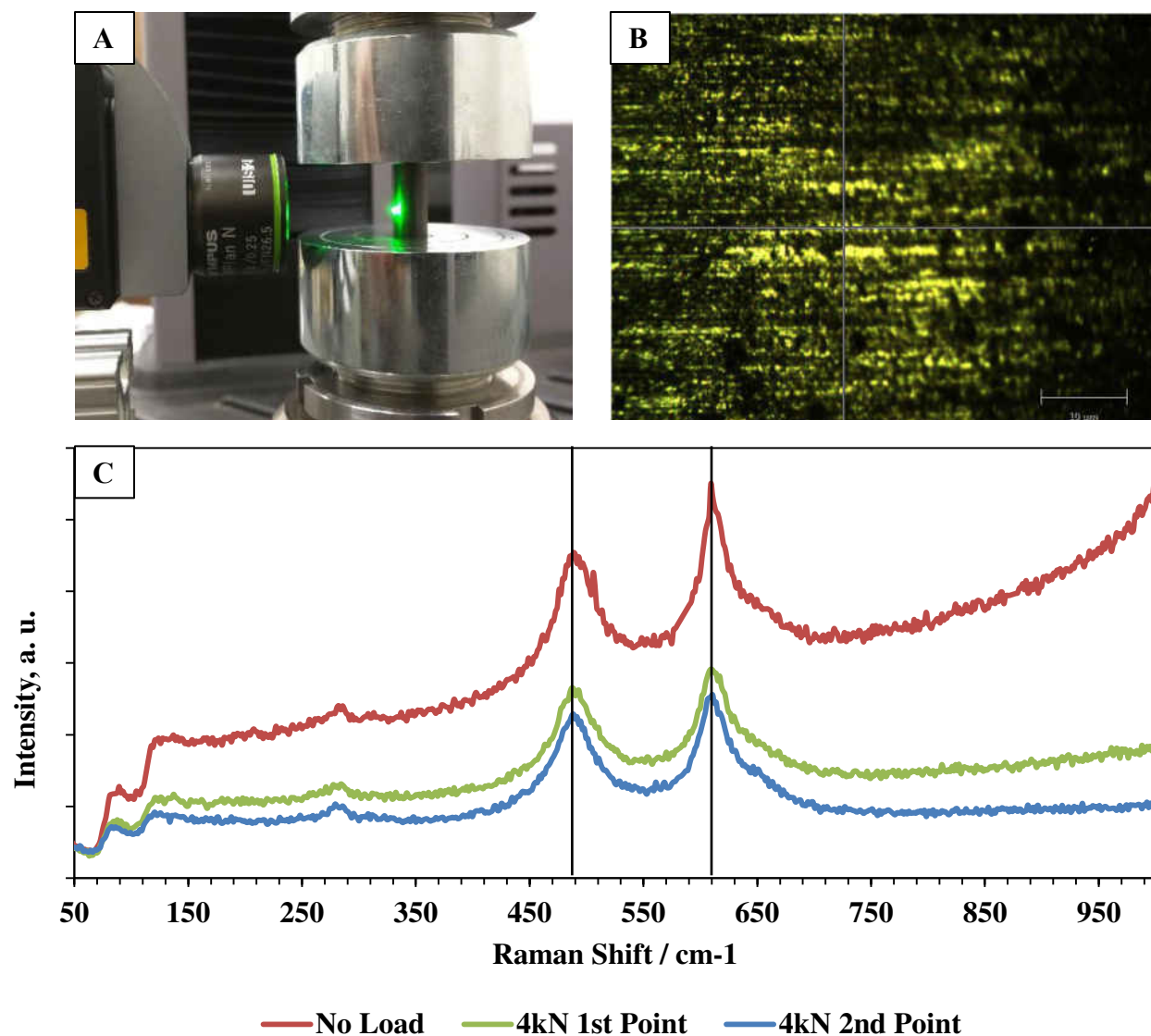
Figure 54: Raman spectra collected using the *in-situ* optical probe for a LaMnO₃ rectangular sample showing its response for two loading cases: no load and under a 4kN load. (A) Set-up for the compression loading experiment and the collection of the Raman spectra. (B) Micrograph of the LaMnO₃ sample obtained using a 20x objective lens installed on the optical probe. (C) Raman spectra for the no load (red) sample, and at two random points (blue and green) of the sample loaded at 4 kN collected with the *in-situ* optical probe.

7.2.3. Other Samples Tested

The Raman spectra of other samples tested using the *in-situ* optical probe was collected in order to validate the accuracy of the instrument. To do this, the use of *Acropora cervicornis* coral skeleton and ZrO_2 as model samples was done and the Raman spectra collected. For the *Acropora cervicornis* coral skeleton (Figure 55) the identification of the major peak at 1080 cm^{-1} was used as a source of validation, and for the ZrO_2 the comparison between the spectra collected using the microscope stage and the *in-situ* optical probe was done (Figure 56).
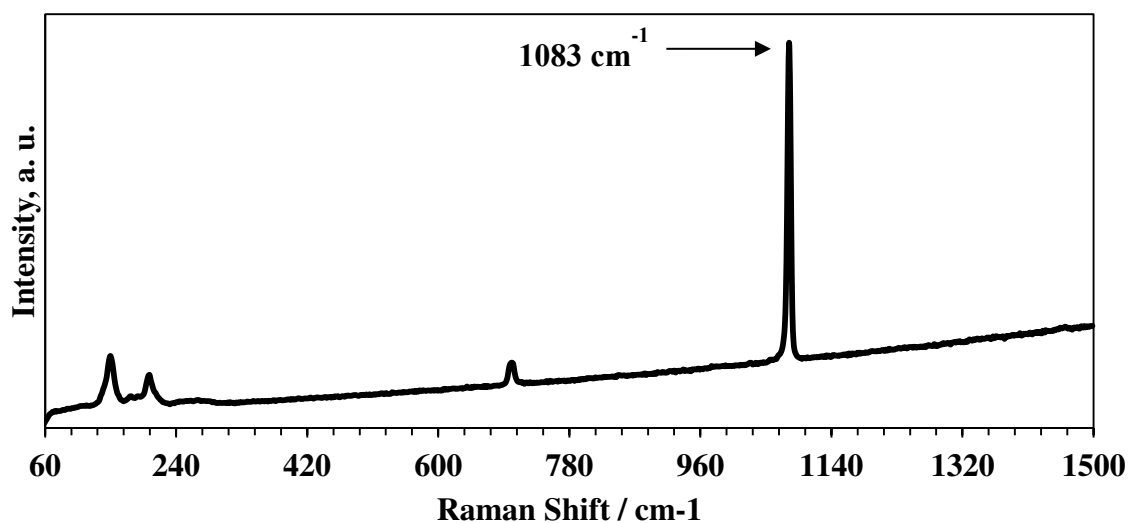
Figure 55: Raman spectra of the *Acropora cervicornis* coral skeleton taken using the *in-situ* optical probe using a 300 mW green laser at 50% laser power with an exposure time of 10 s using a 20x objective lens collecting data for the bands between 60-1500 cm^{-1}.
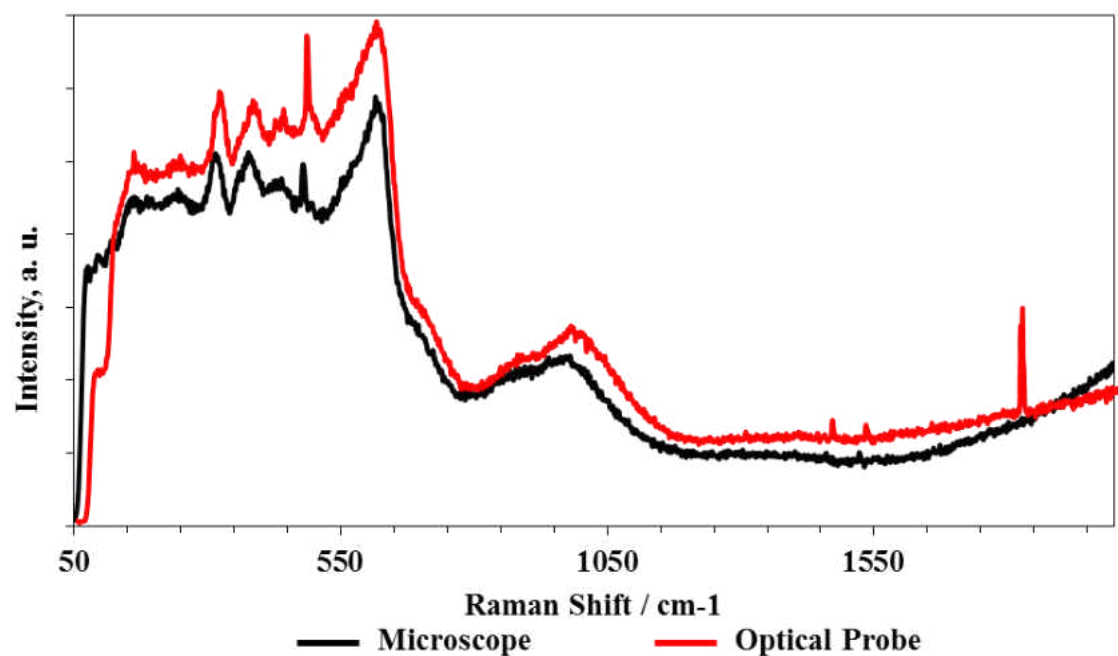
Figure 56: ZrO₂ Raman spectra obtained from the microscope stage (Black) and the designed *in-situ* Optical Probe (Red) using a 300 mW green laser at 50% laser power with an exposure time of 200 s using a 20x objective lens collecting data for the bands between 50-2000 cm⁻¹.

8. CONCLUSIONS

A ring-on-ring biaxial flexural strength fixture was developed in-house to test the biaxial strength of different disk-shaped ceramic components. This test was selected due to the simplicity in design and development of the jigs by following the ASTM C-1499 standard. A significant disadvantage of this method is the requirement for flat parallel samples that makes their preparation extensive and time consuming and not permitting for the testing of as-sintered samples. A model ceramic material composed of ZrB_2-30wt%SiB_6 sintered using SPS technique was used to validate the manufactured ring-on-ring fixture. The X-ray diffraction was used to obtain the phase composition of the model ZrB_2-30wt%SiB_6 ceramic composite while optical microscopy was used to calculate the grain size distribution. X-ray diffraction analysis showed that the ZrB_2 phase was stable while the SiB_6 phase was non-stable after sintering of the composite. The non-homogeneous phase distribution was measured by optical microscopy showing the appearance of large agglomerates/grains in ZrB_2-30wt%SiB_6 composite. The Resonant Ultrasound Spectroscopy was used to measure elastic properties of the composite both at room and high temperature in an Ar protective environment. The calculation of the biaxial strength was simplified by using simple-plate theory, which only depends on the Poisson's ratio of the material being tested, as specified by the ASTM C1499 standard. The measured values of biaxial strength using ring-on-ring jig were compared to a model developed using the finite element method for the elastic region of the ceramic composite assuming a homogeneous material. This finite element analysis showed a close correlation to the experimental results from which it can be concluded that the jig designed was validated since the maximum absolute stress occurred in the tensile surface region of the ceramic disk enclosed by the load ring with a value of 224.9 MPa, decreasing gradually as the radius of the disk increases

The mechanical response of a skeleton of the coral *Acropora cervicornis* to uniaxial compressive loading and sharp Vickers indentation was studied. The results show that the skeleton structure can withstand the cyclic distributed forces of ocean waves and also, to a certain extent, resist highly-concentrated compressive forces. Skeletons of *Acropora cervicornis* have a unique and complex microstructure with substantial porosity, and pores have different shapes and orientations. Skeleton porosity and aragonite crystals' growth directions contribute to "gracious" failure, which extends the instantaneous catastrophic failure to higher loads and deformations. Cylindrical samples cut from the skeleton of a nursery-reared *Acropora cervicornis* exhibited maximum compressive stress of 18.98 ± 5.74 MPa and a micro-hardness of 3.56 ± 0.31 GPa. The anisotropic pores serve as strengthening and toughening elements for the coral skeleton's resistance to fracture in the harsh marine environment, thus contributing to its ability to resist cracking. Further load increase ultimately caused the skeleton to fail catastrophically, with a crack propagated and splitting into two or more non-uniform sections, with the formed fracture surfaces parallel to the applied compression load. In nature, *Acropora cervicornis* distributes applied stresses (e.g., when impacted by marine debris or kicked by a snorkeler) throughout its lattice-like skeleton and fails gradually, until the skeleton finally cracks along its longitudinal axis. However, a more common outcome is that shearing and torsional stresses would snap the skeleton before compression failure occurs. As shown by micro-Raman spectroscopy, the coral skeleton consisted of an aragonite structure rather sensitive to the applied compressive stress, resulting in a decrease of intensity and an increase in FWHM of the 1083 cm^{-1} Raman peak. However, the position of the Raman active 1083 cm^{-1} peak was weakly sensitive to the applied compressive stress. Thus, *Acropora cervicornis* can also resist indentations in the natural environment, such as from grazers (except those with very powerful beaks or jaws,

including parrot fish and sea urchins). Measurements of the flow-field of the moving coral-skeleton using PIV showed that its wake resembles that of a bluff body, and is characterized by the existence of vortex shedding. However, due to high surface roughness of the coral-skeleton, the larger scale vortices were not stable and soon disintegrated into smaller scale vortices. The hydrodynamic load acting on the coral structure is indeed linked to the strength of these vortical elements in the wake.

The solid model of a coral skeleton was developed using graphical techniques that split the frames of a video collected using CT scan and with the use of Mimics® the volume mesh was generated. This model allowed for the study of the coral skeleton and its response under compressive load furthering understanding the complex microstructure of this organism. The elastic modulus of pure $CaCO_3$ was modified accounting for the porosity of the coral skeleton measured using image processing techniques to tune the accuracy of the model and obtain realistic results from the simulation.

An *in-situ* optical spectrometer for the vibrational response of Raman active material was developed to obtain the real-time response of ceramic materials subjected to different states of stress applied through a universal testing machine. The instrument is able to analyze materials by the exciting them with a green laser on a localized point that can be used individually or put together with other points and develop a map that can provide an image of the defects in the surface and sub-surface of the ceramic. This technique can be further developed to study the accumulation of stress the material is experiencing under the loading case it is exposed. The system consisted of an in-Via® Raman system coupled to a fiber optics cable that conducted the laser to the optical probe and allowed for the excitation of the material surface and the collection of the Raman radiation released by it, which was alter processed by the CCD and the software

Wire®. In order to collect maps and gain a good focus in the sample surface the stage had to move in the XYZ axes. This motion was achieved by the development of an in-house program that used the software Cosmos® as the controller of the stepping motors that triggered the motion of the screws controlling the stage. The generation of the maps was done using data analysis with the open source programming language Python^{TM} which permitted the manipulation of the information collected in every point of a map that were translated graphically and color coded to depict the variance in the parameters of the maps.

.

APPENDIX A: BIAXIAL STRENGTH RESULTS FOR THE ZrB$_2$-30wt%SiB$_6$ BRITTLE

CERAMICS

The biaxial flexural strength of three samples of ZrB_2-30wt% SiB_6 was obtained through the ring-on-ring test developed in-house. The elastic properties for the calculation of the maximum stress, as well as the stress-strain plot were found by resonant ultrasound spectroscopy at the University of Texas A&M.
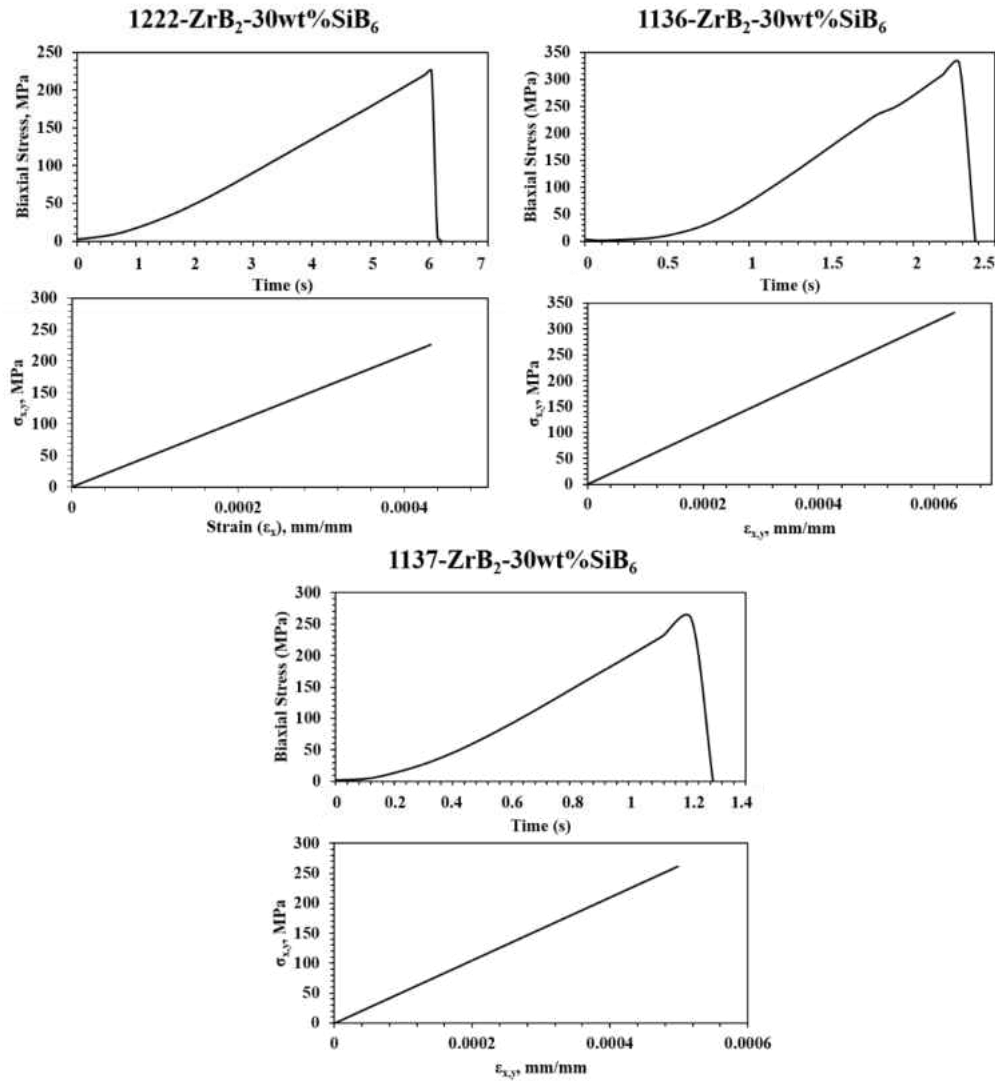
Figure A 1: Biaxial stress and stress-strain plot for three samples of ZrB_2-30wt% SiB_6.

APPENDIX B: VICKERS HARDNESS AND COMPRESSION TEST RESULTS OF

BLEACHED ACROPORA CERVICORNIS CORAL SAMPLES

B.1. <u>Vickers Hardness of Bleached Coral Samples</u>

The Vickers hardness was obtained using a load of 50 grams on 13 random points on the pristine polished surface of a bleached coral sample.

Table B 1: Vickers hardness measurement on bleached coral sample

Bleached Sample		
Indent	**Load (g)**	**Measured Hardness (GPa)**
1	50	3.36
2	50	3.26
3	50	3.58
4	50	3.31
5	50	3.37
6	50	3.53
7	50	3.56
8	50	3.54
9	50	3.33
10	50	3.55
11	50	3.43
12	50	4.40
13	50	4.05
Average		3.56
Std. Dev.		0.31

B.2. Compression of Bleached Coral Samples

Bleached coral samples were compressed at a constant rate of 0.03 mm/s until complete failure using an electromechanical universal testing machine MTS Criterion C43. The plot of four stress-time plot of four samples can be found in
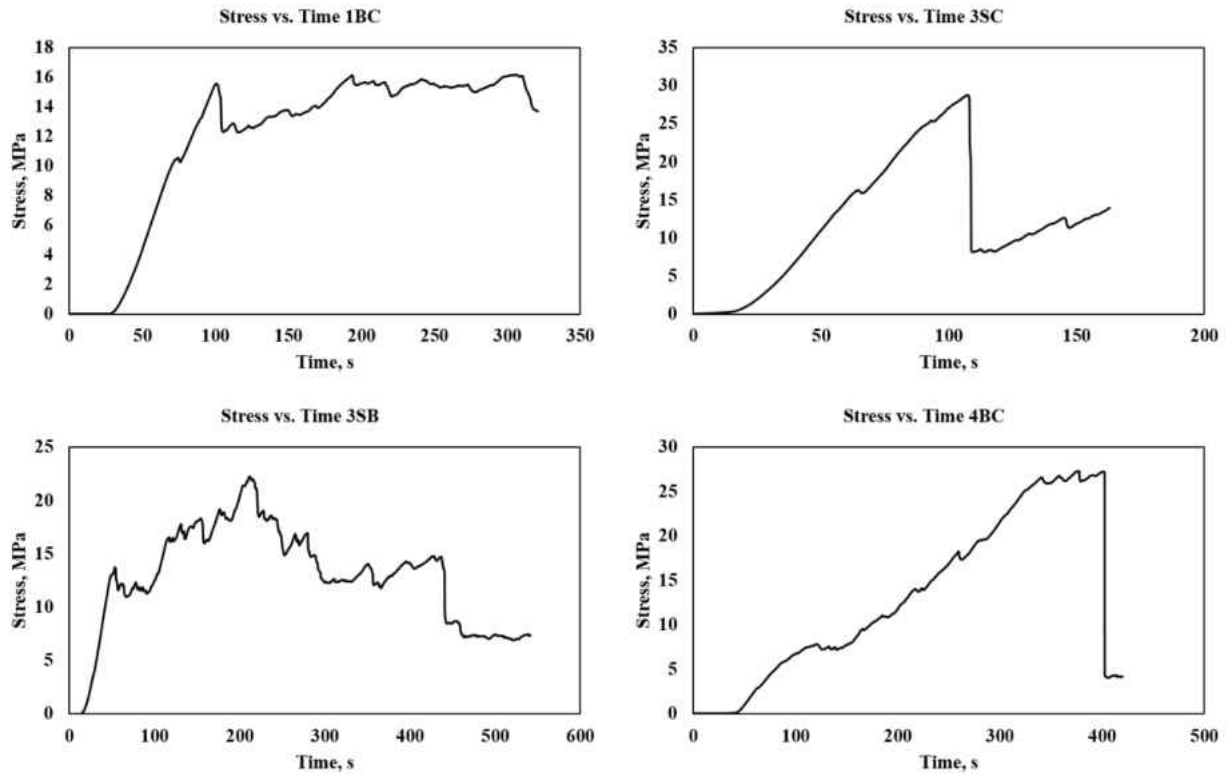
Figure B 2: Stress-time plot of four different bleached coral samples indicating different points of failure and showing a behavior of failure by stages.

REFERENCES

[1] A. Paul, D. D. Jayaseelan, S. Venugopal, E. Zapata-Solvas, J. Binner, B. Vaidhyanathan, A. Heaton, P. Brown, and W. E. Lee, "UHTC composites for hypersonic applications", *The American Ceramic Society Bulletin*, vol. 91, pp. 22-28, 2012.

[2] E. Zapata-Solvas, D. D. Jayaseelan, H. T. Lin, P. Brown, and W. E. Lee, "Mechanical properties of ZrB_2- and HfB_2- based ultra-high temperature ceramics fabricated by spark plasma sintering", *Journal of the European Ceramic Society*, vol. 33, pp. 1373-1386, 2013.

[3] W. G. Fahrenholtz, and G. E. Hilmas, "Refractory diborides of zirconium and hafnium", *Journal of the American Ceramic Society*, vol. 90, pp. 1347-1364, 2007.

[4] S. Q. Guo, "Densification of ZrB_2-based composites and their mechanical and physical properties: A review", *Journal of the European Ceramic Society*, vol. 29, pp. 995-1011, 2009.

[5] J. A. Chamberlain, Jr., "Mechanical properties of coral skeleton: Compressive strength and its adaptive significance", *Paleobiology*, vol. 4, pp. 419-435, 1978.

[6] F. Morbeg, and C. Folke, "Ecological gods and services of coral reef ecosystems", *Ecological Economics*, vol. 29, pp. 215-233, 1999.

[7] C. Sheppard, D. J. Dixon, M. Gourlay, A. Sheppard, and R. Payet, "Coral mortality increases wave energy reaching shores protected by reef flats: Examples from the Seychelles", *Eustarine, Coastal and Shelf Science*, vol. 64, pp. 223-234, 2005.

[8] H. J. S. Fernando, J. L. McCulley, S. G. Mendis, and K. Perera, "Coral poaching worsens tsunami destruction in Sri Lanka", *Eos*, vol. 86, pp. 301-304, 2005.

[9] J. S. Madin, A. I. Dell, E. M. P. Madin, and M. C. Nash, "Spatial variations in mechanical properties of coral reed substrate and implications for coral colony integrity", *Coral Reefs*, vol. 32, pp. 173-179, 2012.

[10] J. M. Pandolfi, R. H. Bradbury, E. Sala, T. P. Hughes, K. A. Bjorndal, R. G. Cooke, D. McArdle, L. McClenachan, M. J. Newman, G. Paredes, and R. R. Warner, "Global trajectories of the long-term decline of coral reef ecosystem", *Science*, vol. 301, pp. 955-958, 2003.

[11] D. R. Bellwood, T. P. Hughes, C. Folke, and M. Nyström, "Confronting the coral reef crisis", *Nature*, vol. 429, pp. 827-833, 2004.

[12] T. P. Hughes, N. A. Graham, J. B. Jackson, P. J. Mumby, and R. S. Steneck, "Rising to the challenge of sustaining coral reef resilience", *Trends in Ecology & Evolution*, vol. 25, pp. 633-642, 2010.

[13] L. J. McCook, J. Jompa, and G. Diaz-Pulido, "Competition between corals and algae on coral reefs: a review of evidence and mechanisms", *Coral Reefs*, vol. 19, pp. 400-417, 2001.

[14] M. W. Miller, and M. E. Hay, "Effects of fish predation and seaweed competition on the survival and growth of corals", *Oecologia*, vol. 113, pp. 231-238, 1998.

[15] V. Tunnicliffe, "Breakage and propagation of the stony coral *Acropora cervicornis*", *Proceedings of the National Academy of Sciences of the United States of America*, vol. 78, pp. 2427-2431, 1981.

[16] D. Huang, "Threatened reef corals of the world", *PLoS ONE*, vol. 7: e34459, doi:10.1371/journal.pone.0034459

[17] Kok, Albert. (May 2, 2007). *Hertshoorn Koraal.* [Photograph]. Retrieved from https://en.wikipedia.org/wiki/Staghorn_coral#/media/File:Hertshoon.jpg

[18] J. R. Ferraro, K. Nakamoto, C. W. Brown, "Chapter 1 - Basic Theory", Editor(s): J. R. Ferraro, K. Nakamoto, C. W. Brown, "Introductory Raman Spectroscopy (Second Edition)", *Academic Press*, 2003, Pages 1-94, ISBN 9780122541056

[19] R. Danzer, T. Lube, P. Supancic, R. Damani, "Fracture of ceramics," *Advanced Engineering Materials*, vol. 10, (4): pp. 275-298, 2008.

[20] M.W. Barsoum, *Fundamentals of ceramics*: Institute of Physics, 2003.

[21] D.J. Green, *An introduction to the mechanical properties of ceramics*: Cambridge University Press, 1998.

[22] J. Pelleg, *Mechanical properties of ceramics*. Solid mechanics and its applications, vol 213: Springer, 2014.

[23] J. B. Watchman, *Mechanical properties of ceramics*: Wiley, 1996.

[24] D. Munz, and T. Fett, *Ceramics. Mechanical properties, failure behaviour, materials selection* vol. 36: Springer, 1999.

[25] Lawn, B.R., *Fracture of brittle solids:* Cambridge University Press, 1993.

[26] A. A. Griffith, "The Phenomena of Rupture and Flow in Solids," *Philosophical Transactions of the Royal Society of London,* vol. 221, 163-198, 1920.

[27] R. Morell and N. P. Laboratory, *Fractography of brittle materials*: National Physical Laboratory, 1999.

[28] R. Danzer, "Mechanical failure of advanced ceramics: The value of fractography" *Key Engineering Materials*, vol. 223, pp. 1-18, 2002.

[29] J. Dusza, "Fractographic failure analysis of brittle materials". *International journal of Materials and Product Technology*, vol. 15, P. 292, 2003.

[30] ASTM Standard C1275, 2018 (1994), "Standard test method for monotonic tensile behavior of continuous fiber-reinforced advanced ceramics with solid rectangular cross-section test specimens at ambient temperature", ASTM International, West Conshohocken, PA, 2018, DOI:10.1520/C1275-18.

[31] ASTM Standard C1273, 2015 (1994), "Standard test method for tensile strength of monolithic advanced ceramics at ambient temperatures", ASTM International, West Conshohocken, PA, 2018, DOI:10.1520/C1273-15.

[32] ASTM Standard C1366, 2013 (1997), "Standard test method for tensile strength of monolithic advanced ceramics at elevated temperatures", ASTM International, West Conshohocken, PA, 2018, DOI:10.1520/C1366-04R13.

[33] J. R. Davis, *Tensile testing*: ASM International, 2004

[34] ASTM Standard C1161, 2018 (1990), "Standard test method for flexural strength of advanced ceramics at ambient temperature", ASTM International, West Conshohocken, PA, 2018, DOI:10.1520/C1161-18.

[35] ASTM Standard C1211, 2018 (1992), "Standard test method flexural strength of advanced ceramics at elevated temperatures", ASTM International, West Conshohocken, PA, 2018, DOI:10.1520/C1211-18.

[36] ASTM Standard C1684, 2018 (2008), "Standard test method for flexural strength of advanced ceramics at ambient temperature − cylindrical rod strength", ASTM International, West Conshohocken, PA, 2018, DOI:10.1520/C1684-18.

[37] ASTM Standard C1358, 2013 (1996), "Standard test method for monotonic compressive strength testing of continuous fiber-reinforced advanced ceramics with solid rectangular cross-section test specimens at ambient temperature", ASTM International, West Conshohocken, PA, 2018, DOI:10.1520/C1358-13.

[38] ASTM Standard C1424, 2015 (1999), "Standard test method for monotonic compressive strength of advanced ceramics at ambient temperature", ASTM International, West Conshohocken, PA, 2018, DOI:10.1520/C1424-15.

[39] P. N. B. Anongba, J. Bonneville, and A. Joulain, "Brittle cracks under compression: Introducing Poisson effect", *Revue Internationale des Sciences et Technologie*, vol. 17, pp. 37-53, 2011.

[40] V. Tomar, and M. Zhou, "Tension-compression strength asymmetry of nanocrystalline α-Fe_2O_3+fcc-Al ceramic-metal composites", *Applied Physics Letters*, vol. 88, pp. 233107-1-4, 2006.

[41] R. Morrell, N. J. McCormick, J. Bevan, M. Lodeiro, and J. Margetson, "Biaxial disc flexure – modulus and strength testing", *British Ceramic Transactions*, vol. 98, pp. 234-240, 1999.

[42] D. K. Shetty, "Biaxial flexure test for ceramics", *American Ceramic Society Bulletin*, vol. 59, pp. 1193-1197, 1980.

[43] R. Thiruvengadaswamy, and R. O. Scattergood, "Biaxial flexure testing of brittle materials", *Scripta Metallurgica*, vol. 25, pp. 2529-2532, 1991.

[44] R. Stadelmann, M. Lugovy, N. Orlovskaya, P. Mchaffey, M. Radovic, V. M. Sglavo, S. Grasso, and M. J. Reece, "Mechanical properties and residual stresses in ZrB_2-SiC spark plasma sintered ceramic composites", *Journal of the European Ceramic Society*, vol. 36, pp. 1527-1537, 2016.

[45] K. H. Vepakomma, J. Westbrook, S. Carley, and J. Kim, "Finite element analysis of ring-on-ring test on LCD panels", *Journal of Display Technology*, vol. 9, pp. 673-677, 2013.

[46] J. E. Ritter, Jr., K. Jakus, A. Batakis, and N. Bandyopadhyay, "Appraisal of biaxial strength testing", *Journal of Non-Crystalline Solids*, vol. 38 & 39, pp. 419-424, 1980.

[47] A. Börger, P. Supancic, and R. Danzer, "The ball on three ball test for strength testing of brittle discs: stress distribution in the disc", *Journal of the European Ceramic Society*, vol. 22, pp. 1425-1436, 2002.

[48] A. A. Porporati, T. Miyatake, K. Schilcher, W. Zhu, and G. Pezzotti, "Ball-on-ring test in ceramic material revisited by means of fluorescence piezospectroscopy", *Journal of the European Ceramic Society*, vol. 31, pp. 2031-2036, 2011.

[49] ASTM Standard C1499, 2015 (2013), "Standard test method for monotonic equibiaxial flexural strength of advanced ceramics at ambient temperature", ASTM International, West Conshohocken, PA, 2015, DOI:10.1520/C1499-15.

[50] T. Fett, G. Rizzi, E. Ernst, R. Müller, and R. Oberacker, "A 3-balls-on-3-balls strength test for ceramic disks", *Journal of the European Ceramic Society*, vol. 27, pp. 1-12, 2007.

[51] R. Danzer, W. Harrer, P. Supancic, T. Lube, Z. Wang, and A. Börger, "The ball on three balls test – Strength and failure analysis of different materials", *Journal of the European Ceramic Society*, vol. 27, pp. 1481-1485, 2007.

[52] R. Danzer, P. Supancic, and W. Harrer, "Biaxial tensile strength for brittle rectangular plates", *Journal of the ceramic society of Japan*, vol. 114, pp. 1054-1060, 2006.

[53] A. Börger, P. Supancic, and R. Danzer, "The ball on three ball test for strength testing of brittle discs: Part II: analysis of possible errors in the strength determination", *Journal of the European Ceramic Society*, vol. 24, pp. 2917-2928, 2004.

[54] J. E. O. Ovri, "A parametric study of the biaxial strength test for brittle materials", *Materials Chemistry and Physics*, vol. 66, pp. 1-5, 2000.

[55] Y. Chen, A. Aman, M. Lugovy, N. Orlovskaya, S. Wang, X. Huang, T. Graule, and J. Kuebler, "Residual stress and biaxial strength in Sc_2O_3-CeO_2-ZrO_2/Y_2O_3-ZrO_2 layered electrolytes", *Fuel Cells*, vol. 13, pp. 1068-1075, 2013.

[56] K. H. Verpakomma, J. Westbrook, S. Carley, and J. Kim, "Finite element analysis of ring-on-ring test on LCD panels", *Journal of Display Technology*, vol. 9, pp. 673-677, 2013.

[57] R. Kao, N. Perrone, and W. Capps, "Large-deflection solution of the coaxial-ring-circular-glass-plate flexure problem", *Journal of the American Ceramic Society*, vol. 54, pp. 566-671, 1971.

[58] M. Wendler, R. Belli, A. Petschelt, D. Mevec, W. Harrer, R. Danzer, and U. Lohbauer, "Chairside CAD/CAM materials. Part 2: Flexural strength testing", *Dental Materials,* vol. 33, pp. 99-109, 2017.

[59] R. D. Kelly, G. J. P. Fleming, P. Hooi, W. M. Palin, and O. Addison, "Biaxial flexure strength determination of endodontically accessed ceramic restorations". *Dental Materials*, vol. 30, pp. 902-909, 2014.

[60] S. Timoshenko, and S. Woinowsky-Krieger, *Theory of plates and shells*, 2nd ed.: McGraw-Hill, New York, 1959.

[61] W. F. Adler, and D. J. Mihora, "Biaxial flexure testing: Analysis and experimental results", *Fracture Mechanics of Ceramics*, vol. 10, pp. 227-245, 1992.

[62] H. Fessler, and D. C. Fricker, "A theoretical analysis of the ring-on-ring loading disk test", *Journal of the American Ceramic Society*, vol. 67, pp. 582-588.

[63] J. A. Salem, and L. M. Powers, "Guidelines for the testing of plates" in Proceedings of the 27th International Cocoa Beach Conference on Advanced Ceramics and Composites: B, *Ceramic Engineering and Science Proceedings*, vol. 24, pp. 357-364, 2003.

[64] C. H. Hsueh, C. R. Luttrell, and P. F. Becher, "Modelling of bonded multilayered disks subjected to biaxial flexure tests", *International Journal of Solids and Structures*, vol. 43, pp. 6014-6025, 2006.

[65] Y. Xu, J. Han, H. Lin, and L. An, "Comparative study of flexural strength test methods on CAD/CAM Y-TZP dental ceramics", *Regenerative Biomaterials*, vol. 2, pp. 239-244, 2015.

[66] J. B. Wachtman, Jr., W. Capps, and J. Mandel, "Biaxial flexure testing of ceramic substrates", *Journal of Materials*, vol. 7, pp. 863-867, 1972.

[67] ASTM Standard F394, 1978 (1996), "Standard test method for biaxial flexure strength (modulus of rupture) of ceramic substrates", ASTM International, West Conshohocken, PA, 1978.

[68] A. A. Porporati, T. Miyatake, K. Schilcher, W. Zhu, and G. Pezzotti, "Ball-on-ring test in ceramic materials revisited by means of fluorescence piezospectroscopy", *Journal of the European Ceramic Society*, vol. 31, pp. 2031-2036, 2011.

[69] J. H. Zhao, J. Tellkamp, V. Gupta, and D. R. Edwards, "Experimental evaluations of the strength of silicon die by 3-point-bend versus ball-on-ring tests", *IEEE Transactions on electronics packaging manufacturing*, vol. 32, pp. 248-255, 2009.

[70] A. Simpatico, W. R. Cannon, and M. J. Matthewson, "Comparison of hydraulic-burst and ball-on-ring tests for measuring biaxial strength", *Journal of the American Ceramic Society*, vol. 82, 1999.

[71] G. D. Quinn, B. T. Sparenberg, P. Koshy, L. K. Ives, S. Jahanmir, and D. D. Arola, "Flexural strength of ceramic and glass rods", *Journal of Testing and Evaluation*, vol. 37, pp. 1-23, 2009.

[72] C. A. Tracy, "A compression test for high strength ceramics", *Journal of Testing and Evaluation*, vol. 15, pp. 14-19, 1987.

[73] M. J. Kerper, L. E. Mong, M. B. Stiefel, and S. F. Holley, "Evaluation of tensile, compressive, torsional, transverse, and impact tests and correlation of results for brittle cermets", *Journal of Research of the National Bureau of Standards*, vol. 61, pp. 149-169, 1958.

[74] F. L. Riley, "Silicon nitride and related materials", *Journal of the American Ceramic Society*, vol. 83, pp. 245-265, 2000.

[75] L. Toth, *Transition metal carbides and nitrides*: Elsevier, 2014.

[76] C. Piconi, and G. Maccauro, "Zirconia as a ceramic biomaterial", *Biomaterials*, vol. 20, pp. 1-25, 1999.

[77] H. W. Nasution, E. Purnama, S. Kosela, and J. Gunlazuardi, "Photocatalytic reduction of CO_2 on copper-doped titania catalysts prepared by improved-impregnation method", *Catalyst Communication*, vol. 6, pp. 313-319, 2005.

[78] E. Rosenberg, O. Koren, L. Reshef, R. Efrony, and I. Zilber-Rosenberg, "The role of microorganisms in coral health, disease and evolution", *Nature Reviews*, vol. 5, pp. 355-362, 2007.

[79] E. H. Gladfelter, "Skeletal development in *Acropora cervicornis*", *Coral Reefs*, vol. 3, pp. 51-57, 1984.

[80] D. E. Williams, and M. W. Miller, "Coral disease outbreak: pattern, prevalence and transmission in *Acropora cervicornis*", *Marine Ecology Progress Series*, vol. 301, pp. 119-128, 2005.

[81] R. W. Buddemeier, S. V. Smith, "Coral reef growth in an era of rapidly rising sea level: predictions and suggestions for long-term research", *Coral Reefs*, vol. 7, pp. 51-56, 1988.

[82] S. R. Massel, T. J. Done, "Effects of cyclone waves on massive coral assemblages on the Great Barrier Reef: meteorology, hydrodynamics and demography", *Coral Reefs*, vol. 12, pp. 153-166, 1993.

[83] O. Hoegh-Guldberg, P.J. Mumby, A. J. Hooten, R.S. Steneck, P. Greenfield, E. Gomez, C.D. Harvell, P. F. Sale, A. J. Edwards, K. Caldeira, N. Knowlton, C. M. Eakin, R. Iglesias-Prieto, N. Muthiga, R. H. Bradbury, A. Dubi, M. E. Hatziolos, "Coral reefs under rapid climate change and ocean acidification", *Science*, vol. 318, pp. 1737–1742, 2007.

[84] G. De'ath, J. M. Lough, K. E. Fabricius, "Declining coral calcification on the Great Barrier Reef", *Science*, vol. 323, pp. 116–119, 2009.

[85] J. S. Madin, M. J. O'Donnell, S. R. Connolly, "Climate-mediated mechanical changes to post-disturbance coral assemblages", *Biology Letters*, vol. 4, pp. 490–493, 2008.

[86] V. Tunnicliffe, "Breakage and propagation of the stony coral *Acropora cervicornis*", *Proceedings of the National Academy of Sciences of USA*, vol. 78, pp. 2427–2431, 1981.

[87] H. R. Laskar, "Asexual reproduction, fragmentation, and skeletal morphology of a plexaurial gorgonian", *Marine Ecology Progress Series*, vol. 5, pp. 61–67.

[88] M. L. Boller, T. D. Swain, H. R. Lasker, "Skeletal morphology and material properties of a fragmenting gorgonian coral", Marine Ecology Progress Series, vol. 228, pp. 131–141, 2002.

[89] E. H. Gladfelter, "Skeletal development in *Acropora cervocornis*: I. Patterns of calcium carbonate accretion in the axial corallite", *Coral Reefs*, vol. 1, pp. 45-51, 1982.

[90] T. E. Baldock, H. Karampour, R. Sleep, A. Vyltla, F. Albermani, A. Golshani, D. P. Callaghan, G. Roff, P. J. Mumby, "Resilience of branching and massive corals to wave loading under sea level rise − A coupled computational fluid dynamics-structural analysis", *Marine Pollution Bulletin*, vol. 86, pp. 91-101, 2014.

[91] P. Colomban, "Raman spectrometry, a unique tool to analyze and classify ancient ceramics and glasses", *Applied Physics A*, vol. 79, pp. 167-170, 2004.

[92] M. J. Baker, C. S. Hughes, K. A. Hollywood, "Raman spectroscopy" in *Biophotonics: Vibrational Spectroscopic Diagnostics*: Morgan & Claypool Publishers, 2016.

[93] G. Gouadec, L. Bellot-Gurlet, D. Baron, P. Colomban, "Raman mapping for the investigation of nanophased materials", Zoubir A. Raman imaging (ed.), *Techniques and Applications*, vol. 168, Springer, pp.85-118, 2012.

[94] V. Domnich, Y. Aratyn, W.M. Kriven, and Y. Gogotsi, "Temperature dependence of silicon hardness: experimental evidence of phase transformations", *Reviews on Advanced Materials Science*, vol. 17, pp. 33–41, 2008.

[95] C.R. Das, H.C. Hsu, S. Dhara, A. K. Bhaduri, B. Raj, L. C. Chen, K. H. Chen, S. K. Albert, A. Ray, and Y. Tzeng, "A complete Raman mapping of phase transitions in Si under indentation", *Journal of Raman Spectroscopy*, vol. 41, pp. 334–339, 2010.

[96] C. Carteret, M. De La Pierre, M. Dossot, F. Pascale, A. Erba, and R. Dovesi, "The vibrational spectrum of $CaCO_3$ aragonite: A combined experimental and quantum-mechanical investigation", *The Journal of Chemical Phyics*, vol. 138, pp. 014201-1-014201-12, 2013

[97] W. A. Deer, R. A. Howie, and J. Zussman, *An introduction to the rock-forming minerals*: Longman Group, 1992.

[98] F, C. Meldrum, "Calcium carbonate in biomineralisation and biomimetic chemistry", *International Materials Reviews*, vol. 48, pp. 187-224, 2003.

[99] R. Frech, E. C. Wang, and J. B. Bates, "The i. r. and Raman spectra of $CaCO_3$ (aragonite)", *Spectrochimica Acta*, vol. 36A, pp. 915-919, 1980.

[100] R. Adamsky, PDF card SiB_6, *Acta Crystallographica*, vol. 11, 744, 1958.

[101] C. Li, Y. Lin, and M. Wang, "Preparation and mechanical properties of ZrB_2-based ceramics using $MoSi_2$ as sintering aids", *Frontiers of Materials Science China*, vol. 4, pp. 271-275, 2010.

[102] S. C. Doney, V. J. Fabry, R. A. Feely, and J. A. Kleypas, "Ocean acidification: the other CO^2 problem", *Annual Review of Marine Science*, vol. 1, pp. 169-192, 2009.

[103] D. T. Barnes, "Coral skeletons: An explanation of their growth and structure", *Science*, vol. 170, pp. 1305-1308, 1970.

[104] E. H. Gladfelter, "Skeletal development in *Acropora palmate* (Lamarck 1816): a scanning electron microscope (SEM) comparison demonstrating similar mechanisms of skeletal extension in axial versus encrusting growth", *Coral Reefs*, vol. 26, pp. 883-892, 2007.

[105] N. J. Silbiger, M. J. Donahue, and R. E. Brainard, "Environmental drivers of coral reef carbonate production and bioerosion: a multi-scale analysis", *Ecology*, vol. 98, pp. 2457-2560, 2017.

[106] N. N. Marfenin, "Non-radial symmetry of the transport system of *Acropora* corals", *Invertebrate Zoology*, vol. 12, pp. 53-59, 2015.

[107] G. Subhash, and G. Ravichandran, "Split Hopkinson pressure bar testing of ceramics ASM handbook", *Mechanical Testing and Evaluation*, vol. 81, pp. 1933-1939, 1998.

[108] G. Subhash, and G. Ravichandran, "Mechanical behaviour of hot pressed aluminum nitride under uniaxial compression", *Journal of Material Science*, vol. 33, pp. 1933-1939, 1998.

[109] J. Dusza, "Fractographic failure analysis of brittle materials", *International Journal of Materials and Technology*, vol. 15, pp. 292-355, 2003.

[110] K. Alvarez, S.Camero, M. E. Alacrón, A. Rivas,and G. González, "Physical and mechanical properties evaluation of *Acropora palmate* coralline species for bone substitution applications", *Journal of Materials Science: Materials in Medicine*, vol. 13, pp. 509-515, 2002.

[111] C. G. Kontoyannis, and N. V. Vagenas, "Calcium carbonate phase analysis using XRD and FT-Raman spectroscopy", *Analyst*, vol. 125, pp. 251-255, 2000.

[112] S. Weiner, Y. Levi-Kalisman, S. Raz, and L. Addadi, "Biologically formed amorphous calcium carbonate", *Connective Tissue Research*, vol. 44, pp. 214-218, 2003.

[113] C. H. K. Williamson, "Vortex dynamics in the cylinder wake", *Annual Review of Fluid Mechanics*, vol. 28, pp. 477-539, 1996

[114] Y. B. P. Kwan, J. R. Alcock, "The impact of water impregnation method on the accuracy of open porosity measurements", *Journal of Materials Science*, vol. 37, pp. 2557-2561, 2002.

[115] J. F. Despois, R. Mueller, A. Mortensen, "Uniaxial deformation of microcellular metals", *Acta Materiala*, vol. 54, pp. 4129-4142.

[116] H. Schumacher, "Reef-building properties of Tubastraea micranthus (Scleractinia, Dendrophylliidae), a coral without zooxanthellae", *Marine Ecology Progress Series*, vol. 20, pp. 93-99.

[117] E. P. Butler, "Transformation-toughened zirconia ceramics", *Materials Science and Technology*, vol. 1, pp. 417-432, DOI: 10.1179/mst.1985.1.6.417, 1985.

[118] I. Birkby, H. Hodgson, Progress with Zirconia Ceramics. In: Riley F.L. (eds) *3rd European Symposium on Engineering Ceramics*. Springer, Dordrecht, 1991.

[119] M. I. Petrescu, "Boron nitride theoretical hardness compared to carbon polymorphs", *Diamond and Related Materials*, vol. 13, pp. 1848-1853, 2004.

[120] J. Eichler, "Boron nitride (BN) and BN composites for high-temperature applications", *Journal of the European Ceramic Society*, vol. 28, pp. 1105-1109, 2008.

[121] H. W. Kim, Y. H. Koh, H. W. Kim, "Densification and mechanical properties of B_4C with Al_2O_3 as a sintering aid", *Journal of the American Ceramic Society*, vol. 83, pp. 2863-2865, 2000.

[122] J. C. LaSalvia, R. B. Leavy, J. R. Houskamp, H. T. Miller, D. E. MacKenzie, J. Campbell, "Ballistic impact damage observations in a hot-pressed boron carbide", *Ceramic Engineering and Science Proceedings*, vol. 30, pp. 45-55, 2009.

[123] G. Sines, M. Adams, "Compression Testing of Ceramics". In: R. C. Bradt, D. P. H. Hasselman, F. F. Lange (eds), *Flaws and Testing. Fracture Mechanics of Ceramics,* vol. 3, pp. 403-449, Springer, Boston, MA, 1978.

[124] S. G. Seshadri, K. Chila, "Tensile Testing of Ceramics", *Journal of the American Ceramic Society*, vol. 70, pp. 242-244, C-242-C-244. doi:10.1111/j.1151-2916.1987.tb04887.x, 1987.

[125] A. L. Chamberlain, W. G. Fahrenholtz, G. E. Hilmas, "High-strength zirconium diboride-based ceramics", *Journal of the American Ceramic Society*, vol. 87, pp. 1170-1172, 2004.

[126] W. D. Callister, *Materials Science and Engineering: an Introduction*, New York, NY: John Wiley and Sons, 2007.

[127] T. K. Gupta, F. F. Lange, J. H. Bechtold, "Effect of stress-induced phase transformation on the properties of polycrystalline zirconia containing metastable tetragonal phase", *Journal of Material Science*, vol. 13, pp. 1464-1470, 1978.

[128] A. Aman, R. Jordan, Y. Chen, R. Stadelmann, M. Lugovy, N. Orlovskaya, E. A. Payzant, C. delaCruz, M. J. Reece, T. Graule, J. Kuebler, J, "Non-congruence of high-temperature mechanical and structural behaviors of $LaCoO_3$ based perovskites", *Journal of the European Ceramic Society*, vol. 37, pp. 1563-1576, 2017.

[129] A. G. Lanin, "Effect of residual stress on the strength of ceramic materials (review)", *Russian Metallurgy*, vol. 4, pp. 307-322, 2012.

[130] W. Liu, X. Ren, "Large piezoelectric effect in Pb-free ceramics", *Physical Review Letters*, vol. 103, pp. 257602-1- 257602-4, 2009.

[131] A. Aman, Y. Chen, M. Lugovy, N. Orlovskaya, M. J. Reece, D. Ma, A. D. Stoica, K. An, "*In-situ* neutron diffraction of $LaCoO_3$ perovskite under uniaxial compression. I. Crystal structure analysis and texture development", *Journal of Applied Physics*, vol. 116, pp. 013503-1 – 013503-10, 2014.

[132] J. Rödel, J. F. Kelly, B. R. Lawn, "In situ measurements of bridged crack interfaces in the scanning electron microscope", *Journal of the American Ceramic Society*, vol. 73, pp. 3313-3318, 1990.

[133] N. Orlovskaya, N. Browning, A. Nicholls, "Ferroelasticity in mixed conducting LaCoO$_3$ based perovskites: a ferroelastic phase transition", *Acta Materiala*, vol. 51, pp. 5063-5071, 2003.

[134] N. Fist, J. Dinan, R. Stadelmann, N. Orlovskaya, "*In*-situ three point bending device for measurements of vibrational response of ceramics under stress by microRaman spectroscopy", *Advances in Applied Ceramics*, vol. 111, pp. 433-439, 2012.

[135] K. Tomeoka, P. R. Buseck, "Matrix mineralogy of the Orgueil CI carbonaceous chondrite", *Geochimica et Cosmochimica Acta*, vol. 52, pp. 1627-1640, 1988.

[136] P. Beck, E. Quirico, G. Montes-Hernandez, L. Bonal, J. Bollard, F. R. Orthous-Daunay, K. T. Howard, B. Schmitt, O. Brissaud, F. Deschamps, B. Wunder, S. Guillot, "Hydrous mineralogy of CM and CI chondrites from infrared spectroscopy and their relationship with low albedo asteroids", *Geochimica et Cosmochimica Acta*, vol. 74, pp. 4881-4892,2010.

[137] P. A. Bland, G. Cressey, O. N. Menzies, "Modal mineralogy of carbonaceous chondrites by X-ray diffraction and Mössbauer spectroscopy", *Meteoritics & Planetary Science*, vol. 39, pp. 3-16, 2010.

[138] R. J. Macke, G. J. Consolmagno, D. T. Britt, "Density, porosity, and magnetic susceptibility of carbonaceous chondrites", *Meteoritics & Planetary Science*, vol. 46, pp. 1842-1862, 2011.

[139] G. J. Flynn, G. J. Consolmagno, P. Brown, R. J. Macke, "Physical properties of the stone meteorites: Implications for the properties of their parent bodies", *Chemie der Erde*, vol. 78, pp. 269-298, 2018.